Test of the Standard Model of Electroweak Interactions by Measuring the Anomalous $WW\gamma$ couplings at $\sqrt{s} = 1.8$ TeV

A Dissertation

Submitted to the Graduate School
of the University of Notre Dame
in Partial Fulfillment of the Requirements
for the Degree of

Doctor of Philosophy

by

Michael Lawrence Kelly

Nripendra N. Biswas, Director

Department of Physics
Notre Dame, Indiana

April 1996

Test of the Standard Model of Electroweak Interactions by Measuring the Anomalous $WW\gamma$ Couplings at $\sqrt{s} = 1.8$ TeV

Abstract

by

Michael Lawrence Kelly

An analysis of $W\gamma$ events found in 73.0 pb^{-1} collected with the DØ detector during Tevatron Run 1b is presented. Forty-six candidate events are observed with a predicted background of 13.2 events. The total cross section for $p\overline{p} \rightarrow W\gamma + X$ (for $p_T^{\gamma} >$ 10 GeV/c and $\Delta R_{e\gamma} > 0.7$) times the branching ratio of W bosons to electrons is measured to be:

$$\sigma(p\overline{p} \rightarrow W\gamma + X) \times \mathrm{BR}(W \rightarrow e\nu) = 11.19^{+2.66}_{-2.32} \pm 0.61\ (syst)\ \pm 0.56\ (lum)\ \mathrm{pb}$$

95% confidence level limits on the CP–conserving anomalous coupling parameters are set using a fit to the photon transverse energy spectrum of the events with a three-body transverse cluster mass greater than 90 GeV/c^2. The results are:

$$-1.4 < \Delta\kappa < 1.4\ (\lambda = 0) \ \text{ and } \ -0.5 < \lambda < 0.5\ (\Delta\kappa = 0)$$

with similar limits are set on the CP–violating coupling parameters $\tilde{\kappa}$ and $\tilde{\lambda}$. These limits were set by assuming a dipole form factor with a scale factor of $\Lambda = 1.5$ TeV.

These results are combined with the previous DØ $W\gamma$ results to set limits on the coupling parameters of

$$-1.2 < (\Delta\kappa, \tilde{\kappa}) < 1.2 \text{ and } -0.4 < (\lambda, \tilde{\lambda}) < 0.4$$

when all other couplings are restricted to their Standard Model values.

No deviation from the predicted Standard Model $WW\gamma$ interaction is observed.

This thesis is dedicated to everyone who has ever held a child's hand while pointing up into a star–filled sky.

TABLE OF CONTENTS

LIST OF FIGURES vi

LIST OF TABLES viii

ACKNOWLEDGEMENTS x

1 INTRODUCTION 1

2 THE STANDARD MODEL AND THE $WW\gamma$ INTERACTION . . 3

2.1 Introduction to the Standard Model 3

2.2 The Basic Electroweak Interaction 7

2.3 Gauge Boson Self-Interactions 10

2.3.1 Signatures of W bosons and $W\gamma$ events 14

2.3.2 Characteristics of $W\gamma$ Events 16

2.4 Previous Studies of the $WW\gamma$ Interaction 20

2.4.1 Low-Energy, Indirect Tests 20

2.4.2 $q\overline{q} \rightarrow W\gamma$ at UA2 21

2.4.3 $q\overline{q} \rightarrow W\gamma$ at the Tevatron 21

3 EXPERIMENTAL APPARATUS 24

3.1 The Tevatron 24

3.1.1 Tevatron Operation in Collider Mode 25

3.2 The DØ Detector 28

3.3 Calorimetry 31

3.3.1 Central Calorimeter 34

3.3.2 Endcap Calorimeters 36

3.3.3 Intercryostat Detector and Massless Gap Detector . . . 37

3.4 Central Tracking 38

3.4.1 Vertex Drift Chambers 39

3.4.2 Transition Radiation Detector 40

3.4.3 Central Drift Chamber 41
3.4.4 Forward Drift Chambers 42
3.5 Outer (Muon) Tracking 43
3.6 Trigger and Data Acquisition 45
3.6.1 Level 0 Trigger and Luminosity Monitor 46
3.6.2 Level 1 and Level 1.5 Triggers 48
3.6.3 Level 2 Filter and Data Acquisition System 49
3.7 Offline Reconstruction 49
3.7.1 Vertex Reconstruction 50
3.7.2 Electron/Photon Reconstruction 50
3.7.3 Muon Reconstruction 51
3.7.4 Jet Reconstruction 52
3.7.5 Reconstruction of Missing Transverse Energy ($\not\!\!E_T$) . . . 52
3.8 Monte Carlo 53

4 EVENT SELECTION 58
4.1 Trigger Efficiencies 58
4.2 Particle Identification 61
4.2.1 Electron Identification 63
4.2.2 Photon Identification 66
4.3 $W \to e\nu$ Sample 71
4.4 $W(e\nu)\gamma$ candidates 72
4.5 Backgrounds to $W(e\nu)\gamma$ 73
4.5.1 QCD Background 73
4.5.2 eeX Background 76
4.5.3 $Z\gamma$ Background 78
4.5.4 $W(\tau\nu)\gamma$ Background 78
4.5.5 Summary of Backgrounds 79
4.6 $\sigma(p\overline{p} \to W\gamma + X) \times \mathrm{BR}(W \to e\nu)$ Measurement 79

5 LIMITS ON THE ANOMALOUS COUPLINGS 81
5.1 Limits from the Total Cross Section Measurement 81
5.2 Limits from Fitting the p_T^γ Spectrum 85
5.3 Limits from the Production Events 90
5.4 Combination of this Work with Previous Results 92

6 CONCLUSIONS 95

A RUN 1A $W\gamma$ RESULTS 98

B RUN 1B $W\gamma$ ANALYSIS USING BOTH "DIRTY" AND "CLEAN" PHOTONS 101

BIBLIOGRAPHY 105

LIST OF FIGURES

2.1 Leading order Feynman diagrams 12

2.2 The cross section for $p\overline{p} \rightarrow W(e\nu)\gamma$ as a function of two coupling parameters 17

2.3 Typical $d\sigma/dp_T^\gamma$ spectrum for different anomalous coupling constants in $p\overline{p} \rightarrow W(e\nu)\gamma$ 18

3.1 The Tevatron accelerator schematic layout. 26

3.2 Overview of the DØ detector 29

3.3 Longitudinal arrangement of the calorimeter 34

3.4 Side view of one-fourth of the calorimeter, showing the projective cell structure for successive layers 35

3.5 Side view of the the DØ central tracking system. 39

3.6 Side view of the DØ muon system 45

3.7 SM $W\gamma$ cross sections for different structure functions 57

4.1 The turn-on curve for the $\not\!\!E_T$ part of EM1_EISTRKCC_MS 60

4.2 The turn-on curves for the electromagnetic E_T part of EM1_EISTRKCC_MS, for EM objects in each calorimeter 61

4.3 The efficiency of the photon ID cuts for photons with E_T below 23.0 GeV 68

4.4 Characteristic spectra for the Run 1b $W \rightarrow e\nu$ events 71

4.5 Characteristic spectra for the Run 1b $W(e\nu)\gamma$ candidates . . . 73

4.6 Event displays for a $W(e\nu)\gamma$ candidate 74

4.7 The probability for a jet to fake a photon in each calorimeter . 76

5.1 The predicted cross section and efficiency for $p\overline{p} \rightarrow W(e\nu)\gamma$ as a function of λ 82

5.2 Run 1b limits on the anomalous couplings from the $p\overline{p} \rightarrow W(e\nu)\gamma$ cross section measurement 86

5.3 Run 1b limits on the anomalous couplings from the fit to the p_T^γ spectrum 89

5.4 Run 1b limits on the anomalous couplings from the fit to the p_T^γ spectrum of the production events 91

5.5 Limits on the anomalous couplings $W\gamma$ from the fit to the p_T^γ spectrum of the Run 1a events and the Run 1b production events 94

6.1 Comparison of the 95% CL limits on $\Delta\kappa$ and λ from this experiment with previously published results 97

A.1 Characteristic spectra for the Run 1a $W\gamma$ candidates 100

B.1 Characteristic spectra for the Run 1b $W(e\nu)\gamma$ candidates before the hits–in–road cut is applied 103

B.2 Run 1b limits on the anomalous couplings from the fit to the total cross section, using both "dirty" and "clean" events . . . 104

LIST OF TABLES

2.1 The three generations of leptons 4

2.2 The three generations of quarks 5

2.3 The mediators of the electroweak force 7

2.4 Quantum numbers for first generation leptons in standard electroweak model 8

2.5 Comparison of early Standard Model predictions with first measurements of the IVB masses 9

3.1 Parameters of the DØ Central Calorimeter 36

3.2 Parameters of the DØ Endcap Calorimeters 37

3.3 Parameters of the DØ Vertex Drift Chamber 40

3.4 Parameters of the DØ Transition Radiation Detector 41

3.5 Parameters of the DØ Central Drift Chamber 42

3.6 Parameters of the DØ Forward Drift Chambers 43

3.7 Resolution parameters of the EM calorimeter 51

3.8 Resolution parameters of the hadronic calorimeter 52

3.9 Comparison of the different resolutions of electromagnetic and hadronic objects at different energies 52

3.10 Missing E_T resolution parameters 53

4.1 Definitions and efficiencies (ε) for the electron identification cuts in the central and endcap calorimeters 66

4.2 Definitions and efficiencies (ε) for the photon identification cuts in the central and endcap calorimeters 67

4.3 Parameters for low E_T photon efficiencies 69

4.4 E_T-independent values of Prob(jet $\rightarrow \gamma$), by calorimeter 75

4.5 Summary of $W(e\nu)\gamma$ backgrounds for Run 1b 79

5.1 Some confidence level (CL) intervals 85

5.2 Data used in the binned fit to p_T^γ 88

5.3 Data used in the binned fit to p_T^γ for the production events . . 90

5.4 Values of the nuisance parameters used in the limits setting procedure 93

A.1 Summary of Run 1a $W(e\nu)\gamma$ and $W(\mu\nu)\gamma$ data and backgrounds 99

B.1 Summary of backgrounds for the $W\gamma$ analysis both with and without the hits–in–road cuts 102

ACKNOWLEDGEMENTS

The acknowledgement of individuals who have made an impact on a student's doctoral dissertation is an honored tradition that will be continued here. There are many people who deserve a great deal of thanks, and in some cases no small share of the credit, for this work which bears my name. I am proud to have worked with many scientists during my tenure at the University of Notre Dame and DØ. It is *because* of these people, and not despite them, that I was able to spend many enjoyable years doing the work of Physics.

My colleagues in the diboson group deserve first recognition. We share a reputation for being an excitible and contentious bunch. These attributes have served us well; our group has consistently produced results which have kept us ahead of the orange team across the ring. Hiro Aihara, Tom Diehl, Tony Spadafora and Taka Yasuda deserve tremendous credit for bearing the mantle of leadership during these long years. The hard work and numerous cross-checks provided by Paul Bloom, Liang-Ping Chen, Brajesh Choudhary, Tom Fahland and Steve Glenn made this analysis bearable. I can never thank John Ellison enough for serving as chairman of my Editorial Board. It was his willingness to guide this work through the last six months which enabled me to finish on such a reasonable time scale. Not forgotten are the editorial efforts of Sue Blessing and Rajendran Raja.

I can go no further without recognizing the tremendous contribution of Greg Landsberg to this work. I owe the very topic of my dissertation to the fact that Greg decided to leave the realm of the charged IVB to study the interaction of the Z boson and the photon. From the day he agreed to let me have the $W\gamma$ topic, 21 July 1993, he has been a tremendous asset and a valued colleague. I am glad to have known him during my time at DØ.

Ulrich Baur deserves special mention for providing us with the Monte Carlo event generator, and his many talks at Fermilab which inspired this work. Alan Jonckheere, Paul Russo and Jim Bishop deserve my thanks for making it possible for me to run the Monte Carlo on their computer networks.

There are too many other people at DØ to thank individually. I've had the opportunity to work with more people than I can name; from the electron-ID group to the WZ group to all the many people I shared shifts with on Runs 1a, 1b and 1c. It has been a pleasure working in an environment with so many bright, dedicated and thoughtful people.

I owe all of this to the Arthur J. Schmitt foundation and Richard Becker. The Schmitt foundation made it possible for me to attend the University of Notre Dame and dedicate so much of my time to the field I love. Other sources of inspiration from my home institution are Physics Department chairman Jerry Jones and Vice-President for Graduate Studies Nathan Hatch. Each of these two men clearly demonstrated how an individual can calmly examine problems and establish a long–term plan for addressing them.

The many friends I've known from Notre Dame have given me greater insight and a deeper understanding of people than I would have thought possible. Those deserving individual mention are my former housemates Chris Kennedy and Doran Stienike. I am in the debt of Creighton University for producing

two such well-rounded individuals and sending them on to Notre Dame. A group acknowledgement goes to all those who worked with me during my time as president of the Graduate Student Union. We overcame terrible obstacles to accomplish great things that year; I am proud to have served with you.

Finally, I must thank all of my teachers, from those at Morgan elementary school and Nottingham High, through Drew University, to Notre Dame and DØ. After my parents, I can think of no one who has influenced my life so deeply. It is my hope that each of you can see a little of yourself in this work. Special thanks goes to my advisor, Nripen Biswas, who always made sure I had what I needed to survive. He provided me with inspiration, an office, computer equipment, travel opportunities, steady pay, and even a place to live while at Fermilab. I am proud to have been his final doctoral student.

CHAPTER 1

INTRODUCTION

The universe in which we live is a wonderful and exciting place. The human species can give no greater honor to that which created this marvelous playground than to spend its existence attempting to understand the nature of *being*. Elementary particle physics may be just one small aspect of this ancient endeavor, but it has been the sole focus of this student's work for many years. This thesis describes the details of the $WW\gamma$ analysis as it was performed at the DØ detector located at the Fermi National Accelerator Laboratory in Batavia, Illinois.

Chapter 2 (*The Standard Model and the $WW\gamma$ Interaction*) should serve as an introduction to the elements of nature upon which this work is based. Some of the mathematics relevent to this work will be provided, with enough references to supporting material to assist the dedicated reader. Chapter 3 (*Experimental Apparatus*) describes the tools used to approach this study, and Chapter 4 (*Event Selection*) presents the details of the analysis.

Chapter 5 (*Limits on the Anomalous Couplings*) contains the majority of the information of interest to the people who are concerned with vector boson self–interactions. It describes the procedure for setting limits on the anomalous $WW\gamma$ couplings and presents limits which are currently the tightest in the

world.

These results are summarized and compared with other recent, similar experiments in Chapter 6. Additionally, two appendices are included. The first summarizes the previous $WW\gamma$ study performed at the same experiment. The second provides slightly more details about the primary improvement in event selection between this study and the previous work.

CHAPTER 2

THE STANDARD MODEL AND THE $WW\gamma$ INTERACTION

This chapter provides a brief overview of the Standard Model of elementary particles, with the primary focus on the self-interaction of gauge bosons. Specifically, the $WW\gamma$ vertex is described, and some features of the interaction are discussed. Previous experimental results are presented.

2.1 Introduction to the Standard Model

The current view of the universe is that all matter is constructed from tiny, indivisible components. It would be an understatement of extraordinary magnitude to say that this "particular" model is not a new idea. Similarly, the idea of breaking things to see how they are built and to learn how they work, is a habit that has its roots in antiquity. Even today, at the end of the second millenium, it is these two ancient desires, to break things and then to categorize them, that has led to what we refer to as the Standard Model of elementary particles.

The Standard Model neatly incorporates the fundamental particles (from which all matter is made) into three separate categories: leptons, quarks, and mediators. There are six *leptons* divided into three familes, or generations[1].

[1]Each family (of both quarks and leptons) is considered to have a unique quantum number

Each family of leptons has two members, one that carries an electric charge and one that is electrically neutral. The "first family" of the leptons has as its members the ubiquitous *electron* (e) and its neutral partner the *neutrino* (ν_e). The electron is the carrier of (negative) unit charge which travels through the circuitry of our homes. The more massive relatives of the electron are the *muon* (μ) and the *tau* (τ); each has a neutral partner similar to the electron's neutrino (ν_μ,ν_τ)[2]. Some characteristics of the leptons are given in Table 2.1.

Table 2.1. The three generations of leptons

Lepton	**Charge**	**Mass (MeV)**	**Lifetime (s)**
e	-1	0.511	∞
ν_e	0	$< 5.1 \times 10^{-6}$	$> 300\ m_{\nu_e}\mathrm{eV}^{-1}$
μ	-1	105.7	2.19×10^{-6}
ν_μ	0	< 0.3	$> 15.4\ m_{\nu_\mu}\mathrm{eV}^{-1}$
τ	-1	1777	2.96×10^{-13}
ν_τ	0	< 31	N.A.

The next category of matter are the *quarks*. Like the leptons there are three generations of quarks; the most common family members are the lightweight *up* (u) and *down* (d) quarks. These two quarks are the primary constituents of all matter encountered in our daily experiences. The u and d quarks are bound in the more familiar protons and neutrons.

The quarks which make up everday matter also contains tiny fractions of the more massive quarks: *strange* (s), *charm* (c), *bottom* (b), and the most massive of all quarks, the *top* (t). Among the many extraordinary features of

that is always conserved. For example, the net number of first generation leptons in the universe cannot change, except by a corresponding change in the number of first generation antileptons. Later this quantity will be referred to as *weak isospin*.

[2]The tau neutrino (ν_τ) has not yet been experimentally observed.

Table 2.2. The three generations of quarks

Quark	Charge	Effective Mass (MeV)
down (d)	$-1/3$	5-15
up (u)	$+2/3$	2-8
strange (s)	$-1/3$	100-300
charm (c)	$+2/3$	1000-1600
bottom (b)	$-1/3$	$\sim 4.3 \times 10^3$
top (t)	$+2/3$	$\sim 180 \times 10^3$

quarks is that each quark has an electric charge, but unlike the charge of the electron, quarks have *fractional* charges. The quarks also carry single units of something similar to charge, called *color*. Each quark may be one of any *three* different colors, whereas the charged leptons have only *one* type of charge. Some properties of quarks are given in Table 2.2. It is important to note that each lepton and quark has an antiparticle, allowing for the possibilities of opposite charges and even anticolors[3]!

Finally, there are the mediators of the four fundamental forces. Two of the forces are beyond the scope of this work: *gravity*, presumably mediated by an undiscovered particle called the *graviton*, and the *strong* force, mediated by *gluons*. Gravity, the most obvious of all forces in everyday life, is too weak to play any significant role in the interaction of the fundamental particles. This is due to the tiny masses of the individual quarks and leptons. Because of this and other reasons, gravity is not even considered part of the Standard Model, although it is included in Grand Unified Theories which extend the Standard Model to unify all forces.

The strong force, which binds the quarks (q) into the protons (p) and

[3]Antiparticles have the opposite quantum numbers of their corresponding particle.

antiquarks ($\overline{q}$) into the antiprotons ($\overline{p}$) manifests itself best at the Tevatron in a variety of QCD (Quantum ChromoDynamics) experiments, e.g. [1] [2]. The topic of this work is not related to the strong interaction. Its effect on data collection cannot be completely ignored in this work; it manages to muscle its way into every measurement at DØ, usually by producing backgrounds to much rarer processes. Large QCD backgrounds are a feature of experiments at $p\overline{p}$ colliders; this is the price that must be paid for colliding bundles of quarks (inside protons) with bundles of antiquarks (inside antiprotons). Only objects with color/anticolor (or colored constituents) experience the strong force.

The last two forces are related. Of the two, *electromagnetism* is perhaps the more familiar. The electromagnetic force is experienced by all particles with an electric charge and is mediated by the massless photon (γ). It is much weaker than the strong force but, because of its nature, extends far enough for us to witness its effects directly. Indeed, the electromagnetic force extends as far as the eye can see!

The last force, the *weak* force, acts equally among all quarks and leptons, independent of electric charge, color or mass. The weak force allows quarks or leptons of the same generation to interact through one of two electrically charged mediators, the W^+ or W^- bosons. The weak force also allows for a neutral interaction via an uncharged mediator, the Z^0 boson. The electromagnetic and weak interactions can be considered as different manifestations of a single *electroweak* force. The theory that ties the two forces together is referred to as the Glashow-Weinberg-Salam (GWS) theory. Some properties of the mediators of the electroweak force are summarized in Table 2.3.

Table 2.3. The mediators of the electroweak force

Mediator	Force	Mass (GeV)	Lifetime (s)
photon (γ)	Electromagnetic	$< 3 \times 10^{-39}$	∞
$W^{\pm}$	Weak	80.2	3×10^{-28}
Z^0	Weak	91.1	3×10^{-28}

2.2 *The Basic Electroweak Interaction*

The standard model of electroweak interactions is the marriage of clever mathematics to a history of keen-eyed observation. Not unforgotten is the long lineage of physicists present during both the courtship and the wedding. This author's preference is to present the GWS theory in terms of experimental observations rather than provide a more rigorous, mathematical outline. Following the example of Quigg [3], the GWS model is examined here only in the leptonic sector, which can be extended to the three generations of quarks along similar lines.

The various leptons are formed into left–handed[4] *weak-isospin* doublets,

$$t = \frac{1}{2} \text{ doublets } \left\{ \begin{array}{l} t_3 = +1/2 \\ t_3 = -1/2 \end{array} \right. \begin{pmatrix} \nu_e \\ e^- \end{pmatrix}_{\mathrm{L}} \cdots$$

Here, t is used to denote the weak isospin and t_3 is the third component of t. The doublets for the μ and τ generations (or *families*) are similarly described.

Experimentally it was observed that the weak charged currents cause transitions within the doublets, e.g. $e \rightarrow \nu_e$, but not between familes, e.g. $\mu \rightarrow \nu_e$. There is also the existence of a weak neutral current. The charged weak currents suggested two charged mediators, or *Intermediate Vector Bosons* (IVBs),

[4]The *handedness* of a particle refers to its *helicity*. Neutrinos are massless; they cannot be right–handed. In this formalism, only the left–handed leptons are included. The right–handed electron is arranged to belong to the $t = 0$ group as a weak isospin singlet.

one positive and one negative. The neutral current required at least one neutral IVB. The short range of the weak interaction suggested that the weak field quanta are massive, and additional observations showed that the weak interaction had the same coupling to all fermions, a characteristic often referred to as *universality*.

The weak isospin doublets transform under $SU(2)$ symmetry[5]. The non-Abelian $SU(2)$ group has three generators, allowing for three IVBs. Glashow suggested enlarging the group to $SU(2)_W \otimes U(1)_Y$, where the Abelian $U(1)_Y$ group is associated with a new quantum number y called the *weak hypercharge* (see Table 2.4) . The weak hypercharge is related to the electric charge (Q) and weak isospin by the Gell-Man–Nishijima formula: $Q = t_3 + y/2$.

Table 2.4. Quantum numbers for first generation leptons in standard electroweak model

Particle	t	t_3	y	Q
ν_e	$1/2$	$+1/2$	-1	0
e_L	$1/2$	$-1/2$	-1	-1

The gauge group $SU(2)_W \otimes U(1)_Y$ then requires four gauge bosons. The recipe for constructing the theory of weak interactions proceeds from this choice of gauge group and the assigment of fermions (as shown here for electrons, but the full electroweak theory includes the quarks and other leptons as well) to the representations[6] of the group. A scalar field (the Higgs field) is introduced to give both the fermions and the IVBs masses, then parameters are

[5] A straightforward text in this matter is Guidry [4], §5 - §9. Guidry leads the reader in a detailed and patient manner through the material necessary for a full appreciation of other texts.

[6] The right-handed components of particles have different quantum numbers from their left-handed counterparts; they are said to belong to different representations of the same gauge group.

chosen to break the symmetry spontaneously, via the *Higgs mechanism*, in a manner consistent with low-energy phenomenology [4]. One such consistency is the fact that the photon is massless.

The Lagrangian density ($\mathcal{L}$, sometimes referred to as simply, the *Lagrangian*[7]) of the standard electroweak model can be considered the sum of four parts:

$$\mathcal{L} = \mathcal{L}_g + \mathcal{L}_f + \mathcal{L}_s + \mathcal{L}_{f-s}$$

Here $\mathcal{L}_g$ represents the Lagrangian for the gauge fields, $\mathcal{L}_f$ for the fermion fields and their coupling to the gauge fields, the third Lagrangian $\mathcal{L}_s$ involves the scalar fields, and finally $\mathcal{L}_{f-s}$ determines the coupling between the fermions and the scalar fields. In the gauge sector of the Standard Model there are three free parameters: the fine structure constant $\alpha = e^2/(4\pi) = 1/(137.0359895 \pm 0.0000061)$, the Fermi coupling constant $G_F = (1.16639 \pm 0.00002)\times 10^{-5}\,\mathrm{GeV}^{-2}$, and the Weinberg angle θ_W, $\sin^2\theta_W = 0.2319 \pm 0.0005$ [5]. The GSW theory has amazing predicitive power once these parameters are known. See Table 2.5 for some early measurements compared to the first theoretical predictions [6].

Table 2.5. Comparison of early Standard Model predictions with first measurements of the IVB masses

Quantity	UA1 Experiment	UA2 Experiment	SM Prediction
m_W (GeV/c^2)	$83.5^{+1.1}_{-1.0} \pm 2.8$	$81.2 \pm 1.1 \pm 1.3$	82.0 ± 1.3
m_Z (GeV/c^2)	$93.0 \pm 1.4 \pm 3.2$	$93.0 \pm 1.3 \pm 1.5$	91.1 ± 1.1

[7] The Lagrangian density is a function of fields and their space-time derivatives, just as the Lagrangian is a function of coordinates and their time-derivatives.

2.3 Gauge Boson Self-Interactions

The gauge boson portion of the electroweak Lagrangian density is

$$\mathcal{L}_g = -\frac{1}{4}F^j_{\mu\nu}F^{\mu\nu}_j - \frac{1}{4}f_{\mu\nu}f^{\mu\nu}. \tag{2.1}$$

The electromagnetic field strength tensor is that of the photon field $\mathbf{A}$:

$$f_{\mu\nu} = \partial_\mu A_\nu - \partial_\nu A_\mu,$$

and the weak field strength tensor (derived from the weak IVB field $\mathbf{W}$) is given by

$$F^j_{\mu\nu} = \partial_\mu W^j_\nu - \partial_\nu W^j_\mu - g\epsilon_{jkl}W^k_\mu W^l_\nu.$$

It is important to note that mass terms for the field W^j_μ are *not* permitted since they must be proportional to $\mathbf{A}_\mu \cdot \mathbf{A}^\mu$ which is not gauge invariant[8]. This is a well known consequence of the gauge symmetry being spontaneously broken: the Lagrangian is invariant under $SU(2)_W \otimes U(1)_Y$ gauge transformations even while the solution to the Lagrangian is not [7].

Equation 2.1 is the part of the full Lagrangian which is responsible for the self-interaction of the gauge bosons. In the Standard Model there are two allowed cubic couplings ($WW\gamma$, WWZ) and four allowed quartic couplings ($WW\gamma\gamma$, $WWZ\gamma$, $WWZZ$, $WWWW$). The scope of this work includes only the study of the cubic $WW\gamma$ coupling from the reaction $q\overline{q} \rightarrow W\gamma$ in $p\overline{p}$ interactions. Similar work at DØ [8] and CDF [9] involves the study of the $WW\gamma$ and WWZ vertices from the rarer process $q\overline{q} \rightarrow WW$. The non-allowed cubic couplings $ZZ\gamma$ and $Z\gamma\gamma$ have also been searched for at both DØ [10] and CDF [11]. In some sense the primary difference between study of the

[8] All masses must come from the *Higgs mechanism* [4].

cubic couplings and the quartic couplings is that the cubic couplings directly test the non-Abelian gauge structure of the electroweak model while the study of the much rarer quartic couplings will be used as a window on electroweak symmetry breaking. The possible future study of quartic gauge boson self-couplings has been explored, the curious reader is directed elsewhere [12].

One of the topics of this dissertation is to measure the cross section of associated vector boson production in $q\overline{q}$ interactions; $q\overline{q} \rightarrow W\gamma$ with subsequent $W \rightarrow e\nu$ decays, leading to a final state of $e\nu\gamma$. In the Standard Model the direct coupling of the W boson and the photon occurs in the s-channel W exchange, as shown in Figure 2.1 (c). At tree level, the $e\nu\gamma$ final state can also originate from the t- or u-channel quark exchange as shown in Figures 2.1 (a) and (b). The GWS theory of electroweak interactions can predict the total cross section of these *production* processes [13]. This study is aimed to confront the theoretical predicition with the the experimental data, as well as to look for deviations from the Standard Model. It is important to note that for leptonic decays of the W boson, there is one final avenue which arrives at a final state of $e\nu\gamma$. The *decay* $W\gamma$ diagram is due to photon radiation from the decay electron and is shown in Figure 2.1 (d).

Despite the successes of the GWS theory of electroweak interactions, the possibility of deviations from the Standard Model exists. Anomalous $WW\gamma$ couplings could be one such deviation. If such anomalies exist, they must be parametrized in such a way as to allow experimentalists to study them. The conventional modification made to the gauge boson portion of the Lagrangian involving the $WW\gamma$ vertex is to use an *effective*[9] Lagrangian [15],

[9]Many authors point out that the notion of an effective Lagrangian is a very useful one since it may be possible to severely constrain the form of a theory without knowing the full dynamics of the fundamental theory [14]. Here possible modifications of the gauge

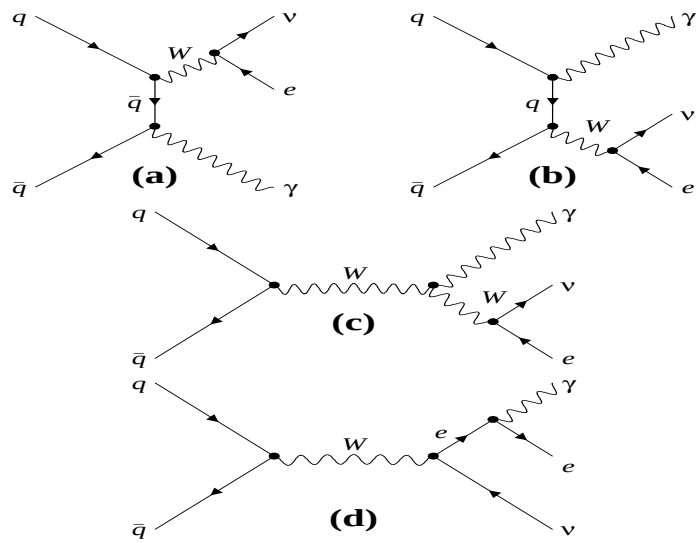

Figure 2.1. Leading order diagrams of $q\overline{q} \to W(e\nu)\gamma$ final states. Diagrams (a) and (b) are the *initial state radiation* (ISR) diagrams; diagram (d) is the *decay* diagram. Diagram (c) shows the trilinear $WW\gamma$ coupling. Together, diagrams (a), (b), and (c) are referred to as the *production* diagrams.

$$\begin{aligned}\mathcal{L}_{WW\gamma} &= -i\,\mathrm{e}[(W^\dagger_{\mu\nu}W^\mu A^\nu - W^\dagger_\mu A_\nu W^{\mu\nu}) \\ &\quad + \kappa\, W^\dagger_\mu W_\nu F^{\mu\nu} + \frac{\lambda}{m_W^2} W^\dagger_{\lambda\mu} W^\mu_\nu F^{\nu\lambda} \\ &\quad + \tilde{\kappa}\, W^\dagger_\mu W_\nu \tilde{F}^{\mu\nu} + \frac{\tilde{\lambda}}{m_W^2} W^\dagger_{\lambda\mu} W^\mu_\nu \tilde{F}^{\nu\lambda}\ ].\end{aligned}$$

Here A^μ and W^μ are the photon and W^- fields, $W_{\mu\nu} = \partial_\mu W_\nu - \partial_\nu W_\mu$, $F_{\mu\nu} = \partial_\mu A_\nu - \partial_\nu A_\mu$, and $\tilde{F}_{\mu\nu} = \frac{1}{2}\varepsilon_{\mu\nu\rho\sigma}F^{\rho\sigma}$. The constant e is the charge of the proton.

In the Standard Model, the *coupling parameters* $(\kappa, \lambda, \tilde{\kappa}, \tilde{\lambda})$ have the values $\kappa = 1$, $\lambda = \tilde{\lambda} = \tilde{\kappa} = 0$. The term of the effective Lagrangian with no coupling parameters is due to the minimal $U(1)_{EM}$ coupling of the photon to the electric charge of the W boson. It is important to recognize that the $SU(2)_W \otimes U(1)_Y$ symmetry manifests itself explicitly in the second (κ) term, a clear indication

boson interaction are not proposed, only that there may be some.

of the non-Abelian nature of the Standard Model. The quantities κ, etc. are related to physical properties of the W boson; κ and λ are CP–conserving couplings and are related to the electric quadrupole moment of the W boson (Q_W) and its magnetic dipole moment (μ_W):

$$Q_W = -\frac{e}{m_W^2}\,(\kappa - \lambda)$$

and

$$\mu_W = \frac{e}{2\,m_W}\,(1 + \kappa + \lambda).$$

The $\tilde{\kappa}$ and $\tilde{\lambda}$ terms are CP–violating; they are related to the electric dipole moment (d_W) and magnetic quadrupole moment (Q_W^m):

$$d_W = \frac{e}{2\,m_W}\,(\tilde{\kappa} + \tilde{\lambda})$$

and

$$Q_W^m = -\frac{e}{m_W^2}\,(\tilde{\kappa} - \tilde{\lambda}).$$

If all the parameters in the $WW\gamma$ coupling have the standard form for $q\overline{q} \to W\gamma$ except for κ and λ, the scattering amplitude A of the s-channel diagram would have the form [16]

$$A \sim a + b\sqrt{s}(\kappa - 1 + \lambda) + cs\lambda$$

where a, b, and c are parameters independent of the center of mass energy ($\sqrt{s}$). It is obvious that the value of the scattering amplitude will grow as $\sqrt{s}$ increases whenever κ and λ do not have their Standard Model values. This is *not* allowed by tree-level unitarity which uniquely restricts the $WW\gamma$ couplings to their Standard Model gauge theory values at asymptotically high energies [17].

The problem of unitarity violation is avoided by the introduction of *form factors* to dampen the growth of the scattering amplitude at high energies. The form factors are chosen such that

$$\lambda \rightarrow \frac{\lambda}{\left(1+\frac{\hat{s}}{\Lambda^2}\right)^n} \quad \text{and} \quad (\kappa - 1) \rightarrow \frac{(\kappa - 1)}{\left(1+\frac{\hat{s}}{\Lambda^2}\right)^n}$$

Similar form factors are used for studies of the CP–violating parameters. It is conventional to use dipole form factors ($n = 2$).

The physical meaning of the parameter Λ is a *form factor scale* at which new physics might manifest itself. Λ is a phenomenological parameter that must be chosen prior to setting the limits on anomalous couplings. Unitarity itself sets the bounds on the anomalous $WW\gamma$ couplings[10] to be [16]

$$|\Delta\kappa| < 7.4 \text{ TeV}^2/\Lambda^2$$

$$|\tilde{\kappa}| < 35 \text{ TeV}/\Lambda$$

$$|\lambda|, |\tilde{\lambda}| < 4.0 \text{ TeV}^2/\Lambda^2$$

Λ should not be set too low, i.e. $\Lambda \approx m_W$, since no composite structure of the W boson (or any other manifestation of new physics) is observed at this scale, and the standard non-anomalous GWS theory has proven to be extremely accurate (q.v. Table 2.5.).

2.3.1 Signatures of W bosons and $W\gamma$ events

W bosons are quite massive when compared to the other elementary particles. They were not observed directly until particle accelerators could collide

[10]Here, and elsewhere in this paper, $\Delta\kappa \equiv \kappa - 1$.

protons and antiprotons with sufficient energy to produce them. After production, W bosons quickly decay into either leptons, e.g. $W \rightarrow e\nu$, or into quark-antiquark[11] pairs, e.g. $W \rightarrow ud$.

Quark decays ($W \rightarrow q\overline{q}$) result in two jets[12] of hadrons that point back to a common vertex. This $W \rightarrow$ dijet signal is extremely difficult to extract from the much more common hadronic jets that result from QCD processes, although it is not impossible [18]. Of the leptons, the τ is much too short-lived to observe directly[13], although attempts are underway to extract a $W \rightarrow \tau\nu$ signal at DØ.

The decays of W bosons into electrons or muons are the cleanest signals for observation and measurement. The branching ratio (BR) for W decays to a single lepton channel (e.g. $W \rightarrow e\nu$) is $(10.7 \pm 0.5)\%$ [5]. Each of the leptons from $W \rightarrow e\nu$ or $W \rightarrow \mu\nu$ carries roughly one-half the energy of the W boson. Detectors can be built to observe energetic electrons and muons. Neutrinos, with neither electric charge nor color, will interact only weakly with a particle detector, but they can be indirectly observed in the form of missing energy. Leptonic W boson decays have been observed at many experiments [19] [20] [21]. For the moment the direct study of W bosons is restricted to those produced through quark-antiquark annihilation at $p\overline{p}$ machines[14]. Eventually, W bosons will be studied at the e^+e^- collider LEP

[11] A careful reader may have already noticed the somewhat haphazard notation applied to the mediators, particles and antiparticles (especially with regard to electric charge) in many of the equations used so far. From here on, the convention of not explicitly distinguishing between a particle and its antiparticle is followed. It is assumed that charge is conserved in every equation.

[12] Liberated quarks instantly pull additional quarks and antiquarks from the vacuum in a process known as *hadronization*. The result is a highly collimated spray of hadrons (e.g. pions, protons, and neutrons) referred to as a jet.

[13] The τ also prefers to decay into jets; only 36% of all τ decays are into muons or electrons.

[14] The first observation of indirectly produced W bosons at HERA has been reported [22].

II, which is expected to have a center-of-mass energy above the threshold for W-pair production.

The DØ collaboration has measured the $\sigma(p\overline{p}\rightarrow W) \times \mathrm{BR}(W \rightarrow e\nu)$ to be 2.36 ± 0.15 nb at $\sqrt{s} = 1.8$ TeV , which is in good agreement with CDF [23]. The Standard Model prediction[15] for $\sigma(p\overline{p}\rightarrow W\gamma) \times \mathrm{BR}(W \rightarrow e\nu)$ is 12 ± 1 pb, almost two-hundred times smaller! $W\gamma$ events will look just like events with a W boson, except that there will be an additional photon found in the detector.

2.3.2 Characteristics of $W\gamma$ Events

Once the $W\gamma$ signal is observed it is necessary to examine some characteristic of $W\gamma$ events to decide if anomalous $WW\gamma$ couplings exist. The most natural feature to consider is the total number of $W\gamma$ events observed. Any anomalies in the $WW\gamma$ couplings will manifest themselves as an excess of events over what the Standard Model predicts, because of the additional contribution from the s-channel diagram. See Figure 2.2.

This excess of events manifests itself most obviously in the p_T spectrum[16] of the photon (p_T^γ). If non–standard couplings exist, the cross section for high p_T photons increases drastically. See Figure 2.3. The tightest limits on anomalous $WW\gamma$ couplings will be set by a careful study of this spectrum.

It is somewhat easy to determine which diagrams (of Figure 2.1) are responsible for a given $W\gamma$ event on the basis of several other quantities. The

[15] It is necessary to put a minimal set of cuts on the photon in $W\gamma$ events when quoting cross section predicitions. In this work the standard DØ requirement that photons have a minimum E_T of 10 GeV is made. Additionally all photons are considered to be well separated from the decay electrons; $\Delta R_{e\gamma} > 0.7$. Because of this last requirement the leptonic branching ratio is always included in all quoted $W\gamma$ cross sections.

[16] The transverse energy (and momentum) of particles is described in Section 3.2.

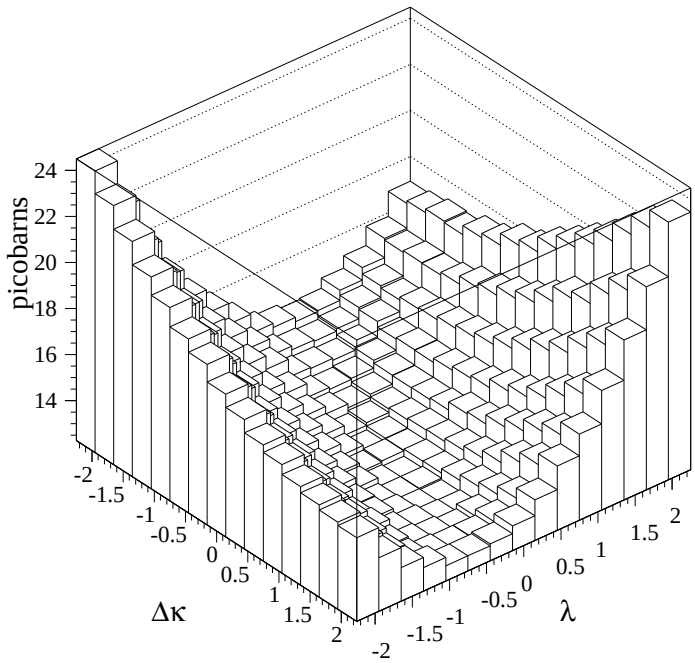

Figure 2.2. The cross section for $p\overline{p} \to W(e\nu)\gamma$ as a function of two coupling parameters. Only the effect of the photon kinematic cuts has been included. Notice the dramatic increase away from the standard model values of $\Delta\kappa = \lambda = 0$. The cross sections were produced with the DØBAUR generator which is described in Section 3.8.

t-channel and u-channel ISR diagrams tend to have photons that are more spatially separated from the W boson decay products than in the case of the decay diagram. The decay diagram is due to bremsstrahlung of the photon from the electron, so the three-body transverse mass of decay events will be reconstructed to be near that of the W boson, while the production diagrams will have a three-body transverse mass reconstructed to be higher than the transverse mass of the W boson.

An interesting feature of $W\gamma$ events is the so-called *radiation zero*[17] (RAZ).

[17] An excellent detailed introduction for this subject exists [24]. This reference also serves as a good pointer to additional references.

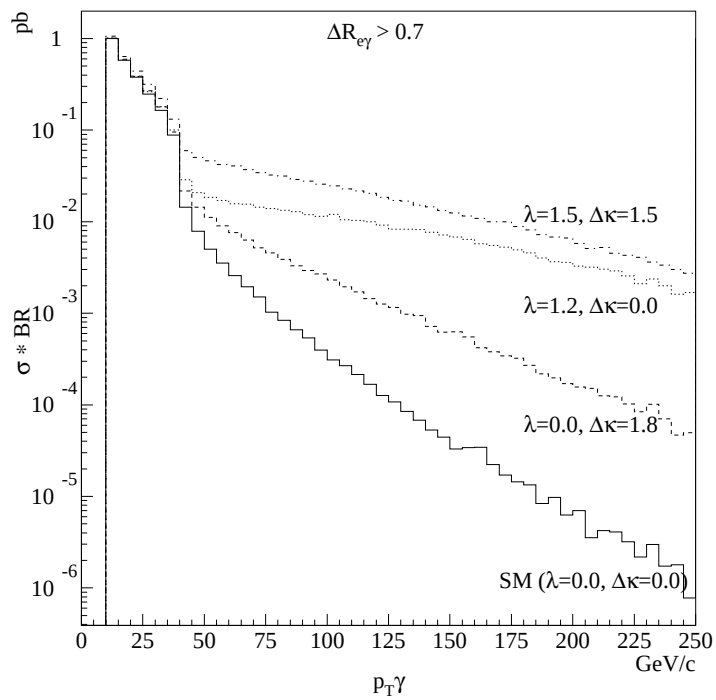

Figure 2.3. Typical $d\sigma/dp_T^\gamma$ spectrum for different anomalous coupling constants in $p\overline{p} \to W(e\nu)\gamma$. Only the effect of the photon kinematic cuts has been included.

The RAZ is the point in phase space where the standard model $W\gamma$ differential cross section vanishes. A dip in the scattering angle (θ^*) occurs at $\cos\theta^* = -1/3$ for W^+ and at $\cos\theta^* = +1/3$ for W^-. θ^* is the scattering angle of the photon relative to the quark direction, in the $W\gamma$ center-of-mass frame. The RAZ is due entirely to the the direct trilinear $WW\gamma$ coupling shown in Figure 2.1 (c). The similar process $q\overline{q} \to Z\gamma$ has no direct $ZZ\gamma$ or $Z\gamma\gamma$ coupling in the Standard Model, so there is no corresponding RAZ to be found in $Z\gamma$ events.

The observation of the RAZ would be another triumph for the GWS theory, but the search for the RAZ is not without difficulties [25]. First, the decay diagrams do not exhibit the RAZ, and must be eliminated; this is done by

requiring the three-body transverse mass be above the mass of the W boson. This will eliminate most decay events but a tiny fraction will remain. Second, the unobservable neutrino longitudinal momentum has a two-fold ambiguity. The effect of choosing the wrong longitudinal momentum for the neutrino has the same effect on the RAZ as any remaining decay events; the RAZ is slightly filled in. Third, due to the small number of remaining $W\gamma$ events, any experiment will have to use both W^+ and W^-, which will shift the RAZ to $|\cos\theta^*| = 0$. Finally, the RAZ in $W\gamma$ is only exact for the leading order process. Jets from higher order QCD processes will spoil the cancellations that give rise to the RAZ and also fill it in. A veto on $W\gamma$ events with jets might be necessary to recover the RAZ.

It is important to make one remark about next-to-leading order (NLO) corrections, not only because of possible RAZ studies, but because the comparison of this work to the standard (and non-standard) models relies on a leading order (LO) Monte Carlo event generator. At Tevatron energies ($\sqrt{s} = 1.8$ TeV) the NLO corrections are quite modest, but at higher center-of-mass energies they become significant [26] due to the presence of a RAZ for the LO process. At Tevatron energies, NLO calculations show that all LO distributions can be scaled by a K–factor:

$$K = 1 + \frac{8\pi}{9}\alpha_s \approx 1.34$$

as a good approximation to NLO [26].

It is necessary to make one last remark about the measurement of the radiation zero from $W\gamma$ events. The current DØ detector has no central magnetic field to measure the charges of the leptons from W boson decays, which makes the reconstruction of the $W\gamma$ center-of-mass frame impossible. The RAZ also

manifests itself in the correlation between the rapidity[18] of the decay lepton and the rapidity of the photon [27], so there was some hope that the RAZ might still be observed at DØ. Unfortunately the rapiditiy correlation is not a strong enough to overcome the lack of charge identification at DØ; the W^+/W^- ambiguity washes out the RAZ.

2.4 Previous Studies of the $WW\gamma$ Interaction

There are three major experimental tests of the $WW\gamma$ vertex. The first is to set limits on ($\Delta\kappa$,λ) and ($\tilde{\kappa}$, $\tilde{\lambda}$)[19]. The second test is to measure the cross section times branching ratio for $W\gamma$ production. Finally, it is possible to look for the radiation zero.

2.4.1 Low-Energy, Indirect Tests

Several indirect tests of the $WW\gamma$ vertex exist. Such studies involve either precise measurements of electric or magnetic dipole moments or they are searches for rare electromagnetic quark decays. These low energy experiments are able to search for anomalous trilinear couplings because of various loop corrections such as "penguin" diagrams [22]. Consequently, these indirect tests are very sensitive to regularization schemes and loop cutoff parameters. A further difficulty with indirect tests is that the limits on anomalous couplings obtained from them have the shape of bands that stretch to infinity when both couplings are allowed to vary[20]. However, if one parameter is held fixed, the limits on the second parameter can be very tight.

[18] See Section 3.2 for the definition of rapidity and pseudorapidity.

[19] The pairs of CP–conserving and CP–violating parameters are considered independently.

[20] Direct tests from $W\gamma$ production produce closed contour limits because the total production cross-section for any pair of couplings is bilinear.

The tightest limits on $\Delta\kappa$ from an indirect test comes from the study of $b \to s\gamma$ events by the CLEO [28] experiment. The 95% confidence level (CL) limits on $\Delta\kappa$ (when $\lambda = 0$) are $-2.6 < \Delta\kappa < -1.2$ and $-0.6 < \Delta\kappa < 0.4$. A complicated interference in the model excludes the region $-1.2 < \Delta\kappa < -0.6$. The strongest indirect constraint on λ comes from the measurement of the magnetic moment of the muon [29], $|\lambda| < 5$. The tightest limits on the CP–violating parameter $\tilde{\lambda}$ are from the electric dipole of the neutron measurements [30]; $|\tilde{\lambda}| < 2.5 \times 10^{-4}$.

2.4.2 $q\overline{q} \to W\gamma$ at UA2

The first direct observation of the $WW\gamma$ interaction was at the CERN experiment UA2 [31]. $p\overline{p} \to e\nu\gamma$ events were studied at $\sqrt{s} = 630$ GeV. UA2 looked for $W \to e\nu$ events (in 13 pb^{-1} of integrated luminosity) with an extra photon of $p_T^\gamma > 4.5$ GeV/c. 16 events were found with an estimated background of 6.8 ± 1.0 events. All of the photons were found to have p_T below 15 GeV/c. From the p_T^γ spectrum the following limits on anomalous couplings were found (at 95% CL):

$$-4.5 < \Delta\kappa < 4.9 \text{ for } \lambda = 0,$$

$$-3.6 < \lambda < 3.5 \text{ for } \Delta\kappa = 0.$$

2.4.3 $q\overline{q} \to W\gamma$ at the Tevatron

Both CDF and DØ have observed $W\gamma$ events in both the electron and muon decay modes of W bosons produced at $\sqrt{s} = 1.8$ TeV. CDF required photons to have p_T^γ above 7 GeV/c in the pseudorapidity range $|\eta| < 1.0$. CDF [32] observed 75 electron events and 34 muon events in approximately

67 pb^{-1} of data (from Tevatron Run 1a and part of Run 1b.) The background was estimated to be 26.4 events. From the p_T^γ spectrum the following limits were set (at 95% CL):

$$-1.8 < \Delta\kappa < 2.0 \text{ for } \lambda = 0,$$

$$-0.7 < \lambda < 0.6 \text{ for } \Delta\kappa = 0.$$

CDF has searched for the radiation zero by limiting their sample to production $W\gamma$ events. This leaves a sample of 17 events with 3.5 background. With these statistics there were not enough events to observe the radiation zero.

The previous DØ results [33] used 13.8 pb^{-1} of data from Run 1a. The analysis is similar to CDF (both experiments require $\Delta R_{e\gamma} > 0.7$ in $\eta - \phi$ space, and both assume a form factor scale of $\Lambda = 1.5$ TeV) but DØ only allows photons with p_T^γ above 10 GeV/c. However, the DØ detector provides photon detection in the forward pseudorapidity region $1.5 < |\eta| < 2.5$. Combining both the electron and muon decay channels, DØ had 23 events with a background of 6.4 events. The limits on anomalous couplings (from p_T^γ) were measured to be:

$$-1.6 < \Delta\kappa < 1.8 \text{ for } \lambda = 0,$$

$$-0.6 < \lambda < 0.6 \text{ for } \Delta\kappa = 0.$$

Of the 23 events, 7 qualify as production events. No attempt was made to observe the radiation zero at DØ. See Appendix A for more details on the DØ Run 1a analysis.

Both CDF and DØ set limits on the CP–violating couplings similar to their reported limits on the CP–conserving parameters. DØ's tighter limits are partially due to the higher rapidity coverage, and partially due to better

understanding of the backgrounds to $W\gamma$, especially at the high end of the p_T^γ spectrum. Because of these two factors, we can expect that the results from the combined DØ Run 1a and 1b work will be the most stringent direct measurement of the $WW\gamma$ coupling that any single experiment can hope to produce for a long time[21].

The prospects for a combined DØ/CDF analysis are quite good. DØ will not be able to assist CDF when looking for the RAZ, but the limits on anomalous couplings can be significantly improved by combining the statistics from each experiment.

[21]The improvement in limits on $\Delta\kappa, \lambda$ scale roughly with an increase of data to the $\frac{1}{4}$ power, for the same $\sqrt{s}$. That is, 1 fb^{-1} (= 1000 pb^{-1}) of data at the Tevatron would improve the Run 1a DØ limits (from $\sim$ 10 pb^{-1}) by a factor of 3. Estimates are that 500 pb^{-1} of data from LEP II ($e^+e^- \rightarrow W^+W^-$ at $\sqrt{s}$ = 176 GeV), may be able to set limits on $|\Delta\kappa|, |\lambda|$ of approximately 0.2 [34]. Each of these two scenarios will take many years to accomplish.

CHAPTER 3

EXPERIMENTAL APPARATUS

The Tevatron is currently the highest energy accelerator in the world. The DØ detector is a massive collection of sub-detectors which, through design or malice, has kept hundreds of scientists busy for many years, and as it is upgraded, it will continue to do so into the next decade. In this chapter, the major detector subsystems are described in Sections 3.3 through 3.5, followed by a short description of the data accquisition and event reconstruction software in Section 3.6. It is necessary to compare experimental data directly with theoretical predicitions. Monte Carlo simulations play an important part in this prediction, so the event generator of primary importance to this work is described in Section 3.8.

3.1 The Tevatron

In order to directly study the $WW\gamma$ interaction it is first neccesary to produce copious amounts of W bosons. Furthermore, this must be done in the vicinity of a detector designed to study both photons and the decay products of the short-lived W bosons. The Fermi National Accelerator Laboratory (FNAL) proton-antiproton collider (the *Tevatron*) is one of the few machines

capable of producing W bosons in the large numbers needed to study the $WW\gamma$ coupling. What follows is a brief discussion of the operation of the accelerator complex in colliding-beam mode. This is only a rudimentary introduction to the ingredients of a succesful colliding beam program. For a more details on the physics of colliding beams the reader is directed to other sources [35].

3.1.1 Tevatron Operation in Collider Mode

The accelerator complex[1] at FNAL actually consists of a series of machines that not only produces both protons and antiprotons but accelerates them to 900 GeV in preparation for head-to-head collisions at a center of mass energy ($\sqrt{s}$) of 1.8 TeV.

The first stage of this process takes place at a *Cockroft-Walton* accelerator. In this device, hydrogen gas is ionized with electrons to produce H^- ions. A static electric field then accelerates these ions to an energy of 750 keV, an energy about thirty times the energy of the electron beam inside a television picture tube. The H^- ions then enter a 150 meter long linear accelerator (the *Linac*) which uses oscillating electric fields to accelerate the ions to 400 MeV. At the end of the Linac the ions are passed through a carbon foil which strips the electrons from the H^- ions, leaving only positively charged protons.

These energetic protons then enter a 500 meter circumference syncrotron called the *Booster*. Electric fields accelerate the protons while magnets keep them traveling in a circular path. The Booster accelerates the protons to an energy of 8 GeV. When a significant amount of protons have been collected in the booster, one full *batch* of protons is then delivered to the next part of the

[1]Most of the information in this section comes from the wonderful note provided by J. Thompson [36].

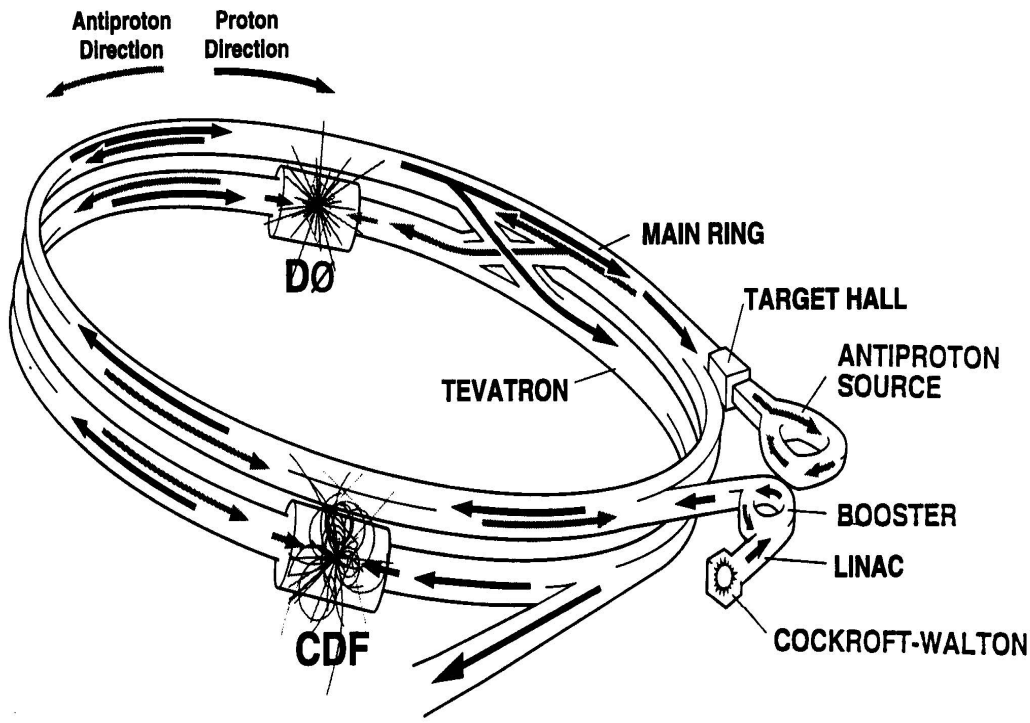

Figure 3.1. The Tevatron accelerator schematic layout.

machine, the *Main Ring*. The Main Ring is a much larger proton synchrotron (6.28 km circumference) which accelerates the protons to over 100 GeV. There is a short period of time after injection, approximately 400 msec long, referred to as *transition*, in which there is an instability in the beam transport which results in a loss of protons from the Main Ring. This is referred to as MRBS losses.

The Main Ring has two major purposes. It can either form bunches of $2 \cdot 10^{12}$ protons and accelerate them to an energy of 150 GeV after which they are injected into the final accelerator, the *Tevatron*, or 120 GeV protons can be dumped onto a nickel target disk to produce antiprotons. About 10^7 antiprotons are produced for every 10^{12} protons that hit this target. The antiprotons are focused by lithium magnet lenses into the *Debuncher*, a roughly

triangularly shaped machine that equalizes the energies of the antiprotons and collects them into a beam by a process known as *cooling*. The monoenergetic beam of antiprotons is then injected into the *Accumulator* ring for storage before the next batch of antiprotons arrives from the nickel target. When a large number of antiprotons is available, they are transferred back into the Main Ring, accelerated, and injected into the Tevatron.

The Tevatron is a synchrotron ring of one thousand superconducting magnets which accelerates six proton (antiproton) bunches to 900 GeV as they travel clockwise (counter-clockwise) around the ring. There are typically about 10^{11} ($5 \cdot 10^{10}$) protons (antiprotons) per bunch injected into the Tevatron. The Tevatron is located in the same structure as the Main Ring, but it is physically below the Main Ring. The proton and antiproton bunches are accelerated in the same tunnel, and after reaching the maximum energy, they are both scraped with a metal plate collimator to produce the clean beams that are then crossed at the BØ (CDF) and DØ interaction regions. These *stores* of bunches typically last 12-18 hours, and the recovery time between stores is on the order of two hours.

A common term used when describing the performance of the collider is *luminosity* ($\mathcal{L}$), the interaction rate per unit cross section. The luminosity is proportional to the frequency of bunch collisions, the number of protons in one bunch and the number of antiprotons in the bunch which hits the protons. It is inversely proportional to the cross sectional area of the two colliding bunches. During the Runs 1a and 1b periods of collider operation, the Tevatron typically operated at luminosities of the order $10^{31}\mathrm{cm}^{-2}\mathrm{s}^{-1}$. The total cross section for $p\overline{p}$ interactions is about $10^{-25}\mathrm{cm}^2$ or 100 millibarns (1 mb = $10^{-27}\mathrm{cm}^2$). So the average number of $p\overline{p}$ interactions is around *one million per second*! A more

informative way to characterize collider performance is to quote the luminosity integrated over time, which is typically described in terms of inverse picobarns. ($1\ \mathrm{pb}^{-1} = 10^{-12}\ \mathrm{barns}^{-1}$) During the course of Runs 1a and 1b, the Tevatron delivered over 100 pb^{-1} to DØ during Run 1b. Almost 90 pb^{-1} of data was written to tape in Run 1b.

While the Tevatron is running in colliding beam mode, the Main Ring continues its duties of manufacturing antiprotons in preparation for the next store. It is important to note that the physical location of the Main Ring requires that it pass through the upper portion of the DØ detector. As mentioned above, the periods of Main Ring injection from the Booster (MRBS) is a very noisy period in the Main Ring.

Additionally, the DØ detector in the area of the Main Ring is quite noisy when the 120 GeV protons travel past as they go towards the antiproton source. As a result, DØ can either stop recording data during the periods of Main Ring activity near the detector or events can be flagged as Main Ring events when they are passed through the trigger sytem. Of the Tevatron's 2.4 second cycle, approximately 0.4 seconds are lost at DØ due to MRBS while another 0.1 seconds are lost due to the protons travelling towards the antiproton source. This results in a dead-time (or lost luminosity) of about 21%. The amount of lost time per store is not fixed, as it depends on the activity of the Main Ring.

3.2 The DØ Detector

The DØ detector was designed to take data while the Tevatron is operating in colliding beam mode with $\sqrt{s} = 1.8$ TeV. The original proposal for the DØ experiment was in 1983, and the detailed design and assembly took place

between 1985 and 1992. The first $p\overline{p}$ collisions were recorded at DØ on May 12, 1992. The first full run of the experiment, *Run 1a*, took place between August 21, 1992 and May 31, 1993 and recorded 15 pb^{-1} on tape. The second full run, *Run 1b*, took place between December 1993 and July 25, 1995 which recorded an additional 87 pb^{-1} of data on tape.

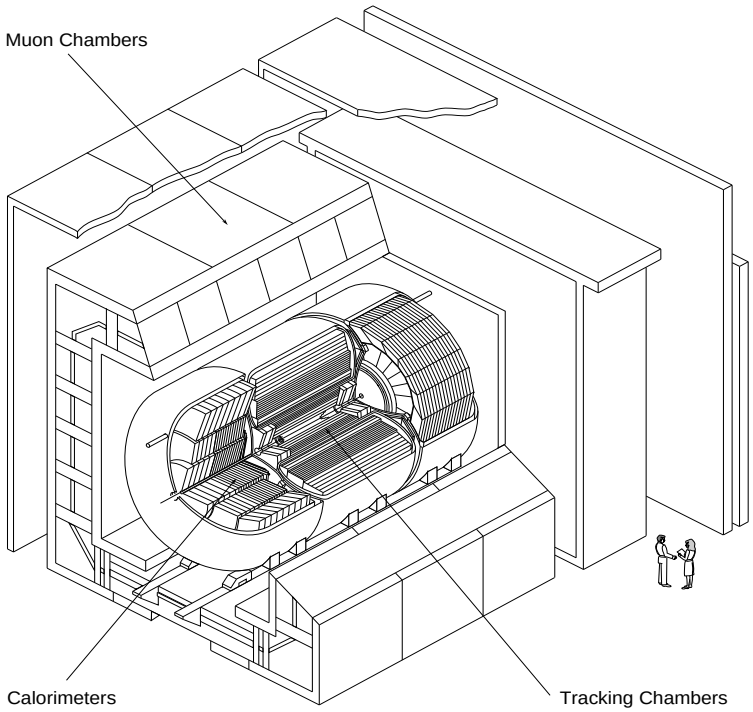

Figure 3.2. Overview of the DØ detector

The DØ detector was designed as a general purpose detector with the following goals in mind:

- Identification and measurement of electrons, photons and muons.
- Identification and measurement of parton jets.
- Measurement of missing transverse energy as a means of signalling the presence of non-interacting particles, e.g. neutrinos.

The general design of the DØ detector is as follows[2]: Tracking chambers are located as close as possible to the interaction point. Like the CERN $p\overline{p}$ experiment UA2 [38] a decade earlier, DØ does not have a central magnetic field to bend the trajectories of charged particles, so the calorimeter begins almost where the central tracking chambers end. Without a central magnetic field (and the ability to measure particle momenta it would provide), the calorimeter is the only device capable of measuring the energy of particles. Beyond the calorimeter is the muon tracking system which does include a toroidal magnet for the measurement of muon momentum. The full detector is approximately 13 m high $\times$ 11 m wide $\times$ 17 m long and has a total weight of 5500 tons.

When describing the geometry of the DØ detector a right-handed coordinate system is used. The z-axis is along the proton direction and the y-axis is upward. The angles ϕ and θ are the azimuthal and polar angles, respectively. ($\theta = 0$ along the proton direction.) The r-coordinate denotes the perpendicular distance from the beam axis. Quite often the variable pseudorapidity (η) is used when refering to the dimensions of the detector. Pseudorapidity, $\eta \equiv -\ln(\tan(\theta/2))$, approximates the true rapidity $y = 1/2 \ \ln((E+p_z)/(E-p_z))$, for finite angles in the limit that $(m/E) \rightarrow 0$. Most of the particles in the DØ detector are described in terms of their transverse energy (E_T), which is the energy of a particle particle in the $x-y$ plane.

What follows is a general explanation of the various elements of the DØ detector followed by the specific details of that particular system.

[2]A more detailed description of the DØ detector can be found elsewhere [37].

3.3 Calorimetry

The DØ liquid argon sampling calorimeter is in many ways the heart of the experiment. A calorimeter is a device which measures the total energy of an incident particle because of the particle's interaction with the material of the calorimeter. Only particles that interacts electromagnetically (e.g. electrons, photons) or strongly (e.g. mesons and hadrons, which are composed of quarks) with matter are capable of depositing significant energy in a calorimeter.

An understanding of the difference between the electromagnetic and strong interactions in matter is crucial to understanding the design of high-energy physics calorimeters. Each type of interaction leads to the development of a *shower* of secondary particles inside the calorimeter. Since the particle showers generated by the different interactions are quite different, a *sampling calorimeter* can take advantage of these differences. Consequently, the DØ calorimeter is divided into two parts, an electromagnetic (EM) calorimeter and a hadronic calorimeter.

A sampling calorimeter is a device which measures the energy of a shower in several different places along the development of the shower rather than measuring the total energy all at once, e.g. as in a sodium iodide crystal. Sampling calorimeters are not homogeneous; one high-density material (the *absorber*) generates the shower from incident particles while another material acts as the active readout. This design takes advantage of different types of shower developments from different particles with varying energies. Because the showers are only sampled at discrete points, *sampling fractions* are necessary to estimate the amount of energy lost in the absorber which is not seen in the active region.

The dominant process in an EM calorimeter is either bremsstrahlung (for electrons and positrons) or electron-positron pair-production by high energy photons[3] [39]. The result of an incident electron or photon of high energy (above 1 GeV) entering a calorimeter is an electromagnetic shower consisting of a mixture of photons and electrons with energy being converted to and from the different types. It is important to note that showers develop laterally as well as along the original direction of the incident particle.

At high energies, bremsstrahlung, the dominant means of energy loss from EM interactions, explains why muons, relatively long-lived particles very similar to the electron, escape the entire calorimeter with only depositing a small amount of energy through ionization. Particles other than electrons and photons do not readily initiate electromagnetic showers as the rate for bremsstrahlung is proportional to to the inverse square of the particle's mass, and other charged particles are much too heavy [40]. Particles which decay into photons before they reach the calorimeter, such as the π^0 or η, will initiate EM showers, so care must be taken when identifying particles from an EM shower[4].

The average size of an EM shower, both transverse and longitudinal, depends on the radiation length (X_0) of the absorber, while the size of a hadronic shower depends on the nuclear absorption length (λ_a). The radiation length in heavy materials is much smaller than the nuclear absorption length, so EM calorimeters are of necessity placed before hadronic ones. Strongly interacting particles shower through many interactions with nuclei in the absorber ma-

[3]Recall that throughout this paper, "electron" refers to both the positively and negatively charged members of the species.

[4]Because of their similar EM showers, discrimination of photons from electrons is only possible with the use of the central tracking system. See Section 4.2 for more details.

terial. This is much more complex than the processes of bremsstrahlung and pair-production which dominate EM showers! Furthermore, it is frequently the case that as a hadronic shower develops, secondary π^0s (recall that they quickly decay electromagnetically into two photons) lead to many EM showers within a hadronic shower! This becomes a problem if the response of a calorimeter is different between EM and hadronic showers.

Typically, the resolution of a calorimeter is is limited by inherent fluctuations in shower generation, but sampling calorimeters have other sources of fluctuations:

- A sampling calorimeter looks at discrete points along the development of a shower, so *intrinsic fluctuations* in the energy carried by decay products is enhanced, especially in the case of pair-production.

- Particles that scatter into the plane of the detector will give rise to large *path-length fluctuations*. More energy will be deposited by a particle moving transverse to the detector than one passing longitudinally through it.

Both of these effects enhance the response of a calorimeter to EM showers (typically by a factor of 40%), so care must be taken to equalize the hadronic response to the EM response. This is done at DØ using the *uranium compensating calorimeter* concept. Much has been written about the history of this approach [41] and will not be repeated here, except to say that depleted uranium works well to normalize EM and hadronic response because as a high-Z absorber it decreases EM response rather than increasing hadronic response as originally suspected.

The DØ calorimeter uses depleted uranium absorbers with varying thick-

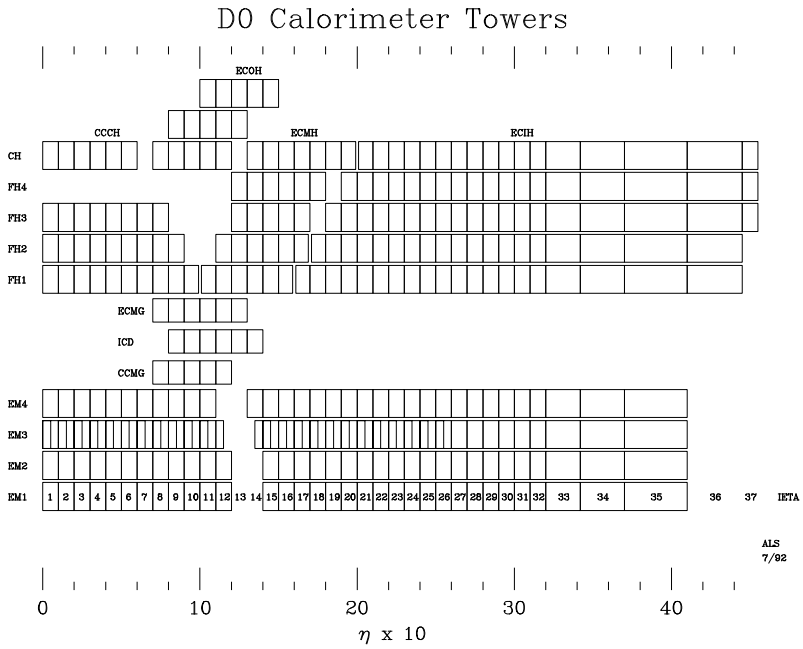

Figure 3.3. Longitudinal arrangement of the calorimeter, showing the cell size as a function of pseudorapidity (η).

nesses for the EM and inner hadronic (referred to as the *Fine Hadronic* or FH) layers, while stainless steel and copper serve as absorbers in the outer (*Coarse Hadronic* or CH) layers. Liquid argon serves as the active medium for the DØ calorimeters, which requires a large cryogenic system. The EM, FH and CH are further divided longitudinally into layers and transversely segmented into readout towers, as shown in Figure 3.3.

These cells are arranged with a *pseudo-projective* geometry, as shown in Figure 3.4. That is, the centers of the each cell points towards the interaction vertex, even while the cell boundaries are perpendicular to the absorber plates.

3.3.1 Central Calorimeter

The CC has a length of 2.6 m covering the pseudorapidity interval $|\eta| <$

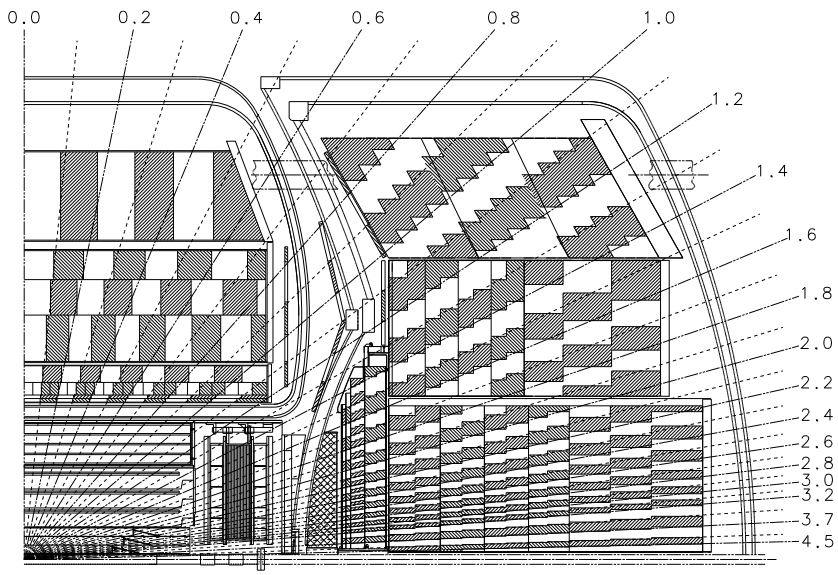

Figure 3.4. Side view of one-fourth of the calorimeter, showing the projective cell structure for successive layers. The lower left corner of the the diagram is the center of the detector. Notice the passage of the Main Ring through the top of the detector. The numbers indicate units of pseudorapidity.

1.2 and consists of three elements, an electromagnetic calorimeter (EM) with four layers, a fine hadronic calorimeter (FH) with three layers, and a coarse hadronic (CH) calorimeter. The details of the Central Calorimeter (CC) are listed in Table 3.1.

Of primary importance to the Wγ analysis are the four layers of the EM calorimeter (CCEM). The segmentation of layers 1, 2 and 4 is 0.1×0.1 in η-ϕ. The third EM layer (EM3) is located at the depth at which electromagnetic showers from 30 GeV electrons produce the maximum number of secondary particles. EM3 has a finer transverse segmentation (0.05×0.05) than the other EM layers. The transverse and longitudinal profile of electromagnetic showers is critical in discriminating between electrons/photons and neutral meson decays to two photons. The four EM layers together cover almost 21

radiation lengths. This is deep enough to contain almost all EM showers.

Table 3.1. Parameters of the DØ Central Calorimeter

Module Type	**EM**	**FH**	**CH**
Pseudorapidity Coverage (η)	± 1.2	± 1.0	± 0.6
Absorber Material	U	U (1.7% Nb)	Cu
Absorber Thickness (mm)	2.3	2.3	46.5
Number of Readout Layers	4	3	1
Depth per Readout Layer	2, 2, 7, 10 X_0 (0.76 λ_a)	1.3, 1.0, 0.9 λ_a	3.2 λ_a
Total Radiation Lengths (X_0)	21	96	33
Total Nuc. Abs. Lengths (λ_a)	0.76	3.2	3.2
Sampling Fraction	11.79%	6.79%	1.45%
Segmentation ($\Delta\eta \times \Delta\phi$)	0.1×0.1 (Layers 1,2,4) 0.05×0.05 (Layer 3)	0.1×0.1	0.1×0.1
Total Number of Channels	10,368	3000	1224

3.3.2 Endcap Calorimeters

DØ uses a pair of Endcap Calorimeters (EC) to cover the detection of electromagnetic and hadronically decaying particlles in the pseudorapidity interval $1.1 < |\eta| < 4.5$; these particles can only escape the detector in the extreme forward regions (large $|\eta|$) or through tiny cracks between cells. This makes the DØ detector almost completely hermetic and allows for a very accurate measure of missing transverse energy.

The EC consists of an electromagnetic layer (ECEM), an inner fine hadronic layer (IFH), an inner coarse hadronic layer (ICH), a middle fine hadronic (MFH) layer, a middle coarse hadronic (MCH) layer, and an outer coarse hadronic layer (OCH). The coarse hadronic layers use stainless steel as an absorber while the other layers use uranium, as in the CCEM and CCFH. (The

CCFH uses a uranium-niobium alloy.)

The ECEM provides pseudorapidity coverage in the region $1.5 < |\eta| < 2.5$. As in the CCEM there are four layers. EM1, EM2, and EM4 are again segmented 0.1×0.1 in η-ϕ while EM3 has the finer transverse segmentation of 0.05×0.05. In the region $|\eta| > 3.2$ the transverse cell segmentation increases to a maxium of 0.4×0.4. See Table 3.2 for more details.

Table 3.2. Parameters of the DØ Endcap Calorimeters

Module Type	**ECEM**	**IFH**	**ICH**
Pseudorapidity Range (η)	$\pm$ (1.3–4.1)	$\pm$ (1.6–4.5)	$\pm$ (2.0–4.5)
Absorber Material	U	U (1.7% Nb)	Steel
Absorber Thickness (mm)	4.0	6.0	46.5
Number of Readout Layers	4	4	1
Total Depth	20 X_0 (0.95 λ_a)	4.4 λ_a	4.1 λ_a
Sampling Fraction	11.9%	5.7%	1.5%
Total Number of Channels	7488	4288	928
Module Type	**MFH**	**MCH**	**OH**
Pseudorapidity Range (η)	$\pm$ (1.0–1.7)	$\pm$ (1.3–1.9)	$\pm$ (0.7–1.4)
Absorber Material	U (1.7% Nb)	Steel	Steel
Absorber Thickness (mm)	6.0	46.5	46.5
Number of Readout Layers	4	1	3
Total Depth	3.6 λ_a	4.4 λ_a	4.4 λ_a
Sampling Fraction	6.7%	1.6%	1.6%
Total Number of Channels	1856	384	960

3.3.3 Intercryostat Detector and Massless Gap Detector

Between the Central and Endcap Calorimeters ($0.8 < |\eta| < 1.5$) is a region of unistrumented material mostly in the form of cryostat walls and support structures. The material profile along a particle path varies rapidly with rapidity through this region. To correct for energy deposited in the uninstrumented

walls there are two scintillation counter arrays, segmented in η-ϕ with 0.1×0.1, called intercryostat detectors (ICD). Additionally three rings of massless gap (MG) detectors are mounted on the surfaces of CCFH, MFH and OCH modules. The MG detectors are readout boards surrounded by liquid argon with no absorbers. Together, the ICD and MG provide a good approximation to the standard DØ sampling of EM showers.

3.4 Central Tracking

As mentioned earlier, the DØ detector does not have a central magnetic field. While this prevents the measurement of the charge and momentum of produced particles, the central tracking chambers are still a vital part of the DØ detector. The presence of a charged track in the central tracker which points towards an electromagnetic shower in the calorimeter is the primary means of distinguishing electrons from photons. The DØ central tracker also measures the trajectory of muons, aiding in identification of that particle. Other information, such as the number of tracks pointing towards an electromagnetic cluster and the ionizing energy lost along a track (dE/dx) can be used to distinguish between electrons and converted photons/pions. Even when complete tracks are not reconstructed from observed hits in the tracking chambers, this information can also be used as an extra means of differentiating photons from pions. Central tracks are also used to reconstruct the z-postion of the primary interaction point as well as any secondary vertices.

The DØ Central Detector (CD) is composed of four independent subsystems. The Vertex Drift Chamber (VTX) is closest to the interaction region. The Transition Radiation Detector (TRD) and Central Drift Chamber (CDC)

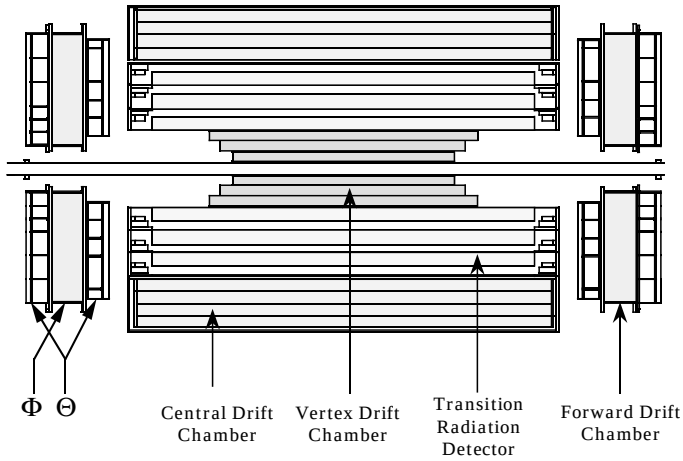

Figure 3.5. Side view of the the DØ central tracking system.

extend outward from the VTX towards the Central Calorimeter. Two Foward Drift Chambers (FDC) provide tracking in the forward region before the End-cap Calorimeters. The CD extends from $z = \pm 135$ cm to $r = 78$ cm. While this analysis only takes advantage of the information provided by the CDC and FDC, future studies that require additional rejection may take advantage of the TRD and VTX detectors. For this reason all four systems will be briefly discussed.

3.4.1 Vertex Drift Chambers

The Vertex Chamber (VTX) was originally designed to identify secondary vertices from heavy (charm, bottom) quark decays. It also serves as a complimentary tool for track reconstruction, dE/dx measurement and vertex identification.

It is the innermost tracking chamber in the DØ detector, extending from an inner radius of 3.7 cm (the outer radius of the beryllium beam pipe which contains the $p\overline{p}$ interactions) to an outer radius of 16.2 cm. The VTX is a

drift chamber consisting of three mechanically independent concentric layers of cells. The innermost layer has sixteen cells while the outer two layers have thirty-two cells each.

Table 3.3. Parameters of the DØ Vertex Drift Chamber

Parameter	**Specification**
Radius	3.7 cm - 16.2 cm
Overall Length	116.8 cm
Number of Layers	3
Number of Cells	16,32,32 (for Layers 1,2,3)
Number of Sense Wires	8 per cell (640 total)
Sense Wire Voltage	+2.5kV
Drift Field	1 kV/ cm
Gas Type	95% CO_2 + 5% ethane + 0.5% H_2O
Gas Gain	4×10^4
Spatial Resolution	$r\phi \simeq 60$ μm, $z \simeq 1.5$ cm

3.4.2 Transition Radiation Detector

DØ's Transition Radiation Detector (TRD) occupies the volume between the VTX and CDC; it extends from a radius of 17.5 cm to 49 cm. The TRD is capable of providing an independent identification of electrons and converted photons from $\pi^0 \rightarrow \gamma\gamma$ decays. The TRD was not used in the analysis described here; other means of particle identification proved to be sufficient for the selection of $e\nu\gamma$ events. It is likely that TRD information will be used in future analyses that require higher rejection of converted photons.

Transition radiation x-rays are emitted when relativistic ($\gamma > 10^3$) charged particles cross boundaries between media with different dielectric constants. The DØ TRD consists of three separate layers. Each layer has a radiator

section (393 foils of 18 μm thick polypropylene) followed by an x-ray detection chamber. The x-rays produced in the DØ TRD have a distribution that peaks at 8 keV and is mainly contained below 30 keV.

Table 3.4. Parameters of the DØ Transition Radiation Detector

Parameter	**Specification**
Radius	17.6 cm - 47 cm
Overall Length	165 cm
Number of Layers	3
Number of Sense Wires	256 per layer
Sense Wire Voltage	+1.6 kV
Drift Field	0.7 kV/cm
Gas Type	Radiation Chamber - N_2
	Gap - CO_2
	Drift Chamber - 95% Xe + 7% CH_4 + 2% C_2H_6
X-ray energy	< 30 keV

3.4.3 Central Drift Chamber

The Central Drift Chamber (CDC) provides track information for charged particles produced with $|\eta| < 1.2$. It extends radially from the outer surface of the TRD (49.5 cm) to the inner radius of the CC (74.5 cm). The CDC consists of 4 concentric rings of 32 azimuthal cells per ring. Cells in adjacent layers are staggered in ϕ by one half cell to improve pattern recognition and track reconstruction.

The measurements of $r\phi$ rely on the anode wires which run parallel to the beam direction. The z position of a track point is measured twice in each layer with delay lines located just before the first and just after the last sense wire of each cell. The spatial resolution is 2 mm in the z direction and 150 μm

in the $r\phi$ plane. A single layer of 128 scintillating fibers was installed on the CDC support cylinder for precise calibration of the CDC drift velocities.

In addition to measuring the position of tracks from charged particles, the CDC is capable of measuring the energy lost (dE/dx) along the track. This information can be used as an extra tool for discriminating electrons from converted photons. However, as in the case of the TRD, the dE/dx information was not used for this analysis as other tools provided sufficient rejection of pions.

Table 3.5. Parameters of the DØ Central Drift Chamber

Parameter	**Specification**
Radius	51.8 cm - 71.9 cm
Overall Length	179.4 cm
Number of Layers	4
Number of Cells	32 per layer
Number of Sense Wires	7 per cell (896 total)
Sense Wire Voltage	+1.45 kV (inner sense wires)
	+1.58 kV (outer sense wires)
Drift Field	620 V/cm
Drift Velocity	34 μm/ns
Gas Type	93% Ar + 4% CH_4 + 3% CO_2 + 0.5% H_2O
Gas Gain	2×10^4 (inner sense wires)
	6×10^4 (outer sense wires)
Spatial Resolution	$r\phi \simeq 180$ μm, $z \simeq 2.9$ mm

3.4.4 Forward Drift Chambers

A Forward Drift Chamber (FDC) is located at each end of the VTX/TRD/CDC barrel (z = 104.8 cm) and extends to the front of the EC cryostat (z = 135.2 cm). The FDC's radial coverage extends from 11 cm to 62 cm. These two mirror-image chambers extend the tracking coverage up to $|\eta| < 3.1$. Each

FDC consists of three separate chambers stacked perpendicular to the beam axis. Two Θ modules measure the polar angles of tracks from charged particles. A single Φ module is sandwiched in between the Θ modules; it has radial wires and measures the ϕ coordinate of the tracks.

Each Θ module consists of four mechanically separate quadrants, each containing six rectangular cells at increasing radii. All the cells have eight sense wires and one delay line. The Φ module is a single chamber containing 36 sectors covering the entire ϕ range; each Φ sector has 16 sense wires.

Table 3.6. Parameters of the DØ Forward Drift Chambers

Parameter	**Specification**
Radius	11 cm - 62 cm
Overall Length	$z = \pm$(104.8 cm - 135.2 cm)
Number of Modules	6 (4 Θ, 2 Φ)
Number of Cells	24 in each Θ module
	36 in each Φ module
Number of Sense Wires	8 per cell in each Θ module
	16 per cell in each Φ module
Sense Wire Voltage	+1.55 kV Θ modules
	+1.66 kV Φ modules
Drift Field	1 kV/cm
Drift Velocity	40 μm/ns Θ modules
	37 μm/ns Φ modules
Gas Type	93% Ar + 4% CH_4 + 3% CO_2 + 0.5% H_2O
Gas Gain	2.3×10^4 inner Θ sense wires
	5.3×10^4 outer Θ sense wires
	3.6×10^4 Φ sense wires
Spatial Resolution	$\theta \simeq 300$ μm, $\phi \simeq 200$ μm

3.5 Outer (Muon) Tracking

Muons are leptons similar to electrons; each interacts through only the

weak or electromagnetic forces. Muons are over 200 times more massive than electrons, and since the cross section for bremsstrahlung depends inversely on the square of the particle mass, muons will not be identified in the electromagnetic part of the calorimeter. The energy lost from muons will be mostly due to the ionization of the detector media. The minimum momentum required for a muon to pass through the entire DØ detector varies from 3.5 GeV/c at $\eta = 0$ to 5.0 GeV/c at higher η. For this reason the muon detectors are placed outside the calorimeter, which absorbs the debris from hadronic and electromagnetic showers.

The DØ muon system consists of five separate solid-iron toroidal magnets and several layers of proportional drift tube (PDT) chambers to measure track coordinates to approximately three degrees. One central toroid (CF) covers the pseudorapidity range $|\eta| < 1.0$, two end toroids (EF) extend the coverage from $1.0 < |\eta| < 2.5$. These three toroids, and the PDTs which accompany them, are referred to as the Wide Angle Muon System (WAMUS). Two Small Angle Muon Systems (SAMUS) further extend the pseudorapidity coverage from $2.5 < |\eta| < 3.6$.

Inside each of these magnets (which produce a field of about 2 T) is a single layer of PDT chambers, referred to as the 'A' layer. Two more layers of PDTs are beyond the toroids; first the 'B' layer and then, after a gap of 1-3 m, the 'C' layer. The A layer consists of four planes of PDTs. The B and C layers have three planes of PDTs. The drift resolution in the PDTs is 0.53 mm. Practical considerations such as support structures and readout electronics prevent full three-layer coverage of all η-ϕ space.

This work does not use muons except when the results from Run 1a are combined with this analysis. The Run 1a $W\gamma$ analysis only used muons found

in the pseudorapidity range $|\eta| < 1.7$. This restricted range of the pseudorapidity of muons was a result of the requirements of the DØ trigger system.

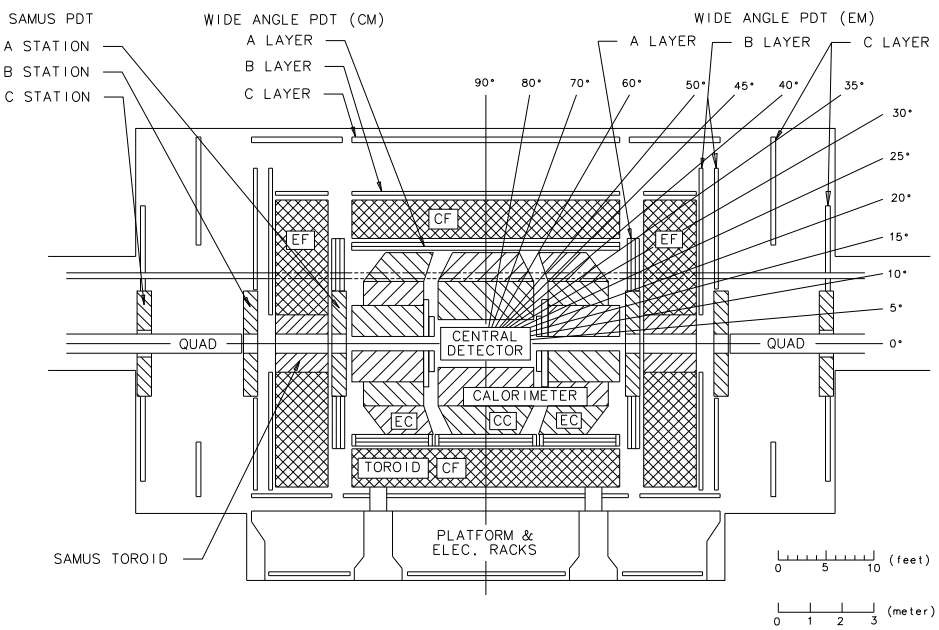

Figure 3.6. Side view of the DØ muon system.

3.6 Trigger and Data Acquisition

The DØ detector was designed to operate in a high-luminosity environment (average $\sim 5 \times 10^{30}\text{cm}^{-2}\text{s}^{-1}$ in Run 1a, average $\sim 7 \times 10^{30}\text{cm}^{-2}\text{s}^{-1}$ in Run 1b) at a large center of mass energy ($\sqrt{s} = 1.8$ TeV). The total cross section of elastic and inelastic $p\overline{p}$ interaction is approximately 70 mb (or 7×10^{-26}cm). The actual events of physics interest are only a tiny fraction of this sample. For example, QCD jet production is on the order of 5 mb, $p\overline{p} \to W + X$ is[5]

[5]Here, and elsewhere in this work "X" in an equation means "anything else". E.g. the X

is approximately 22 nb, $p\overline{p} \rightarrow Z + X$ is approximately 2 nb, $p\overline{p} \rightarrow W\gamma + X$ is approximately 110 pb, and $p\overline{p} \rightarrow t\overline{t} + X$ is approximately 6 pb. For events associated with a particular decay channel, the branching ratio for decays of the short-lived particles (W and Z bosons, $t\overline{t}$ pairs) further reduces these already tiny numbers. In order to extract these precious events from the huge background of primary elastic or minimum bias $p\overline{p}$ interactions the DØ detector uses a complex multilevel trigger.

The DØ trigger system has three levels of increasingly sophisticated event selection. The Level 0 scintillator-based trigger detects the occurance of an inelastic $p\overline{p}$ collision. The rate of data from Level 0 is on the order of 10^5 Hz. Level 1 is a collection of hardware triggers arranged in a flexible software-driven architechture which allows easy modification; the rate out of Level 1 is about 200 Hz. The Level 1 triggers operate within the 3.5 μsec time interval between beam crossings and contribute no deadtime. Additional rejection can be provided provided by a Level 1.5 trigger system which applies simple filtering algorithms. Candidates from Level 1 (and Level 1.5) are passed on the standard DØ data acquisition pathways to a farm of microprocessors which serve as event builders as well as the Level 2 trigger system. Sophisticated algorithms reside in the Level 2 processors which reduce the rate to about 2 Hz before passing them on to the host computers for recording and monitoring.

3.6.1 Level 0 Trigger and Luminosity Monitor

The Level 0 (L0) detector registers the presence of inelastic collisions and serves as the luminosity monitor for the experiment [42]. L0 consists of two

in $p\overline{p} \rightarrow W\gamma X$ means that a W boson and a photon are produced along with something else, possibly a jet or other energy from an underlying event.

scintillator hodoscopes. Each is mounted on the front surface of the opposing EC cryostat perpendicular to the beam direction. These hodoscopes have a checkerboard pattern of scintillators using 20 short (7×7 cm^2) elements and 8 long (7×65 cm^2) elements read out by two photomultipliers. The L0 trigger is $\approx 99\%$ efficient for non-diffractive inelastic collisions.

The L0 detector also provides information on the z-coordinate of the primary collision vertex by measuring the time difference on the signals in the two hodoscopes. The z-position is then used by Level 1 to measure transverse energies. The vertex position resolution is $\sigma_z \approx 3.5$ cm for single interaction events and $\sigma_z \approx 6.0$ cm for multiple interactions. A rough vertex position is measured within 0.8 μsec after an interaction (the 'fast vertex') and a more precise ('slow vertex') measurement is available within 2.1 μsec.

The Tevatron luminosity is obtained by measuring the rate for non-diffractive inelastic collisions. Events of this type are selected by requiring a Level 0 coincidence within $|z_{\mathrm{vtx}}| < 100$ cm. Scalers count various quantities: live crossings, coincidences satisfying the vertex cut, and coincidences satisfying the requirements of a single interaction[6]. These scalers allow the luminosity to be measured independently for each beam bunch and provide feedback to accelerator operations. The calibration of the luminosity monitor is based on the world average values of total, elastic, and single diffractive cross sections, using the results from CDF [43] and E710 [44]. DØ uses the average of 58.9 pb for inelastic and 9.5 pb for single diffractive cross sections [45]. The systematic error of the normalization constant is 5.4%.

[6]At L0, a multiple interaction is determined by timing the hits in the hodoscopes. At an instantaneous luminosity of $6 \times 10^{30}\mathrm{cm}^{-2}\mathrm{s}^{-1}$ there is approximately one interaction per bunch crossing.

3.6.2 Level 1 and Level 1.5 Triggers

The Level 1 (L1) trigger [46] framework has several inputs: L0 information, the L1 calorimeter trigger and the L1 muon trigger. The calorimeter trigger extends to $|\eta| < 3.2$ in trigger towers of 0.2×0.2 in η-ϕ space. These trigger towers are subdivided longitudinally into electromagnetic and hadronic trigger towers. The output of the calorimeter L1 is the transverse energy deposited in the these towers. The L1 muon trigger's output is the number of muon candidates and their p_T. This information is fed into the L1 trigger framework, which is based on the two-dimensional AND-OR network, which converts up to 256 inputs into a 32-bit word with the L1 trigger information. An event is said to pass L1 if at least one bit of the trigger word is set.

The L1 trigger also uses information about Main Ring activity. This information can be used to veto certain events either as part of the L1 system or as part of an offline analysis. Typically trigger events with the L1 terms MRBS_LOSS and MICROBLANK are rejected as they indicate periods of Main Ring activity. The MRBS_LOSS term indicates events taken during the period of Main Ring injection and transition; the MICROBLANK term indicates the passage of the Main Ring bunches through the DØ detector.

Some of the L1 bits were prescaled, meaning that only some fraction of the events which satisfy that L1 trigger bit are accepted for recording to tape. The prescales are different for different bits and can also depend on the luminosity. The use of prescales prevents large cross section processes, such as QCD multijet, from saturating the trigger system.

During Run 1b a Level 1.5 (L1.5) system [47] was implemented that uses

the L1 calorimeter trigger tower data and applies filtering algorithms based on neighbor sums and ratios of the EM and EM plus hadronic transverse energies. For the triggers of interest for this work, Level 1.5 allowed DØ to maintain unprescaled and lower trigger thresholds at L1 for electromagnetic objects. The time required to perform the Level 1.5 algorithms may take up to 250 μsec; for the triggers used in this analysis the data lost due to L1.5 is approximately 2%.

3.6.3 Level 2 Filter and Data Acquisition System

The Level 2 (L2) filter is a software based trigger system. The system is based on a farm of VAXstation 4000-60 and 4000-90's which collect and process the raw data. A coarse reconstruction of the event is performed and the event is checked against the various L2 bits which are fed from the L1 triggers. (Each L2 bit follows a particular L1 bit.) The L2 filter then rechecks if the requirements on the transverse energies of EM/hadronic objects, number and transverse momenta of muons, missing transverse energy, etc. are satisfied. If all the L2 requirements are satisfied, the event is said to pass L2 and it is temporarily stored on disk before being transferred to an 8 mm magnetic tape.

3.7 Offline Reconstruction

The amount of time available for event reconstruction at Level 2 is very small; full reconstruction must take place offline. A farm of Silicon Graphics processors has the dedicated task of converting the digitized raw data into hit position, hit timing, and deposited energy in the detector. These

are then corrected with calibrated data such as amplifier gains, geometrical surveys, etc. The software package that handles event reconstruction is named DØRECO [37]. The Run 1a data used in this analysis was processed with DØRECO version 11, while the Run 1b data was reconstructed using DØRECO version 12. Here are the major details of event reconstruction as they pertain to this analysis.

3.7.1 Vertex Reconstruction

Information from the central tracker is used to reconstruct the vertex position. First, fits are performed on the hits in the drift chambers to make tracks in the $r\phi$ plane. An rz track associated with each $r\phi$ track is reconstructed. The z vertex is obtained by projecting the reconstructed tracks onto the beam axis and performing a gaussian fit to the distribution of z intercepts. If more than one vertex is reconstructed, the vertex with the most tracks is designated as the primary vertex. In Run 1b the distribution of vertices was centered at $z = 0.0$ cm with an rms deviation of 29 cm.

3.7.2 Electron/Photon Reconstruction

The reconstruction of electrons and photons is straightforward. First, EM towers[7] are ordered according to their transverse energy (E_T), highest to lowest. To reduce noise response, the lowest possible E_T for a tower is chosen to be 50 MeV. The towers are then looped over, finding the nearest neighbor with the highest E_T. These two towers are then linked together, and in this way EM clusters are formed. The EM cluster is then designated as a possible

[7] An EM tower is a tower in the first four (EM) layers of the calorimeter and possibly the first layer of the fine hadronic calorimeter (FH1).

electron (sometimes referred to as a PELC) if a track is found in a *tracking road* of 0.1×0.1 in θ-ϕ space. If no track is found, the object is designated as a possible photon (sometimes referred to as a PPHO).

Energy resolution (σ) of electrons and photons, determined from EM clustering, is typically expressed in terms of the following equation:

$$\left(\frac{\sigma}{E}\right)^2 = C^2 + \frac{S^2}{E} + \frac{N^2}{E^2} \tag{3.1}$$

where E is the energy of the incident electron, C is a constant term involving calibration errors, S is sampling fluctation of the liquid argon calorimeter and N is the noise term. The values of C, S and N are shown in Table 3.7.

Table 3.7. Resolution parameters of the EM calorimeter

Calorimeter	C	S ($\sqrt{\text{GeV}}$)	N (GeV)
CCEM	0.003 ± 0.002	0.140 ± 0.005	0.14 ± 0.14
ECEM	0.003 ± 0.003	0.157 ± 0.006	0.29 ± 0.03

3.7.3 Muon Reconstruction

The first stage of muon reconstruction starts with the hit information based on the signals from the muon system. This data is corrected based on survey information and the hits are associated with 3–d space points. These hits are then grouped into tracks loosely consistent with muons from the interaction region. A global fit is then performed using the muon chamber track segments, energy deposited in the calorimeter, tracks in the central tracker, and the reconstructed vertex. The momentum resolution is parametrized as [48]

$$\frac{\sigma(1/p_\mu)}{(1/p_\mu)} = \sqrt{\left(\frac{0.18(p_\mu - 2)}{p_\mu}\right)^2 + ((0.003 \pm 0.001)\, p_\mu)^2}$$

where p_μ is measured in GeV/c.

3.7.4 Jet Reconstruction

The jet reconstruction algorithm starts by finding seed towers in the calorimeter with energy greater than 1 GeV. Energies from nearby towers, up to a given radius in η-ϕ space, are added to the seed towers. The reconstruction algorithm then decides whether or not to merge any clusters based on the amount of energy shared between two clusters. The jet reconstruction threshold is 8 GeV. The jet energy resolution follows the form of Equation 3.1, with the parameters in Table 3.8. In this work jets were reconstructed within a cone of radius 0.5 in η-ϕ space. The approximate resolution of electromagnetic and hadronic objects at a few different energies are listed in Table 3.9.

Table 3.8. Resolution parameters of the hadronic calorimeter

C	S ($\sqrt{\text{GeV}}$)	N (GeV)
0.010 ± 0.005	0.74 ± 0.07	2.16 ± 0.22

Table 3.9. Comparison of the different resolutions of electromagnetic and hadronic objects at different energies

Incident Energy	σ/E	
	e/γ	Jets
10 GeV	4.7 %	31.9 %
25 GeV	2.8 %	17.2 %
50 GeV	2.0 %	11.4 %

3.7.5 Reconstruction of Missing Transverse Energy ($\not{E}_T$)

The missing E_T of an event is defined as the negative of the energy vector sum of all the final states in the transverse plane, using energy measured in

the calorimeter. For technical reasons, $\not{E}_T$ is calculated including or excluding muon transverse energy if a muon candidate is present. In the analysis involving $W \to e\nu$, muon data are not used, so the $\not{E}_T$ measured by the calorimeter can be assigned to the transverse energy of the non–interacting particles (e.g. neutrinos). The $\not{E}_T$ resolution of the detector is parametrized [49] as

$$\sigma = a + b \times S_T + c \times S_T^2 \tag{3.2}$$

where S_T is the sum of the scalar transverse energy in the calorimeter. The values of the parameters are in Table 3.10.

Table 3.10. Missing E_T resolution parameters

a	b (GeV)	c (GeV^{-1})
1.89 ± 0.05	$(6.7 \pm 0.7) \times 10^{-3}$	$(9.9 \pm 2.1) \times 10^{-6}$

For the missing E_T , σ/S_T improves from 20% at 10 GeV to about 5% for 50 GeV.

3.8 Monte Carlo

In the next chapter, an analysis of data which compares the observed $W\gamma$ signal with the standard model and non-standard models where anomalous couplings are allowed to vary will be presented. The model predictions depend on precise Monte Carlo calculations. A Monte Carlo event generator must properly include the production, trilinear and decay diagrams to calculate the total and differential cross sections of $p\overline{p} \to \ell\nu_\ell\gamma$ for both standard model and anomalous cases. It must also be able to generate a large number of events quickly. This is important because the anomalous effects are most pronounced

at high p_T^γ where the SM cross section is small, requiring the generation of a large number of events to obtain an accurate p_T^γ spectrum. Similar large event samples also need to be generated for a variety of coupling parameters in order to set limits on the anomalous couplings. Finally, any Monte Carlo which is to be used must have the ability to simulate the response of different parts of the DØ detector, e.g. geometrical acceptances, triggers, particle identifiaction.

The event generator used for the DØ $W\gamma$ analyses is that of U. Baur and D. Zeppenfeld [16]. This generator is referred to as BAUR. The BAUR Monte Carlo simulates leading order production and decay kinematics for both the electron and muon decay modes of the W boson. Higher order QCD effects such as $p\overline{p} \rightarrow q + W + \gamma$ are taken into account by increasing the cross section output of the BAUR generator by a K–factor of 1.34.

Two options exist for applying the various instrumental effects to the BAUR Monte Carlo. The first option is to use the output of BAUR (the 4-momenta of the final state particles) as an input for a complete detector simulation program such as DØGEANT [50]. Underlying event effects can be added to the BAUR output through the ISAJET [51] event generator prior to DØGEANT. In practice this approach is very time-consuming and not practical considering the size of κ-λ space which needs to be studied in the process of setting limits on the anomalous couplings. A more practical approach is to modify the original BAUR generator to include a fast Monte Carlo simulation of the DØ detector. This is what was done; the modified BAUR code is referred to as DØBAUR.

The fast (or *toy*) Monte Carlo includes the instrumental resolution of the detector, the E_T-dependence of the trigger system, and particle identification efficiencies among the many factors used in the detector simulation. Whenever

possible these efficiencies are studied using data collected in the same run which implicitly takes the effect of multiple interactions, underlying event, etc. into account. The following effects were all included in DØBAUR:

- Geometrical acceptance of the DØ detector.
- Primary vertex longitudinal position displacement (Run 1a: $z_{\rm vtx} = -11.0$cm, Run 1b: $z_{\rm vtx} = 0.0$ cm) and smearing ($\sigma_z = 29.0$ cm).
- Smearing of electron/photon and muon momenta as well as the missing transverse energy according to the resolutions, as described in Section 3.7.
- Level 1 and 2 trigger efficiencies and turn-on effects, as described in Section 4.1.
- Photon, electron and muon identification efficiencies, as described in Sections 4.2.1 and 4.2.2.
- Photon losses due to conversions in the material in front of the calorimeter and random track overlap.
- Transverse kick of the $W\gamma$ system due to associated jet production, which is generated according to the observed W boson p_T distribution (q.v. Figure 4.4).

The various effects can be switched on or off in the toy Monte Carlo for easy study. The standard output of DØBAUR is a total cross section for a given set of cuts as well as a set of histograms of different kinematical distributions, including the p_T spectrum of the photon. These outputs are vital for the precision measurement of anomalous couplings, but they are not without

systematic uncertainties. There is a systematic uncertainty in the DØBAUR code which is due to both detector and theoretical effects. These uncertainties affect the final measurement of the anomalous couplings; they are summarized in Table 5.4 for both the electron (Runs 1a and 1b) and muon (Run 1a only) channels.

The detector related uncertainties will be described later. The dominant portion of the theoretical uncertainty is due to the many possible choices for the structure functions. The MRSD-' [52] set of next-to-leading order (NLO) structure functions is chosen because they describe the measurement of the W boson decay asymmetry [53] better that other sets of structure functions. Twenty one different NLO and leading order (LO) structure functions [54] were used to to calculate the Standard Model cross section for W boson decays to both electrons and muons. See Figure 3.7. The LO structure functions result in a systematically lower cross section when compared to the NLO structure functions. The BAUR Monte Carlo calculations only include LO matrix elements but approximates NLO QCD corrections by use of the K–factor, so a NLO structure function choice is more appropriate. The uncertainty[8] in the cross section due to our choice of the MRSD-' set is 6%.

A smaller theoretical uncertainty is the scale used for the structure function calculations. This uncertainty was estimated to be 1% by varying the nominal value of $Q^2 = \hat{s}$ from $\hat{s}/2$ to $2\hat{s}$. The effect of the p_T kick to the $W\gamma$ system was also studied in the BAUR code and found to introduce and additional uncertainty of 4.9% on the cross section for the Run 1b analysis.

[8]The uncertainty of 6% reflects the uncertainty between the different groups of structure functions (CTEQ, MRS, etc.) not the uncertainty between different flavors of any one group's particular parton distribution functions, e.g. MRSD-' and MRSH.

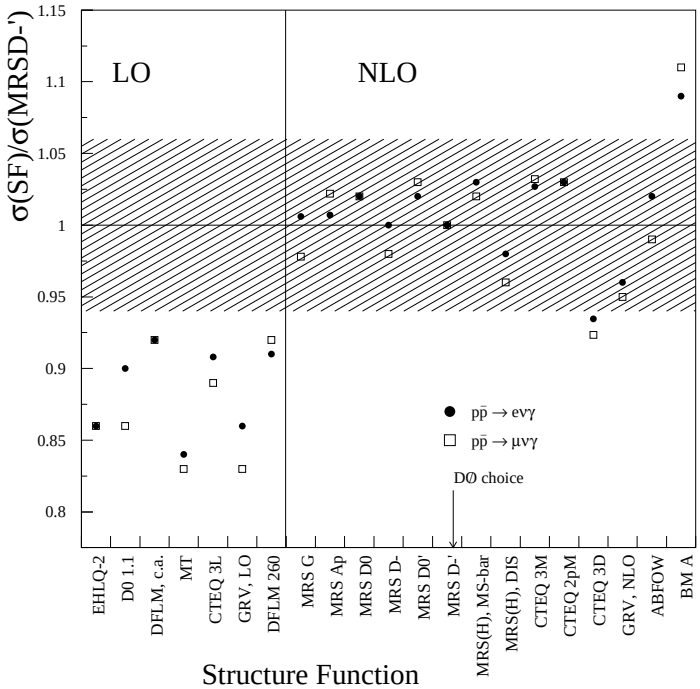

Figure 3.7. SM $W\gamma$ cross sections for different structure functions, normalized to the MRSD-' set. The band shows the 6% systematic uncertainty. The cross sections from leading order functions are shown for comparison.

CHAPTER 4

EVENT SELECTION

This chapter contains a detailed description of the selection process for $e\nu\gamma$ events from the DØ Run 1b data. The triggers that were used were studied and are parametrized. The efficiencies of the offline selection requirements are presented. Detector inefficiencies are also shown. Characteristic plots of the $W \rightarrow e\nu$ sample and the $e\nu\gamma$ candidates are shown, along with estimates of backgrounds. Finally the cross section for $p\overline{p} \rightarrow W\gamma$ will be calculated and compared to the Standard Model prediction.

4.1 Trigger Efficiencies

This $W\gamma$ analysis can be considered a subset of the Run 1b $W \rightarrow e\nu$ analysis, with the only difference between the two analyses being the requirement of a photon in the former study[1]. Each analysis corresponds to a luminosity of 73.0 ± 3.9 pb^{-1} of data from the same L2 filter, EM1_EISTRKCC_MS.

EM1_EISTRKCC_MS is fed by the L1 single electron trigger EM_1_HIGH. This trigger required that a single EM object with E_T above 12 GeV be found in the EM calorimeter. This threshold was lowered to 10 GeV when the L1.5

[1]Of course, some details of the two analyses may differ, e.g. offline electron identification requirements, kinematic or fiducial requirements, etc.

system became operational. For $W \rightarrow e\nu$ decays the Jacobian peak in the E_T distributions of electrons is around 40 GeV. With such a low L1 threshold, the efficiency for the $W \rightarrow e\nu$ trigger is high, almost 99%.

For most of Run 1b, this trigger had an active veto that passed events during either the MRBS_LOSS or MICROBLANK periods (q.v. Section 3.6.2) but did not pass events in which these two periods overlapped. Data taken during each of these periods contains Main Ring energy deposited in the calorimeter, which seriously degrades missing E_T measurement. In subsequent $W \rightarrow e\nu$ analyses these contaminated data are rejected as an offline cut. It was hoped that very detailed studies of the Main Ring energy would allow DØ to recover this extra data, but the prospects for this are not good [55].

The L2 filter EM1_EISTRKCC_MS required that there be missing E_T greater than 15 GeV and at least one EM object above 20 GeV. The EM object was also required to pass a simple shape cut and the energy of the cluster was required to be somewhat isolated. Because of the higher thresholds, the L2 filter demonstrates a typical turn-on curve as a function of E_T for both the missing E_T and the E_T of the EM object. The two components of EM1_EISTRKCC_MS were considered separately.

To parametrize the turn-on of the missing E_T part of EM1_EISTRKCC_MS the diagnostic filter EM1_ELE_MON was used. Both filters hang from the same L1 term. EM1_ELE_MON has the same electromagnetic L2 threshold, but requires looser shape cuts on the EM cluster and has no $\not\!\!E_T$ requirement. Starting with events that pass EM1_ELE_MON, the L2 shape cuts of EM1_EISTRKCC_MS are imposed offline. From this sample it is then seen how many also pass the L2 $\not\!\!E_T$ requirement of EM1_EISTRKCC_MS. The curve is fit to an error function of the following form:

$$f(E_T) = p_4 \left(\frac{1 - p_3}{2} (1 + \mathrm{erf}(p_1 (E_T - p_2))) + p_3 \right)$$

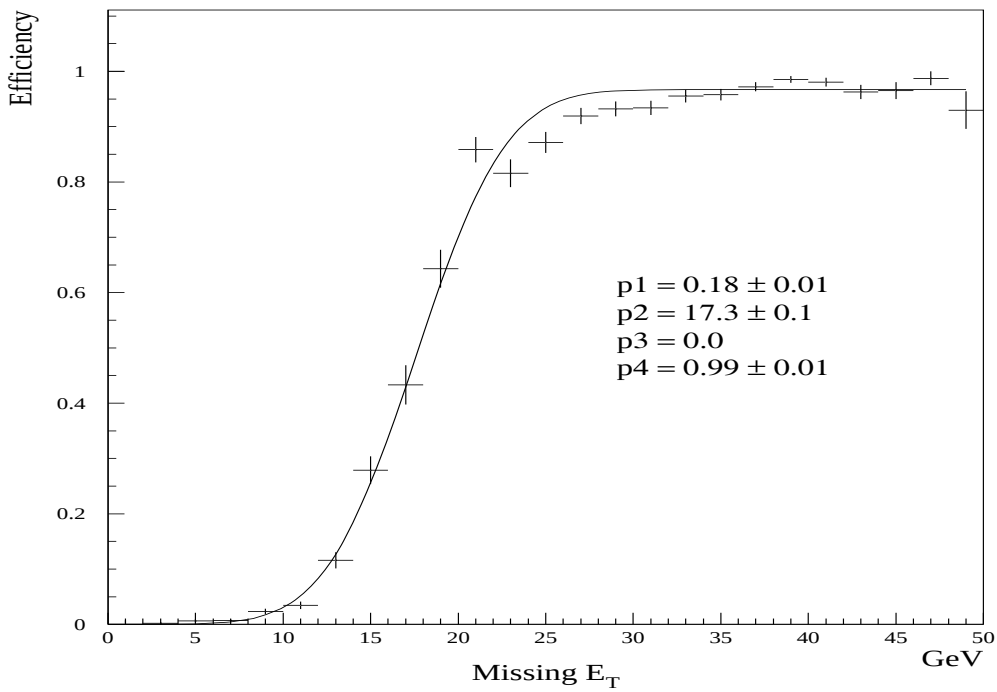

Figure 4.1. The turn-on curve for the $\not\!\!E_T$ part of EM1_EISTRKCC_MS. Binomial errors are shown on each point.

The electromagnetic part of EM1_EISTRKCC_MS is studied by starting with a sample of events with two EM clusters with reconstructed $E_T > 10$ GeV found in one of two monitor filters, ELETRK_1_MON or ELE_1_MON. Each of these two filters required a single electron with E_T at L2 above 16 GeV. Both electrons in these events are checked to see if they passed the requirements of the L2 filter. If only one passed the second electron is entered into an unbiased sample; if both pass, each is entered into the sample. The unbiased electrons are required to pass the shape cuts of EM1_EISTRKCC_MS and then a cut on L2 E_T above 20 GeV is made to generate a turn-on curve versus

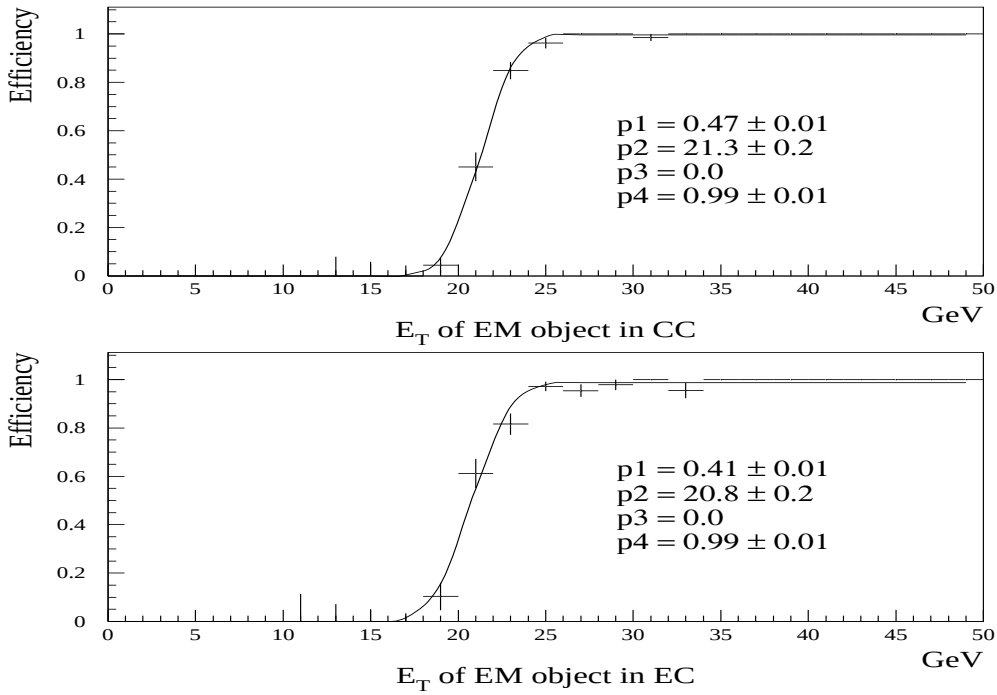

Figure 4.2. The turn-on curves for the electromagnetic E_T part of EM1_EISTRKCC_MS, for EM objects in each calorimeter. Binomial errors are shown on each point.

reconstructed E_T of the electromagnetic object. Separate turn-on curves are generated for both the central and endcap calorimeters. These curves and the fit parameters are shown in Figure 4.2. These parameterizations of the trigger efficiencies were included in the DØBAUR code.

4.2 Particle Identification

Once an event has made it through the trigger system and the various particles have been reconstructed (see Section 3.7) it is necessary to apply a set of offline cuts to the various objects to reduce backgrounds that might otherwise wash out the signal of interest. The first set of requirements for an event to make it into the $W \rightarrow e\nu$ sample is that there be only one electron

in the event with an E_T above 25 GeV. This electron must be in the fiducial volume corresponding to the coverage provided by the DØ EM calorimeter: $|\eta_e| < 1.1$ for CC electrons, $1.5 < |\eta_e| < 2.5$ for EC electrons. There must also be at least 25 GeV of missing E_T in the event. Using the electron E_T and the $\not\!\!E_T$, the *transverse mass* of the W boson is reconstructed and required to be above 40 GeV/c^2. The transverse mass of the $e\nu$ system is defined as

$$M_T = \sqrt{2E_T^e \not\!\!E_T (1 - \cos\phi^{e\nu})}$$

where $\phi^{e\nu}$ is the azimuthal angle between the electron and the missing E_T. The E_T and M_T requirements are referred to as *kinematic* cuts. The pseudorapidity requirement is a *fiducial* cut.

DØ has a menu of different *quality* (or ID) cuts that can be applied to the various reconstructed particles. It is generally the case that different analyses will use a common set of quality cuts but impose very different values for any given cut[2]. Deciding where to set a given cut depends very much on the type of signal that is trying to be extracted. While studying rare events such as $W\gamma$, it is important not to use quality cuts which are too tight. To do so runs the risk of eliminating valuable candidates. For this reason, the quality cuts imposed on the electron from W decays are somewhat looser than those imposed in a straightforward $\sigma(p\overline{p} \to W) \times$ BR$(W \to e\nu)$ cross section measurement. This is perfectly reasonable since a $W\gamma$ analysis uses the presence of a photon as a very efficient cut! In fact, in this measurement, it is the quality cuts on the photon which turn out to be the most important.

[2]E.g., compare the use of Isolation (I) between the electron and photon ID below.

4.2.1 *Electron Identification*

There are two subsets of quality cuts that can be used on reconstructed electrons. The first set of cuts comes from the information about the electromagnetic shower in the EM calorimeter. The second set of cuts comes from the information associated with an electron's track through the central detector.

The quality information available from the calorimeter includes:

- The amount of EM and hadronic energy of a given cluster, and
- The transverse and longitudinal shape of a given cluster.

All of the electrons in this analysis are required to have at least 90% of their total energy to be in the EM calorimeter. This is refered to as a cut on *EM fraction*. These electrons are also required to have a good *Isolation*, which is defined as

$$I = (E_{\rm tot}(0.4) - E_{\rm EM}(0.2))/E_{\rm EM}(0.2)$$

where $E_{\rm tot}(0.4)$ is the total calorimeter energy inside a cone of radius $R = 0.4$, and $E_{\rm EM}(0.2)$ is the EM energy inside a cone of 0.2 in the same units. The Isolation requirement of electrons in this analysis is $I < 0.15$.

The last quality cut made on electrons is based on the shower profile of the EM cluster. This is done using a covariance technique called the *H–matrix* algorithm [56]. The algorithm analyzes the observed energy depositions in different cells of the electron cluster and compares them with electrons from a Monte Carlo sample. It does this by using a 41×41 covariance matrix built from the Monte Carlo electrons. The inverse of the covariance matrix is called the H–matrix. A χ^2-like function is then calculated on a cluster-by-cluster basis using the H–matrix as an error matrix. This χ^2-like function is

a quantitative measure of the probability that the cluster is due to a single electron or photon. Test beam data [57] of both electrons and pions was used to determine the optimum cuts on the H–matrix χ^2 for electron identification. The χ^2 was required to be less than 100 for CC electrons and less than 200 for EC electrons. The cut is looser for EC electrons because of the different amount of material in front of the different calorimeters which results in different multiple scattering and conversion probabilities for electrons and photons hitting the CC and EC. The various calorimeter based quality cuts are very correlated and the total efficiency reflects this.

The quality information available from the central tracker includes:

- Quality of the track associated with the EM cluster.
- Ionization (dE/dx) along a track.
- Energy deposited in the TRD.

For this analysis, only the accuracy of the track fit is used. Tracks are more likely to accurately point to the center of an EM cluster if they have a low *track match significance* (σ_T). The track match significance is defined as

$$\sigma_T = \sqrt{\left(\frac{r\Delta\phi}{r\delta\phi}\right)^2 + \left(\frac{\Delta z}{\delta z}\right)^2}$$

where r is the distance from the vertex to the EM shower, $\Delta\phi$ and Δz are the differences in azimuthal angle and beam direction between the track position and the shower center. $r\delta\phi$ and δz are the position resolutions of the calorimeter. For the $W\gamma$ analysis, σ_T is required to be less than 10 for both CC and EC electrons.

Besides rejecting real electrons that fail these quality cuts, there is a source of electron finding inefficiency that has not yet been taken into account. All

electrons were required to have a reconstructed track somewhere in the tracking road from the cluster to the vertex in order to enter the $W \rightarrow e\nu$ sample. Because of the finite efficiency of the central tracking chambers and inefficiencies in the reconstruction code, some true electrons will not have their tracks detected or reconstructed. This implicit requirement has an efficiency associated with it referred to as the *track-in-road* efficiency.

The efficiency of all these cuts was studied using electrons in the $Z \rightarrow ee$ event sample from Run 1b[3]. An unbiased sample of electrons was found in this sample by using events where one electron passed tight quality cuts. The second electron is then unbiased. If both electrons pass the tight cuts, both enter the unbiased sample. The efficiency for a given set of quality cuts on a true electron is estimated by removing the effect of background in the $Z \rightarrow ee$ sample. The true efficiency (ε) for a set of cuts is given by

$$\varepsilon = \frac{\varepsilon_s - \varepsilon_b f_b}{1 - f_b} \tag{4.1}$$

where ε_s is the efficiency measured in the signal region, ε_b is efficiency measured in the background region, and f_b is the ratio of the number of background events in the signal region to the total number of events in the signal region. The signal region for $Z \rightarrow ee$ was chosen to be the region of the Z invariant mass (m_Z) spectrum between 86 GeV/c^2 and 96 GeV/c^2. The background under the Z peak was estimated by using a sidebands technique. The number of events in the sidebands 61 GeV/c^2 $< m_Z <$ 71 GeV/c^2 and 111 GeV/c^2 $< m_Z <$ 121 GeV/c^2 was averaged to estimate f_b. Systematic uncertainties for this method were estimated by comparisons with the more complicated method of fitting the m_Z spectrum to a relativistic Breit-Wigner function

[3]The reasons for using collider data from the same run to estimate efficiences were given in Section 3.8.

convoluted with a Gaussian added to a linear background. The two different methods have good agreement [58].

The track-in-road efficiency is estimated in a similar manner, except that the $Z \rightarrow ee$ sample used for that measurement is allowed to include photons (i.e. possible electrons with a lost track) as the unbiased electron. The track-in-road requirement is then tested on this sample with the backgrounds taken into account as in Equation 4.1. The electron quality cuts and their efficiencies are summarized in Table 4.2.1.

Table 4.1. Definitions and efficiencies (ε) for the electron identification cuts in the central and endcap calorimeters

Cut description	CC		EC	
	Cutoff	ε	Cutoff	ε
H-matrix χ^2	< 100	0.949 ± 0.003	< 200	0.947 ± 0.005
EM fraction	> 0.90	0.995 ± 0.005	> 0.90	0.995 ± 0.005
Isolation	< 0.15	0.993 ± 0.002	< 0.15	0.996 ± 0.002
Track match	$< 10\sigma$	0.980 ± 0.002	$< 10\sigma$	0.937 ± 0.006
Track-in-road		0.831 ± 0.005		0.856 ± 0.008
All cuts		0.768 ± 0.006		0.760 ± 0.011

4.2.2 Photon Identification

In this analysis, a photon is required to have transverse energy above 10 GeV, and it is required to be well separated from the electron in η-ϕ space: $\Delta R_{e\gamma} > 0.7$. Photons are detected at DØ in the same manner as electrons: through electromagnetic showers in the calorimeter. The electromagnetic showers of electrons and photons are practically identical, so the same calorimeter based quality cuts are used. Photons in this study have the same EM fraction and H–matrix χ^2 requirements as the electrons. The Iso-

lation for photons is tighter, $I = 0.10$, to reduce the QCD background (see Section 4.5.1). The efficiency of these calorimeter based cuts is estimated using Z events as described in Section 4.2.1. The quality cuts and their efficencies are summarized in Table 4.2.2.

Table 4.2. Definitions and efficiencies (ε) for the photon identification cuts in the central and endcap calorimeters

Cut description	CC		EC	
	Cutoff	ε	Cutoff	ε
H-matrix χ^2	< 100	0.949 ± 0.003	< 200	0.947 ± 0.005
EM fraction	> 0.90	0.995 ± 0.005	> 0.90	0.995 ± 0.005
Isolation	< 0.10	0.968 ± 0.003	< 0.10	0.974 ± 0.004
All cuts		0.921 ± 0.004		0.923 ± 0.006

There is one major difference between the electron and photon efficiencies that is not yet taken into account. The efficiencies quoted in Table 4.2.2 are only true for photons with E_T above 23 GeV. For lower transverse energies, the Isolation and the H–matrix cuts are less efficient. The H–matrix cut is not as efficient at low transverse energies because it was tuned using electrons with E_T above 25 GeV. The Isolation requirement suffers at low E_T because of the underlying event and other noise in the detector which can be a significant portion of a 10 GeV cluster but not a 25 GeV cluster. No high-statistcis, low-background source of low-energy electrons or photons exists in the data, so photons generated with a Monte Carlo were overlaid with minimum bias data taken during Run 1b [59]. The minimum bias data were taken at a variety of instantaneous luminosities so the effect of different luminosities could be correctly incorporated into DØBAUR. The E_T-dependent decrease in photon identification efficiency for photons with E_T btween 10 and 23 GeV was

modeled using a function of the form:

$$\varepsilon(E_T) = A + B \times E_T + C \times E_T^2 \tag{4.2}$$

The parameters A, B, and C are given in Table 4.3. Equation 4.2 is multiplied by the plateau values given by Table 4.2.2. The curves are shown in Figure 4.3. It is important to note that even though there is a loss of efficiency for detecting low E_T photons, the efficiency for detecting photons with E_T above 23 GeV is still quite high. Recall that anomalous $WW\gamma$ couplings manifest themselves strongest at the high end of the p_T^γ spectrum, which is exactly where the DØ detector does best!

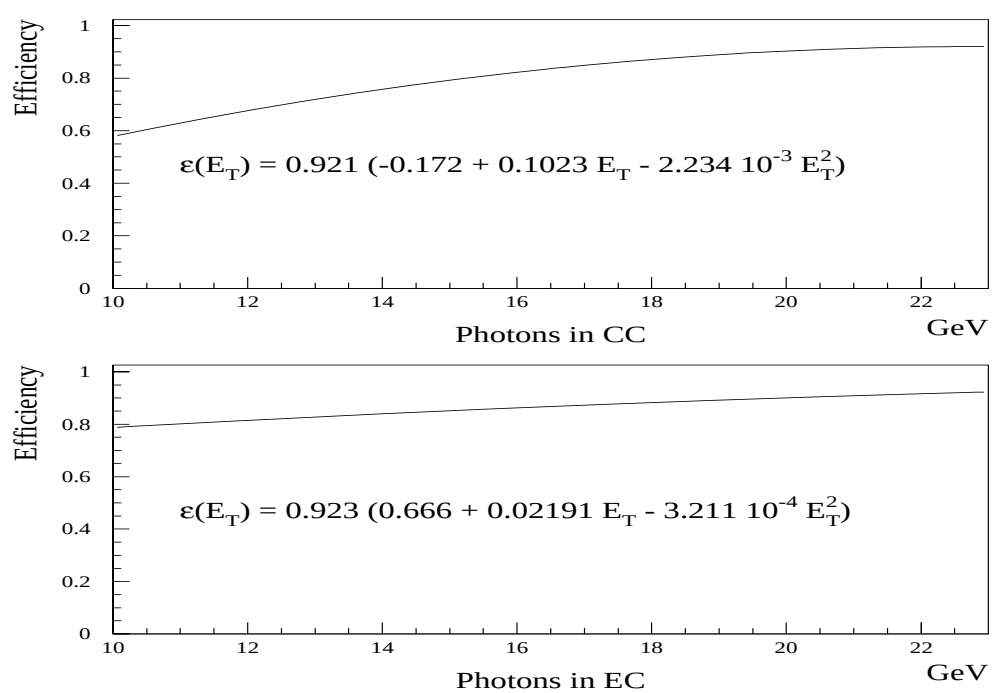

Figure 4.3. The efficiency of the photon ID cuts for photons with E_T below 23.0 GeV. Central photons have a lower efficiency due to the isolation requirement. The efficiency of the hits–in–road cuts is not included here.

Photons at DØ have no associated track, so tracking quality cuts such as

Table 4.3. Parameters for low E_T photon efficiencies

A	B (GeV^{-1})	C (GeV^{-2})
-0.1720	0.1023	-2.234×10^{-3}
0.6660	0.0219	-3.211×10^{-4}

were used on the electrons have no meaning, yet it is possible to use other information in the CDC and FDC to further improve the $W\gamma$ signal. The dominant sources of backgrounds to real photons in this analysis tend to leave hits in the drift chambers because they are either electrons which fail to have their tracks reconstructed, or because they are neutral mesons (π^0,η) which decay into two photons and one of the photons converts[4]. An analysis package was developed to check very tight roads[5] pointing from EM calorimeter clusters towards the event vertex, and counting the number of hits in the road.

A *clean* photon passes the following cuts:

Clean photons passing through CDC have: Ratio of hit wires ≤ 0.6,
# of XY hits ≤ 20,
# of 3d hits ≤ 1, and
# of z-segment hits $= 0$.

Clean photons passing through FDC have: Ratio of hit wires ≤ 0.7, and
# of XY hits ≤ 36.

The efficiency of this *hits-in-road* cut was measured by using "emulated photons". Starting with the $Z \rightarrow ee$ sample, the calorimeter cluster positions

[4]Usually it is the case that the neutral mesons are produced along with many other mesons, some electrically charged, in a jet. These charged mesons will leave tracks just as electrons do, with the same track-in-road efficiency as true electrons.

[5]0.005×0.012 in θ-ϕ space, tracking roads use 0.1×0.1.

of the electrons were rotated in ϕ by $\pi/2$ and a new, tight road was constructed between this emulated photon and the vertex. This mimics the situation of real photons quite well. This method also has the advantage of implicitly taking effects such as instantaneous luminosity and multiple interactions into account. These cuts reject eleven electrons for every one which is accepted for both the central and forward regions, with an efficiency of $0.83 \pm .01$ (0.70 ± 0.03) in the CDC (FDC).

The hits-in-road cuts are very efficient at rejecting electrons with a lost track. This was studied by looking at low $\not{E}_T$ $Z \rightarrow ee$ events where one EM cluster was a PELC and the other was a PPHO. After backgrounds are taken into account, only $(11 \pm 2)\%$ of PPHO's are not rejected in both the CC and EC.

There are two other ways to lose photons at DØ that need to be modeled in the DØBAUR detector simulation. The first is the possibility of a *random track overlap*. Again, this was estimated by using rotated clusters in the $Z \rightarrow ee$ data[6]. The Run 1b probability for a random track to overlap a photon was found to be 0.139 ± 0.005 in the CC, and 0.161 ± 0.008 in the EC [59].

The second loss of photons is from photons being reconstructed as electrons because of conversions in the material in front of the CDC or FDC. The conversion probability (P_c) was calculated [60] using the DØGEANT [50] detector simulator. P_c is a function of the photon's pseudorapidity. P_c is then multiplied by the track-in-road efficiency to get the η-dependent probability of photon losses due to conversions. The conversion probability is roughly 10% (30%) for photons in the CC (EC).

[6]Here the larger 0.1×0.1 tracking cones were used to look for random tracks that point to the rotated clusters.

4.3 $W \rightarrow e\nu$ Sample

After imposing the various kinematic, fiducial and electron ID cuts on the data, over sixty-thousand $W \rightarrow e\nu$ candidates remain. Some of the characteristic plots for this sample are shown in Figure 4.4.

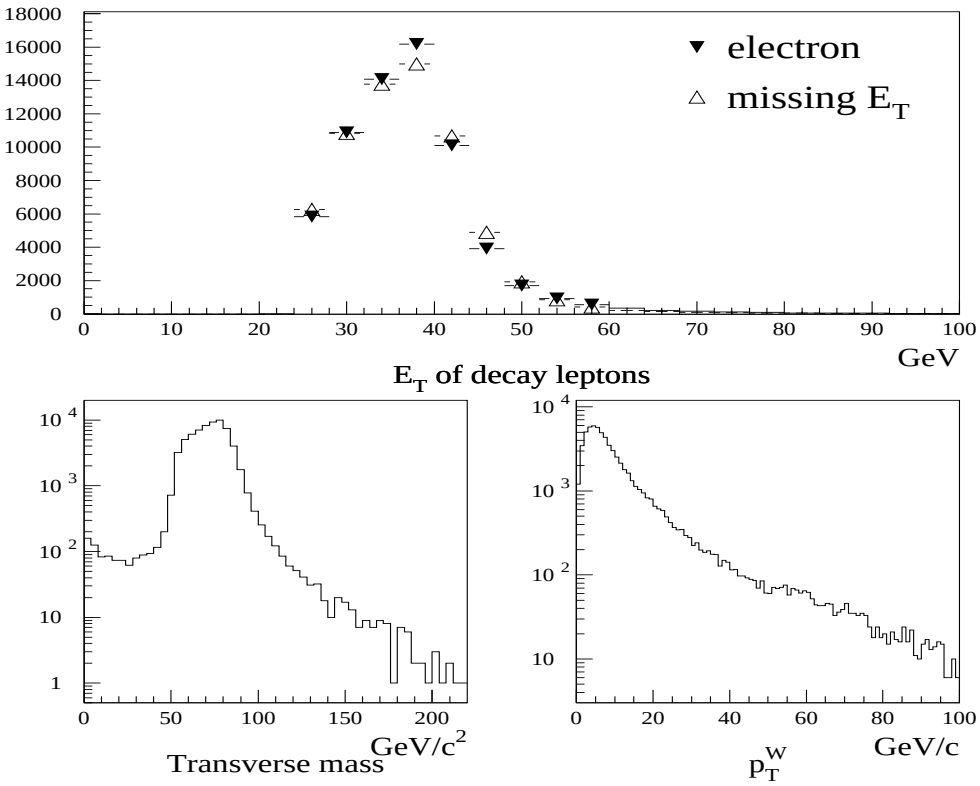

Figure 4.4. Characteristic spectra for the Run 1b $W \rightarrow e\nu$ events.

Figure 4.4 shows the E_T distribution of both the electrons and neutrinos (characterized by the missing E_T) in the parent $W \rightarrow e\nu$ sample. Notice that these distributions peak well above the trigger and event selection thresholds. The two–body transverse mass also peaks above the $e\nu\gamma$ selection threshold of 40 GeV/c^2. The p_T spectrum of the W candidates was used to estimate part of the theoretical uncertainties of the Monte Carlo generator, as described in

Section 3.8.

4.4 $W(e\nu)\gamma$ candidates

After requiring that the W candidates have a well-separated photon ($\Delta R_{e\gamma} > 0.7$) above 10 GeV that pass all of the photon ID cuts, forty-six $e\nu\gamma$ candidates remain. The highest observed p_T^γ is that of a 48.0 GeV/c photon in the central calorimeter. Thirty-nine of the events are $W\gamma + 0$ jet events, five are $W\gamma + 1$ jet events, and two are $W\gamma + 2$ jet events[7]. No events with two photons are observed.

Thirty-four of the events have central electrons, while thirty-three of the photons are in the central calorimeter. The fraction of central electrons, $(74 \pm 6)\%$, should be compared with the predicted Standard Model value of 73%, and $(72 \pm 7)\%$ central photons should be compared with the predicted Standard Model value of 71%.

The characteristic distributions of the candidates are shown in Figure 4.5. Also shown on those plots is the Standard Model expectation plus the background, as described in Section 4.5 . The three-body transverse mass plot will be of particular interest later. The three-body transverse mass of the $e\nu\gamma$ system is defined by

$$M_T(\gamma e;\nu) = \sqrt{(((m_{\gamma e}^2 + |\mathbf{E}_T^\gamma + \mathbf{E}_T^e|^2)^{\frac{1}{2}} + \not{E}_T)^2 - |\mathbf{E}_T^\gamma + \mathbf{E}_T^e + \not{\mathbf{E}}_T|^2)}$$

There are twenty-five candidates with $M_T(\gamma e;\nu) > 90$ GeV/c^2. These events are dominated by the ISR and direct $WW\gamma$ coupling diagrams (Figure 2.1, diagrams a,b,c), and so they have greater sensitivity to anomalies in

[7]For the case of counting jets in $W\gamma$ events, jets are reconstructed with a cone size of $R = 0.5$ and have a minimum E_T of 15 GeV. The allowed fiducial volume for the jets is $|\eta| < 4.5$.

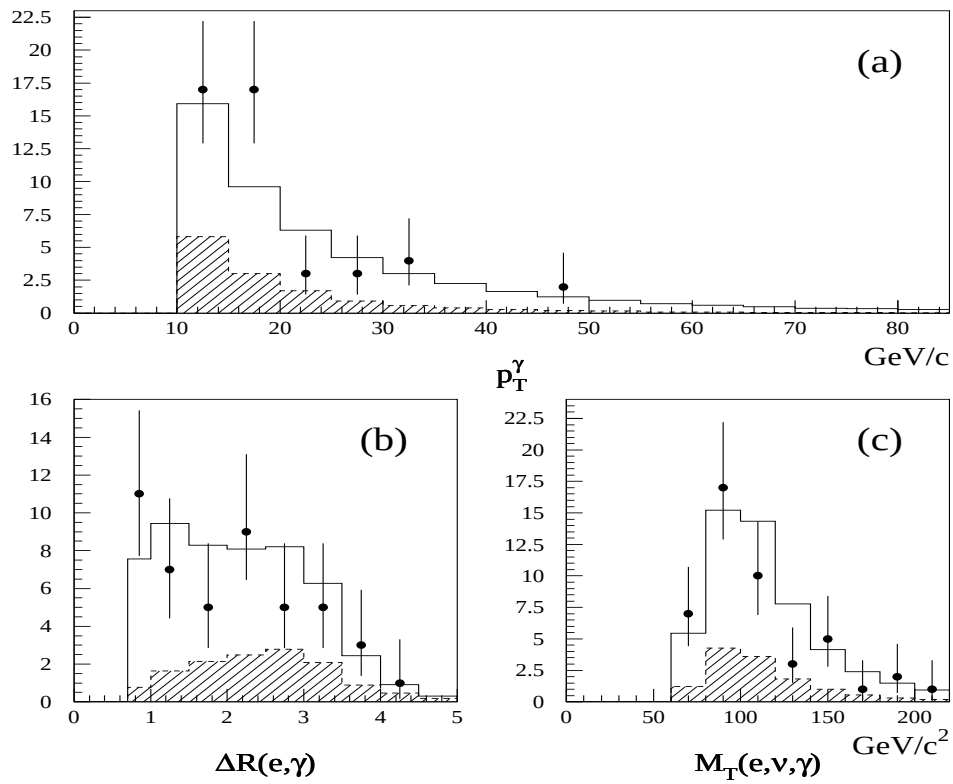

Figure 4.5. (a) The p_T^γ spectrum for the 46 Run 1b $W(e\nu)\gamma$ candidates. The $\Delta R_{e\gamma}$ and $M_T(\gamma e;\nu)$ distributions (b,c) are also shown. The points are the data with 1σ error bars. The solid histograms are the Standard Model Monte Carlo predictions plus the background estimates (shown as shaded histograms).

the $WW\gamma$ vertex.

4.5 Backgrounds to $W(e\nu)\gamma$

4.5.1 QCD Background

The dominant background to the process $p\overline{p} \to W(e\nu)\gamma$ arises from W + jet events where the jet decays electromagnetically and is reconstructed in the calorimeter as a photon. The probability for a jet to fluctuate into a well-isolated electromagnetic shower is small, but the large number of jets above

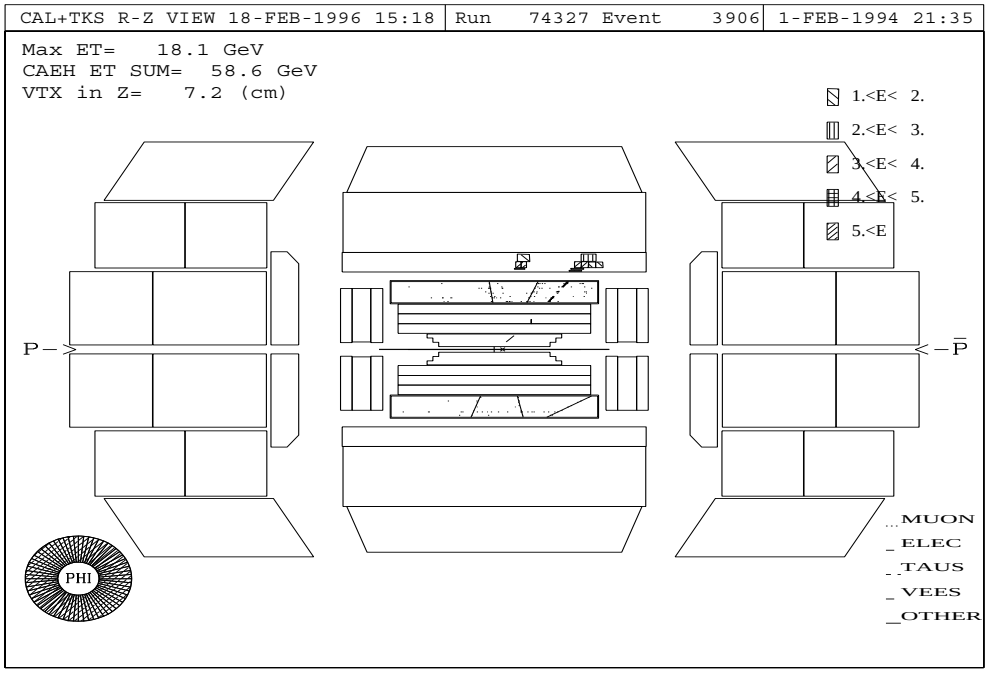

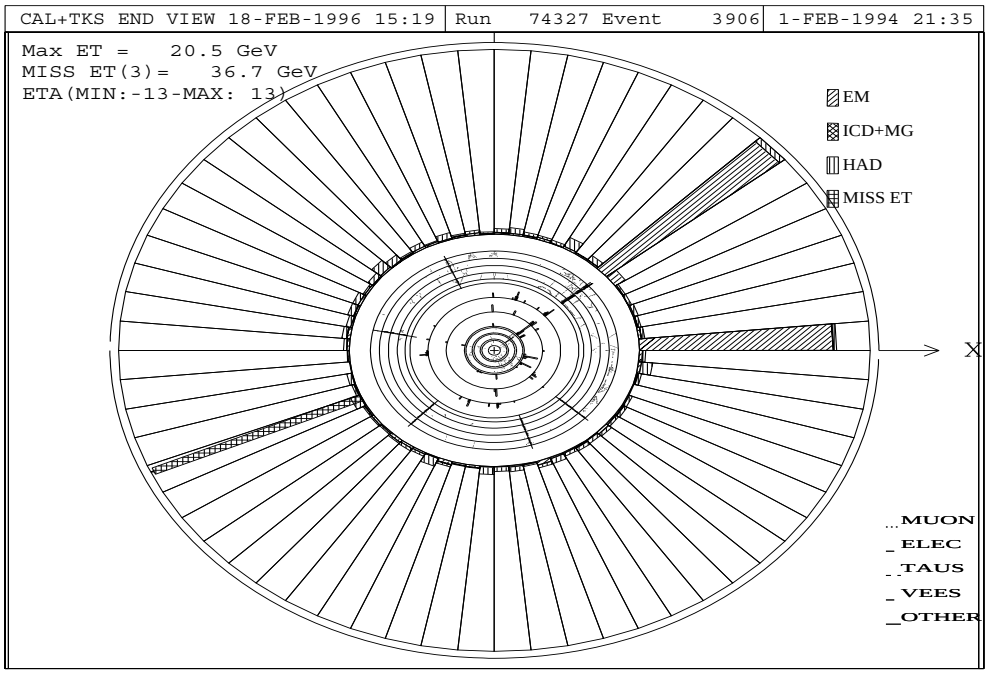

Figure 4.6. Two event displays for the first $W(e\nu)\gamma$ candidate found in Run 1b at DØ. The top display shows the rz (side) view of the DØ detector. The development of the electromagnetic showers in the central calorimeter can be seen. The relative amounts of transverse energy and $\not\!\!E_T$ in the central calorimeter is shown in the bottom display.

10 GeV in the W sample (over 19000 in Run 1b) guarantees that some jets will look identical to photons.

The probability for a jet to mimic a photon is refered to as the *fake rate*. The fake rate is measured directly from the data by building large samples of multi-jet events from triggers dedicated to QCD physics. Hadronic jets have a slower trigger turn-on than the electromagnetic jets, so the leading (trigger) jets are eliminated from the multi-jet sample. The total $\not\!\!E_T$ is required to be less than 15 GeV, insuring that there is no contamination from $W \to e\nu$ events. Approximately two million jets are left in the multi-jet sample used in this work. There are two sources of photons in the sample, fake photons and direct photons from initial state radiation in QCD events. The photons are required to pass all of the identification cuts described in Section 4.2.2 and their E_T spectrum is plotted. The observed E_T spectrum for the photons in each calorimeter (CC/EC) is then divided by the E_T spectrum for the jets, and the E_T-dependence of Prob(jet $\to \gamma$) is checked. There is no observed E_T-dependence for photons in this sample, so constant values are used. The fake rates are tabulated in Table 4.4.

Table 4.4. E_T-independent values of Prob(jet $\to \gamma$), by calorimeter

Calorimeter	**Prob(jet $\to \gamma$)**
Central	$(8.7 \pm 0.3) \times 10^{-4}$
Endcap	$(8.0 \pm 0.5) \times 10^{-4}$

The E_T-dependent direct photon contamination is estimated using direct-photon measurements peformed at DØ [61]. The E_T-independent values are then corrected by $0.911 \times \exp(-0.0124\ E_T)$ in both the CC and EC in order to remove the expected direct photon contamination. The E_T-dependence of

this correction is due to the fact that the production cross section for direct photons falls slower as E_T increases than does the production cross section for jets. This correction introduces an uncertainty of $\pm 25\%$ to Prob(jet $\rightarrow \gamma$). The E_T-dependent Prob(jet $\rightarrow \gamma$) curves are shown in Figure 4.7. The estimated number of QCD background events for events with photons in the CC is 8.3 ± 2.1 events. The EC estimate is 3.2 ± 0.8 events.

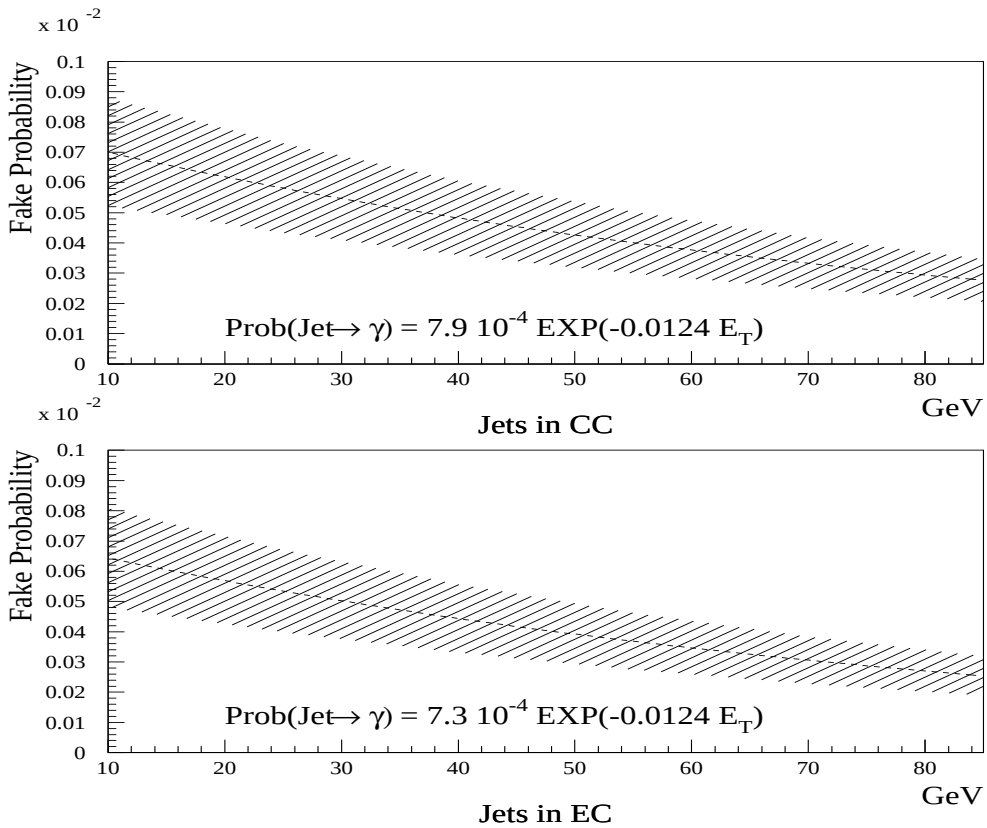

Figure 4.7. The probability for a jet to fake a photon in each calorimeter. Included is the correction due to direct photon contamination in the QCD sample. The shaded bands indicate the uncertainty, due mainly to the direct photon correction.

4.5.2 eeX Background

Another background that can be quite substantial comes from events with

two electrons and large amounts of missing transverse energy where the track pointing to one of the electrons is not reconstructed due to inefficiencies of the tracking chambers or the reconstruction program. If the electron with the lost track passes the photon identification cuts, the event can enter the $e\nu\gamma$ sample. The physics origin of such events can be $t\bar{t}$, WW, Z production, or QCD processes. Luckily the hits–in–road cuts are very good at rejecting electrons with a lost track, as described in Section 4.2.2.

The eeX background is estimated by repeating the $W\gamma$ analysis as described, but electron candidates are substituted for the photon candidates. The second electron must pass all of the photon ID cuts except the track veto and the hits-in-road cuts. Forty-two of these events are found in the Run 1b $W \rightarrow e\nu$ sample. Some of these events are $W\gamma$ events in which the photon converted, and should not be allowed to enter the background estimate of eeX[8].

The measured tracking efficiencies (see Section 4.2.1) indicate that the number of eeX background events in a $e\nu\gamma$ analysis without a hits-in-road cut would be 6.1 ± 0.4 events. The efficiency of the clean photon cuts for eliminating electrons with a lost track (see Section 4.2.2) reduces this number to 0.7 ± 0.1 events. There is a slight ambiguity when deciding on which electron in the $W+$ "e" search to consider as the one which would lose its track. This ambiguity is reduced by considering the tighter isolation and the lower E_T threshold required for the photon as well as the transverse mass cut on the $W \rightarrow e\nu$ candidate.

[8]In DØBAUR, the number of converted photons which are rejected are exactly proportional to the measured tracking efficiencies, plus a small correction which accounts for the additional rejection of converted photons from the hits–in–road cuts.

4.5.3 $Z\gamma$ Background

There is a small background to $e\nu\gamma$ that comes from $Z(ee)\gamma$ events in which one of the electrons enters a gap in the detector and gives rise to significant missing transverse energy. Because the DØ detector is hermetic, this background is very small. This background is estimated by generating Standard Model $Z\gamma$ events using the generator of Baur and Berger [62] followed by a full detector simulation using the GEANT program [50]. The fraction of $W(e\nu)\gamma$ events arising from $Z\gamma$ is 0.012 ± 0.002. The number of background events does not drastically change if the anomalous $ZZ\gamma$ couplings are allowed to fluctuate within the limits set by previous DØ studies [10] due to the more central nature of anomalous $ZZ\gamma$ events. The final $Z\gamma$ background estimate for this analysis is 0.4 ± 0.1 events.

4.5.4 $W(\tau\nu)\gamma$ Background

The final background to $e\nu\gamma$ comes from $p\overline{p} \rightarrow W(\tau\nu)\gamma$ where the τ lepton decays into an electron. This background was estimated using the ISAJET [51] program followed by a full detector simulation using the GEANT program [50]. This background is not large because the electronic decay of τ leptons results in electrons with significantly reduced E_T; the kinematic threshhold for electrons in this analysis is 25 GeV.

As in the case of the $Z\gamma$ background, the $\tau\nu\gamma$ background is estimated as a fraction of the total number of observed $e\nu\gamma$ events. 0.018 ± 0.002 of the observed events are due to $\tau\nu\gamma$. This background scales with anomalous $W\gamma$ couplings. The total number of predicted $\tau\nu\gamma$ events in this sample is 0.6 ± 0.1.

4.5.5 *Summary of Backgrounds*

The backgrounds to $W(e\nu)\gamma$ are summarized in Table 4.5. Also shown are the background estimates for the production events only. The background distributions are shown in Figure 4.5.

Table 4.5. Summary of $W(e\nu)\gamma$ backgrounds for Run 1b

Background	**All $W\gamma$ events**	**Production $W\gamma$ only**
W + jets	11.5 ± 2.3	8.8 ± 1.7
eeX	0.7 ± 0.1	0.5 ± 0.1
$Z\gamma$	0.4 ± 0.1	0.2 ± 0.1
$W(\tau\nu)$	0.6 ± 0.1	0.3 ± 0.1
Total	13.2 ± 2.3	9.8 ± 1.7

4.6 $\sigma(p\overline{p} \to W\gamma + X) \times BR(W \to e\nu)$ *Measurement*

By subtracting the total number of background events from the total number of observed $e\nu\gamma$ events, the total signal is measured to be $32.8^{+7.8}_{-6.8}$ events[9]. When restricting the study to the production events only, the number of signal events is measured to be $15.2^{+6.1}_{-5.0}$. The total signal is related to the cross section by

$$\sigma(p\overline{p} \to W\gamma + X) \times \mathrm{BR}(W \to e\nu) = \frac{\text{signal}}{\mathcal{L}\varepsilon}$$

where $\mathcal{L}$ is the total integrated luminosity (73.0 ± 3.9 pb^{-1}) and ε is the total selection efficiency, including geometrical acceptances.

The total efficiency ε was estimated by comparing the output of DØBAUR when the fast detector simulator was turned off with the results when all fast

[9]The asymmetric errors are the 1σ Poisson errors due to the statistics only. The uncertainty of the background is not included in these numbers, but is instead included in the systematic uncertainty of the cross section measurements.

detector effects were turned on. In the former case, all kinematic effects were also turned off except the p_T^γ and $\Delta R_{e\gamma}$ requirements. The total selection efficiency for the $W\gamma$ analysis is found to be about 4%. The total selection efficiency for production events is much higher, approximately 11%.

The measured cross section times branching ratio for $p\overline{p} \rightarrow W\gamma + X$ (with $p_T^\gamma > 10$ GeV/c and $\Delta R_{e\gamma} > 0.7$) in this work is measured to be:

$$\sigma(p\overline{p} \rightarrow W\gamma + X) \times \mathrm{BR}(W \rightarrow e\nu) = 11.19^{+2.66}_{-2.32} \pm 0.61\ (syst)\ \pm 0.56\ (lum)\ \mathrm{pb}$$

The Standard Model prediction is 12.5 ± 1.0 pb . The uncertainty on the prediction is from theoretical considerations such as the choice of structure functions and the p_T kick of the $W\gamma$ system due to hadronic recoil. See Section 3.8 for more details. The systematic uncertainty on the cross section measurement includes the uncertainty of the background estimates, as well as the uncertainty of the measured efficiencies and acceptances.

Production events are only about one-fifth of the Standard Model cross section, $\sigma \times \mathrm{BR} = 2.3 \pm 0.2$ pb. The comparable measured cross section for production events (with the same photon requirements) is found to be:

$$\sigma(p\overline{p} \rightarrow W\gamma + X) \times \mathrm{BR}(W \rightarrow e\nu) = 1.84^{+0.75}_{-0.61} \pm 0.10\ (syst)\ \pm 0.09\ (lum)\ \mathrm{pb}$$

From these results it is possible to say that the observed number of $W\gamma$ events is entirely consistent with the Standard Model. The confidence limits on the anomalous $WW\gamma$ couplings will be derived in the next chapter.

CHAPTER 5

LIMITS ON THE ANOMALOUS COUPLINGS

In this chapter the observed $W\gamma$ events will be used to directly set limits on the possible anomalous $WW\gamma$ couplings. The limits will be set by both comparing the total number of $W\gamma$ events with the predicted cross section and by comparing the observed differential cross section $d\sigma/dp_T^\gamma$ with the Monte Carlo predictions. The tightest limits will be obtained by restricting the study to the production $W\gamma$ events only. These results will be combined with the previously published DØ $W\gamma$ results.

5.1 Limits from the Total Cross Section Measurement

It follows from the form of the $WW\gamma$ interaction vertex that the anomalous coupling contributions to the cross section of the process $p\overline{p} \to W\gamma$ are quartic in $(\Delta\kappa, \lambda)$ and $(\tilde{\kappa}, \tilde{\lambda})$, so the total cross section of $p\overline{p} \to W\gamma$ as a function of two couplings can be expressed in the following bilinear form:

$$\sigma(\Delta\kappa, \lambda) = \sigma_{\rm SM} + a_0\Delta\kappa + a_1\Delta\kappa^2 + b_0\lambda + b_1\lambda^2 + c\Delta\kappa\lambda, \qquad (5.1)$$

where $\sigma_{\rm SM}$ is the Standard Model cross section and a_i, b_i and c are coefficients. A similar form exists for the CP–violating parameters $\tilde{\kappa}$ and $\tilde{\lambda}$[1]. Compare

[1]Couplings with different CP–parity do not interfere with each other, so there are no cross terms in 5.1 which are proportional to the product of a CP–conserving and CP–violating coupling. In this work (and elsewhere) they are considered independently.

Equation 5.1 with Figure 2.2.

It is important to note that as one coupling parameter is varied the overall detection efficiency ε (trigger, acceptance and selection ID) is flat when compared to the cross section, so that a bilinear form for Equation 5.1 is valid. See Figure 5.1 (a). The detection efficiency rises slightly for anomalous cases,

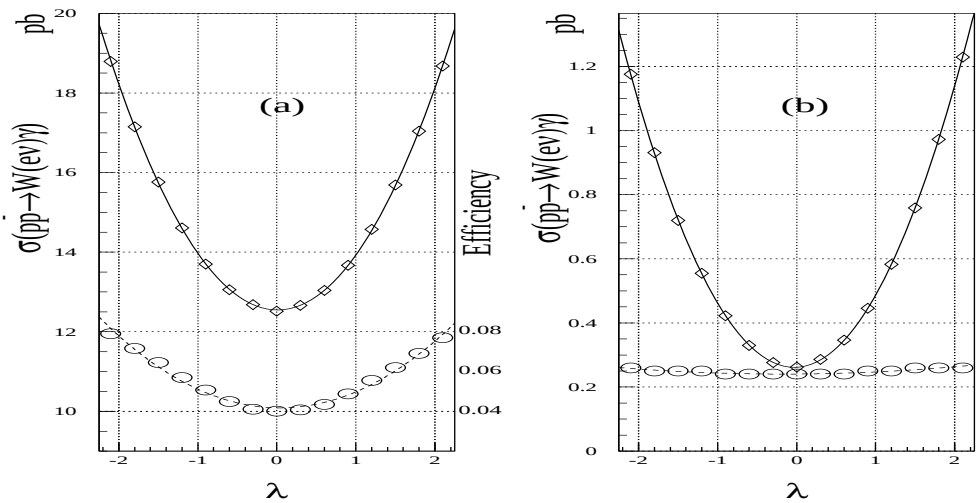

Figure 5.1. (a) The predicted cross section for $p\overline{p} \rightarrow W(e\nu)\gamma$ (diamonds) and the total detection efficiency (circles) as a funtion of λ. Notice the different scales used for each. (b) The cross section times efficiency for $\sigma(p\overline{p} \rightarrow W(e\nu)\gamma)$ as a function of the coupling parameter λ for production events ($M_T(\gamma e;\nu) > 90$ GeV/c^2) (diamonds), and decay events ($M_T(\gamma e;\nu) < 90$ GeV/c^2) (circles).

due mainly to the increased trigger efficiency (higher p_T photons) and the increased acceptance (more central objects), but it has much less sensitivity to the anomalous couplings than the total cross section.

As mentioned previously, the counting experiment can be used to set limits on the anomalous couplings because of the pronounced rise in the total cross section for coupling parameters away from their Standard Model values. The best method for establishing conservative upper limits on the anomalous couplings is to use the Bayesian approach to set confidence level (CL) upper

limits for the expected cross section as a function of the anomalous couplings ($\sigma(\Delta\kappa, \lambda)$).

The expected number of events μ from an experiment can be described as

$$\mu = b + \mathcal{L}\varepsilon\sigma(\Delta\kappa, \lambda) \tag{5.2}$$

where b is the expected background, $\mathcal{L}$ is the integrated luminosity, and ε is the total detection efficiency of the experiment. The probability (or *likelihood*) for observing n events with a given expectation value of μ is given by the Poisson probability

$$P = \frac{e^{-\mu}\mu^n}{n!} \tag{5.3}$$

which becomes

$$P = \frac{e^{-(b+\mathcal{L}\varepsilon\sigma(\Delta\kappa,\lambda))}(b + \mathcal{L}\varepsilon\sigma(\Delta\kappa, \lambda))^n}{n!} \tag{5.4}$$

The parameters $\mathcal{L}$, ε, and b are referred to as *nuisance parameters*; $\sigma(\Delta\kappa, \lambda)$ is the measurement of interest. The values of $\mathcal{L}$, ε, and b are measured with some uncertainty (σ) which must affect Equation 5.4. The nuisance parameters are integrated out of 5.4 by allowing a particular parameter to vary about its measured value with a Gaussian distribution:

$$P = \int \mathcal{G}_{\mathcal{L}}\, d\mathcal{L} \int \mathcal{G}_b\, db \int \mathcal{G}_\varepsilon\, d\varepsilon\, \frac{e^{-(b+\mathcal{L}\varepsilon\sigma(\Delta\kappa,\lambda))}(b + \mathcal{L}\varepsilon\sigma(\Delta\kappa, \lambda))^n}{n!}. \tag{5.5}$$

The Gaussian distribution distribution $\mathcal{G}$ for a nuisance parameter x has a nominal mean of $\mu = 1$, and a rms deviation of σ_x:

$$\mathcal{G}_x = \frac{1}{\sigma_x\sqrt{2\pi}} \exp \frac{-(x-\mu)^2}{2\sigma_x^2}. \tag{5.6}$$

Each of the uncertainties is necessarily uncorrelated. This method of folding uncertainties into the likelihood function has an advantage when combining

results from different experiments that share common systematics. This is exactly how the earlier DØ $W\gamma$ results will be later combined with the results of this thesis. For the purposes of this work, there are three nuisance parameters. They are:

- The efficiencies associated with the decay lepton from the W boson,
- The expected background in the sample (dominated by QCD), and
- The uncertainty of the integrated luminosity, the efficiencies associated with the photon, and the theoretical uncertainties of the Monte Carlo.

The uncertainties between these three nuisance parameters are uncorrelated, and chosen in such a way as to easily combine results from channels which share common systematics. The values of the nuisance parameters and their associated uncertainties for the Run 1b $e\nu\gamma$ limits estimates are summarized in Table 5.4.

One final note before the limits are presented. One background to $p\overline{p} \rightarrow W(e\nu)\gamma$ is the related process $p\overline{p} \rightarrow W(\tau\nu)\gamma$ where the τ lepton decays into an electron. This background is proportional to the predicted $e\nu\gamma$ cross section for all possible anomalous couplings, so the predictions from DØBAUR are scaled upwards by the fraction of expected $\tau\nu\gamma$ events rather than considering them part of the background proper, q.v. Section 4.5.4.

The cross sections $\sigma(\Delta\kappa, \lambda)$ were generated using the DØBAUR program with a dipole form factor scale of $\Lambda = 1.5$ TeV. 15×15 grids were generated for the pairs of common CP–parity anomalous couplings, where each coupling varied between -2.1 and $+2.1$ in steps of 0.3. The resulting grids are within the limits imposed by unitarity and cover the variation of allowed anomalous couplings from previous $W\gamma$ experiments at the Tevatron [33].

For later convenience the negative log-likelihood, $L \equiv -\log P$, is used in place of the Poisson probability of Equation 5.4. This likelihood is generated over the entire grid of anomalous couplings, and the result is fit to a bilinear function, and the maximum value of the negative log-likelihood serves a role similar to the constant parameter of Equation 5.1. In the case of fits to the negative log-likelihood, the s-standard-deviation errors are evaluated along the contour $L_{\max} - s^2/2$ [5]. Some values of s and the associated confidence level intervals are listed in Table 5.1.

Table 5.1. Some confidence level (CL) intervals

s	CL interval	$-s^2/2$
1σ	68.27%	-0.50
1.96σ	95.00%	-1.92
2σ	95.45%	-2.00
3σ	99.73%	-4.50

The contours showing the 95% and 68% CL limits on the pair of CP–conserving anomalous couplings from the cross section measurement are shown in Figure 5.2. It is the practice to quote the limits on one coupling when all of the other couplings are set to their Standard Model values. These *axis limits* are summarized in Figure 5.2.

5.2 Limits from Fitting the p_T^γ Spectrum

The method of obtaining limits on anomalous couplings from the total number of observed events is straightforward but it ignores extra information that may be found in the kinematic distributions of $W\gamma$ events. The differential distribution $d\sigma/dp_T^\gamma$ is particluarly sensitive to anomalous couplings[2]. See

[2]The differential cross section $d\sigma/dp_T^\gamma$ as a function of the anomalous couplings is also well

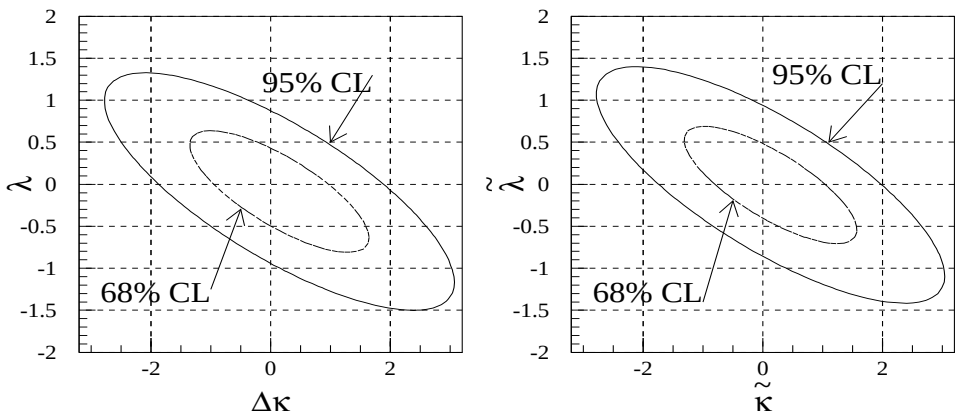

Run 1b W(eν)γ Cross Section Results	
68% axis limits	
$-0.9 < \Delta\kappa < 1.0$	$-0.9 < \tilde{\kappa} < 1.1$
$-0.5 < \lambda < 0.4$	$-0.4 < \tilde{\lambda} < 0.5$
95% axis limits	
$-1.9 < \Delta\kappa < 1.9$	$-1.8 < \tilde{\kappa} < 2.0$
$-0.9 < \lambda < 0.9$	$-0.9 < \tilde{\lambda} < 0.9$
Unitarity limits	
$\lvert\Delta\kappa\rvert < 3.3$	$\lvert\tilde{\kappa}\rvert < 23.3$
$\lvert\lambda\rvert < 1.8$	$\lvert\tilde{\lambda}\rvert < 1.8$

Figure 5.2. Run 1b limits on the anomalous couplings from the $p\overline{p} \to W(e\nu)\gamma$ cross section measurement. A dipole form factor scale of $\Lambda = 1.5$ TeV was assumed.

Figure 2.3.

A comparison of the observed p_T^γ spectrum with predictions from DØBAUR is particularly useful for the following reasons:

- The shape of the dominant background is well understood.
- The experimental resolution of p_T^γ is very good.
- The photon is a common object for both $W(e\nu)\gamma$ and $W(\mu\nu)\gamma$ analyses, allowing for a well understood combination of both channels.

---

described by a bilinear fit.

- The drop in $d\sigma/dp_T^\gamma$ as p_T^γ increases allows the non-observation of high p_T^γ events to be used as an extra tool when setting limits.

It is possible to compare an observed p_T^γ spectrum with the differential cross section using binned or unbinned likelihood fits. In this work a binned likelihood fit is used. Complete discussion of the differences between binned and unbinned likelihood fits can be found elsewhere. In short, unbinned fits rely on the precise shape of $d\sigma/dp_T^\gamma$ and the backgrounds over the range of measurements. Unbinned fits may also be constrained by the total number of observed events and the total predicited cross section.

Unbinned fits are sensitive to the resolution and smearing of measured data, but in the case of a binned fit, the bins can be chosen to accomodate the resolution of the measured quantity of interest, here p_T^γ. Each of the bins is uncorrelated, and a Poisson likelihood for observing n_i events in the ith bin is, as in Equation 5.2,

$$P_i = \frac{e^{-(b_i+\mathcal{L}\varepsilon\sigma_i)}(b_i + \mathcal{L}\varepsilon\sigma_i)^{n_i}}{n_i!} \tag{5.7}$$

The data is usually binned in such a way as to have many events per bin. The lower edge of the first bin is set at the lowest measured p_T^γ for the experiment, in this work the lowest p_T^γ bin starts at 10 GeV/c. A modification of more standard binned-likelihood methods is to include a final bin with no observed events [63]. This is a *null experiment*; it uses the non-observation of high p_T^γ events to improve the limits on anomalous couplings. This is a particularly valuable technique for this thesis as the Standard Model predicts a sharp decrease in the differential cross section as p_T^γ increases. The lower edge of the last bin is set far enough above the last observed data point to insure against the possibility of the last event fluctuating into the empty bin.

The probability of observing the total histogram of N bins is the multiplication of the individual probabilities P_i,

$$P = \prod_{i=1}^{N} \frac{e^{-(b_i+\mathcal{L}\varepsilon\sigma_i)}(b_i + \mathcal{L}\varepsilon\sigma_i)^{n_i}}{n_i!} \tag{5.8}$$

The negative log-likelihood of Equation 5.8 is

$$L \equiv -\log P = \sum_{i=1}^{N}(n_i \log(b_i + \mathcal{L}\varepsilon\sigma_i) - (b_i + \mathcal{L}\varepsilon\sigma_i)), \tag{5.9}$$

where the constant term has been omitted.

Table 5.2. Data used in the binned fit to p_T^γ by bin. The $W(\tau\nu)\gamma$ background has been removed from the background estimates.

p_T^γ **Bin (GeV/c)**	**Number Observed**	**Background**
10 - 15	17	5.6
15 - 20	17	3.0
20 - 30	6	2.4
30 - 50	6	1.2
50 and above	0	0.4

Some remarks about the binned likelihood approach are in order. The binned likelihood method described here is insensitive to the total number of bins, as long as there are at least two. One bin is needed for the observed events, and one is needed for the null experiment[3]. The *a posteori* choice of bins is completely unbiased; the lower edge of the last p_T^γ bin conveys the most information, and the placement of that bin edge is driven by the experimental resolution [63]. In this analysis, the last bin begins at 50 GeV/c. This is above the p_T^γ resolution of the highest observed $W(e\nu)\gamma$ candidate. If the lower edge

[3]A legitimate mathematical question that will shortly arise is "Why does this work continue to use five bins when the final results require only two?" It is the purpose of this thesis to convey as much information as possible. The extra information about the shape of the p_T^γ spectra may not be necessary for the purposes of setting limits on the anomalous couplings, but it could prove useful to future studies.

of the empty bin is raised to 55 GeV/c, the final limits on anomalous couplings do not change. Table 5.2 shows the choice of bins and the number of events and background in each. See also Figure 4.5.

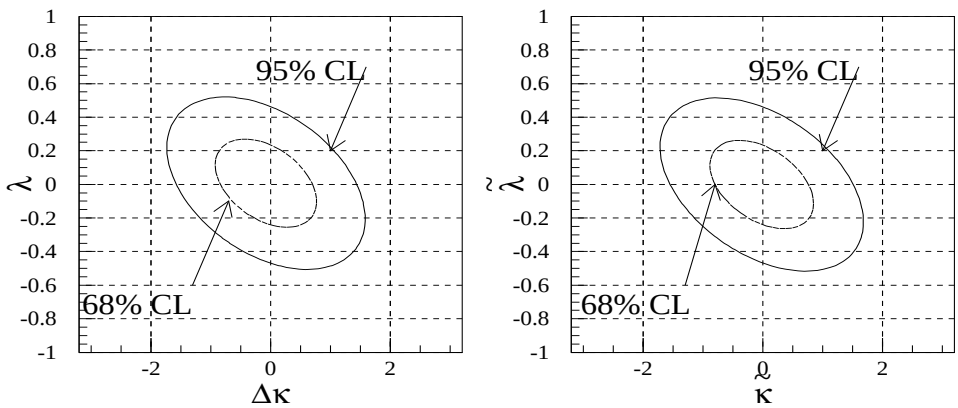

Run 1b W(eν)γ p_T^γ Fit Results	
68% axis limits	
$-0.8 < \Delta\kappa < 0.7$	$-0.8 < \tilde{\kappa} < 0.8$
$-0.2 < \lambda < 0.2$	$-0.2 < \tilde{\lambda} < 0.2$
95% axis limits	
$-1.6 < \Delta\kappa < 1.5$	$-1.6 < \tilde{\kappa} < 1.5$
$-0.5 < \lambda < 0.5$	$-0.5 < \tilde{\lambda} < 0.5$
Unitarity limits	
$\lvert\Delta\kappa\rvert < 3.3$	$\lvert\tilde{\kappa}\rvert < 23.3$
$\lvert\lambda\rvert < 1.8$	$\lvert\tilde{\lambda}\rvert < 1.8$

Figure 5.3. Run 1b limits on the anomalous couplings from the fit to the p_T^γ spectrum. A dipole form factor scale of $\Lambda = 1.5$ TeV was assumed.

The resulting limits are tighter than those from a simple fit to the total cross section, as expected. The contours showing the 95% and 68% CL limits on the pair of CP–conserving anomalous couplings are shown in Figure 5.3.

5.3 *Limits from the Production Events*

This work has already shown that it is possible to put tight constraints on possible anomalies in the $WW\gamma$ interaction. So far the data used in this work was from all of the diagrams shown in Figure 2.1. It is obvious that the only diagram which carries information about the $WW\gamma$ vertex is the self–coupling diagram. If this study was restricted to only that diagram, even tighter limits on anomalous self-couplings could be set. Unfortunately is impossible to decide which diagram a particular $W(e\nu)\gamma$ originated from with complete certainty.

It is possible to remove most of the events arising from one of the uninteresting diagrams, the decay graph, while maintaining strong sensitivity to anomalous couplings. This is done be requiring the three–body cluster mass to be above 90 GeV/c^2. This eliminates almost all of the decay diagrams (which have a three–body mass close to that of the W boson) while keeping a significant amount of $WW\gamma$ and production events. The high three–body mass events have the most sensitivity to anomalous couplings. See Figure 5.1 (b). This particular analysis has never been attempted before because of the limited statistics available to the previous analyses.

Table 5.3. Data used in the binned fit to p_T^γ for the production events. The $W(\tau\nu)\gamma$ background has been removed from the background estimates.

p_T^γ **Bin (GeV/c)**	**Number Observed**	**Background**
10 - 15	6	3.6
15 - 20	9	2.2
20 - 30	4	2.1
30 - 50	6	1.2
50 and above	0	0.4

After the $M_T(\gamma e;\nu) > 90$ GeV requirement, there are twenty-five candi-

dates left with an estimated background of 9.8 ± 1.7 events, q.v. Table 4.5.

The limits setting procedure is identical to the method described in Section 5.2. A negative log-likelihood fit to the p_T^γ spectrum was performed over the same range of anomalous couplings as described earlier. See Table 5.3 for details. The contour limits on anomalous couplings are shown in Figure 5.4. As expected, the improved sensitivity to anomalous couplings results in tighter

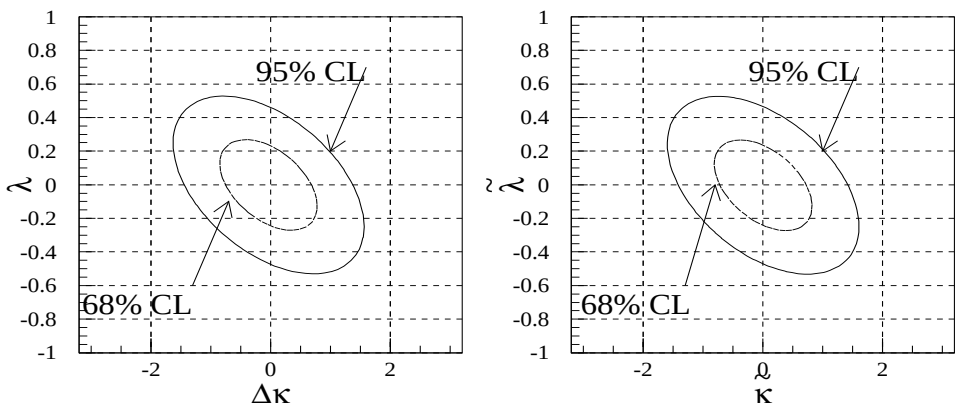

Run 1b W(eν)γ Results from p_T^γ Fit to the Production Events	
68% axis limits	
$-0.8 < \Delta\kappa < 0.7$	$-0.7 < \tilde{\kappa} < 0.7$
$-0.2 < \lambda < 0.2$	$-0.2 < \tilde{\lambda} < 0.2$
95% axis limits	
$-1.4 < \Delta\kappa < 1.4$	$-1.4 < \tilde{\kappa} < 1.4$
$-0.5 < \lambda < 0.5$	$-0.5 < \tilde{\lambda} < 0.5$
Unitarity limits	
$\lvert\Delta\kappa\rvert < 3.3$	$\lvert\tilde{\kappa}\rvert < 23.3$
$\lvert\lambda\rvert < 1.8$	$\lvert\tilde{\lambda}\rvert < 1.8$

Figure 5.4. Run 1b limits on the anomalous couplings from the fit to the p_T^γ spectrum of the production events. A dipole form factor scale of $\Lambda = 1.5$ TeV was assumed.

limits. These results are currently the most stringent limits on anomalous couplings from a direct test of the $WW\gamma$ vertex in the world. The next section will make a further improvement on the $W\gamma$ analysis by combining these results with the previously published DØ results.

5.4 Combination of this Work with Previous Results

The previous DØ $W\gamma$ analysis is summarized in Appendix A. Each analysis (Run 1a $W(e\nu)\gamma$, Run 1a $W(\mu\nu)\gamma$, and Run 1b $W(e\nu)\gamma$) can be considered a different experiment with some common systematic uncertainties. Because each of these experiments made identical kinematic requirments on the photons ($\Delta R_{e\gamma} > 0.7$ and $p_T^\gamma >$ 10 GeV/c) it is natural to combine the work in order to decrease the statistical errors present in these individually small samples. It is straightforward to combine the amount of signal in each experiment to estimate the predicted cross section times branching ratio to leptons. When the Run 1a $W\gamma$ results are combined with this work, the total measured cross section from the $49.4^{+9.4}_{-8.3}$ signal events is:

$$\sigma(p\overline{p} \rightarrow W\gamma + X) \times \mathrm{BR}(W \rightarrow \ell\nu) = 11.22^{+2.13}_{-1.88} \pm 0.69\ (syst)\ \pm 0.61\ (lum)\ \mathrm{pb}$$

When attempting to improve the limits on anomalous couplings by combining different experiments, it is extremely important to correctly account for any common systematic effects between the analyses. These three experiments took place at the same detector, so the theoretical and luminosity related uncertainties are exactly correlated. A likelihood fit to the p_T^γ spectrum of the combined work will be used because the photon identification uncertainty and the uncertainty of the background estimate is common to each experiment. Finally the Run 1a and Run 1b $W(e\nu)\gamma$ analyses have common systematics involving electron reconstruction and identification.

The systematic uncertainties are then grouped together into into four nuisance parameters, as described in Section 5.1. One parameter is for the uncertainty on the backgrounds, one is for the theoretical, luminosity and photon–dependent uncertainties, and there is one parameter for each of the

lepton–related uncertainties. Some of the uncertainties decreased between Runs 1a and 1b because of improved systematics in the diagnostic samples (e.g. $Z \rightarrow ee$, QCD background) while some uncertainties increased, such as the uncertainty associated with the addition of the hits–in–road cut on the photons. When an uncertainty in a nuisance parameter changed between the two runs, a new uncertainty was assigned to that parameter that was weighted by the total integrated luminosity of each experiment.

Table 5.4. The values of the nuisance parameters used in the limits setting procedure

Source of error	Nuisance Parameters		
	$e\nu$ channel Run 1a	$\mu\nu$ channel Run 1a	$e\nu$ channel Run 1b
Photon, Luminosity and Theoretical			
Luminosity Uncertainty	5.4%	5.4%	5.4%
Structure function choice	6.0%	6.0%	6.0%
Structure function scale	1.0%	1.0%	1.0%
$p_T^{W\gamma}$ kick	3.9%	3.9%	4.9%
Conversion Probability	5.0%	5.0%	5.0%
Random track overlap	1.0%	1.0%	0.5%
Photon ID efficiency	7.0%	7.0%	3.1%
Total ($\sigma_{\mathcal{L}}$)	12.5%	12.5%	11.2%
Leptons			
Trigger and ID efficiency (σ_ε)	5.2%	11.0%	1.3%
Backgrounds			
Total Background (σ_b)	50.0%	50.0%	25.4%

The complete equation used for the combined analysis has the form

$$P = \int \mathcal{G}_{\mathcal{L}}\, d\mathcal{L} \int \mathcal{G}_b\, db \left(\int \mathcal{G}_{\varepsilon_e}\, d\varepsilon_e\, f_e \; + \; \int \mathcal{G}_{\varepsilon_\mu}\, d\varepsilon_\mu\, f_\mu \right) \tag{5.10}$$

where f_e and f_μ are the Poisson probabilities for each W decay channel, as in Equation 5.4. Each of the nuisance parameters in Equation 5.10 is convoluted

with a Gaussian distribution $\mathcal{G}$ of width σ equal to the uncertainty of the parameter in question[4].

The contour limits on anomalous $W\gamma$ couplings are shown in Figure 5.5. These limits are the result of combining the DØ Run 1a $e\nu\gamma$ and $\mu\nu\gamma$ analyses with the results of Section 5.3. They are currently the tightest limits on anomalous $W\gamma$ couplings from a direct measurement of the $WW\gamma$ vertex. The next chapter will compare these results with previous studies.

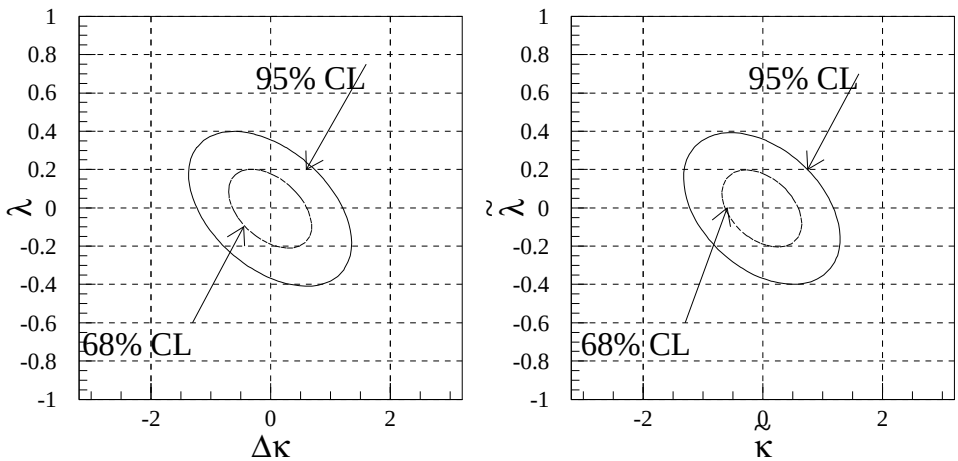

Combined Run 1a (eνγ, μνγ) and Run 1b (eνγ) Results	
68% axis limits	
$-0.6 < \Delta\kappa < 0.6$	$-0.6 < \tilde{\kappa} < 0.6$
$-0.2 < \lambda < 0.2$	$-0.2 < \tilde{\lambda} < 0.2$
95% axis limits	
$-1.2 < \Delta\kappa < 1.2$	$-1.2 < \tilde{\kappa} < 1.2$
$-0.4 < \lambda < 0.4$	$-0.4 < \tilde{\lambda} < 0.4$
Unitarity limits	
$\lvert\Delta\kappa\rvert < 3.3$	$\lvert\tilde{\kappa}\rvert < 23.3$
$\lvert\lambda\rvert < 1.8$	$\lvert\tilde{\lambda}\rvert < 1.8$

Figure 5.5. Limits on the anomalous couplings $W\gamma$ from the fit to the p_T^γ spectrum of the Run 1a events and the Run 1b production events. A dipole form factor scale of $\Lambda = 1.5$ TeV was assumed.

[4]In practice, the convolution of the Poisson probability with each nuisance parameter's Gaussian takes place at fifteen evenly spaced points between $\pm 3\sigma$. In this scheme the nuisance parameters are not allowed to fluctuate below zero; to do so would be unphysical.

CHAPTER 6

CONCLUSIONS

This work made a rigorous study of the standard electroweak model through a test of the $WW\gamma$ interaction. 73 pb^{-1} of integrated luminosity collected at DØ during Tevatron Run 1b were used. Forty-six $W\gamma$ candidate events were observed through the electronic decay of the W boson. Twenty-five of these events can be attributed to the initial state radiation and self–coupling hypotheses. Both the total number of events and the kinematic distributions of the events are consistent with the Standard Model expectations.

These results were combined with the earlier DØ $W\gamma$ study that was done using 13.8 pb^{-1} of data from Run 1a. From this combined analysis the total cross section times the branching ratio of W boson decay to leptons is measured to be:

$$\sigma(p\overline{p} \rightarrow W\gamma + X) \times \mathrm{BR}(W \rightarrow \ell\nu) = 11.22^{+2.13}_{-1.88} \pm 0.69\ (syst)\ \pm 0.61\ (lum)\ \mathrm{pb}$$

for photons with p_T above 10 GeV which are spatially separated from the decay leptons by $\Delta R_{\ell\gamma} > 0.7$.

This thesis also directly set limits on the anomalous CP–conserving ($\Delta\kappa$,λ) and CP–violating ($\tilde{\kappa}$,$\tilde{\lambda}$) parameters using a variety of different techniques. The most strict limits were set when a binned likelihood fit to the p_T^{γ} spectrum of

the Run 1b production $e\nu\gamma$ events is combined with the fit to the p_T^γ spectrum of the Run 1a $e\nu\gamma$ and $\mu\nu\gamma$ events. At a confidence level of 95%, the limits on the couplings (when all other couplings are held at their Standard Model values) are:

$$-1.2 < (\Delta\kappa, \tilde{\kappa}) < 1.2 \text{ and } -0.4 < (\lambda, \tilde{\lambda}) < 0.4 \,.$$

These are currently the tightest directly-obtained limits on anomalous $WW\gamma$ couplings in the world. Figure 6.1 compares the limits on the CP–conserving coupling parameters with the tightest limits from another direct experiment (CDF) and an indirect experiment (CLEO). Also shown is the expectation for the minimal $U(1)_{\mathrm{EM}}$ coupling, which is currently excluded at the 90% CL.

Assuming that the Standard Model is correct, these limits should improve by another 15% when combined with the $\mu\nu\gamma$ results from Run 1b. Another short Tevatron run, Run 1c, delivered approximately 10 pb^{-1} of integrated luminosity to both CDF and DØ. DØ maintained a trigger to collect both $e\nu\gamma$ and $\mu\nu\gamma$ events, but the extra events can improve these results by no more than a few percent. Should DØ and CDF decide to combine their individual $W\gamma$ results, the limits could improve by as much as 30% beyond what is shown here[1]. If certain assumptions about the $WW\gamma$ and WWZ couplings are made, much tighter limits can be set by combining the results of the $p\overline{p} \to W\gamma$ analyses with the $p\overline{p} \to WW$ studies [8]. Such work involving the Run 1a data is already in progress at DØ [64].

The most drastic improvement in limiting the anomalous couplings to their Standard Model values will occur at future experiments such as LEP II, LHC and the upgraded Tevatron. Higher center-of-mass energies and/or

[1]A combination of the DØ and CDF $W\gamma$ results is feasible only if the common systematics between the two experiments are properly taken into account.

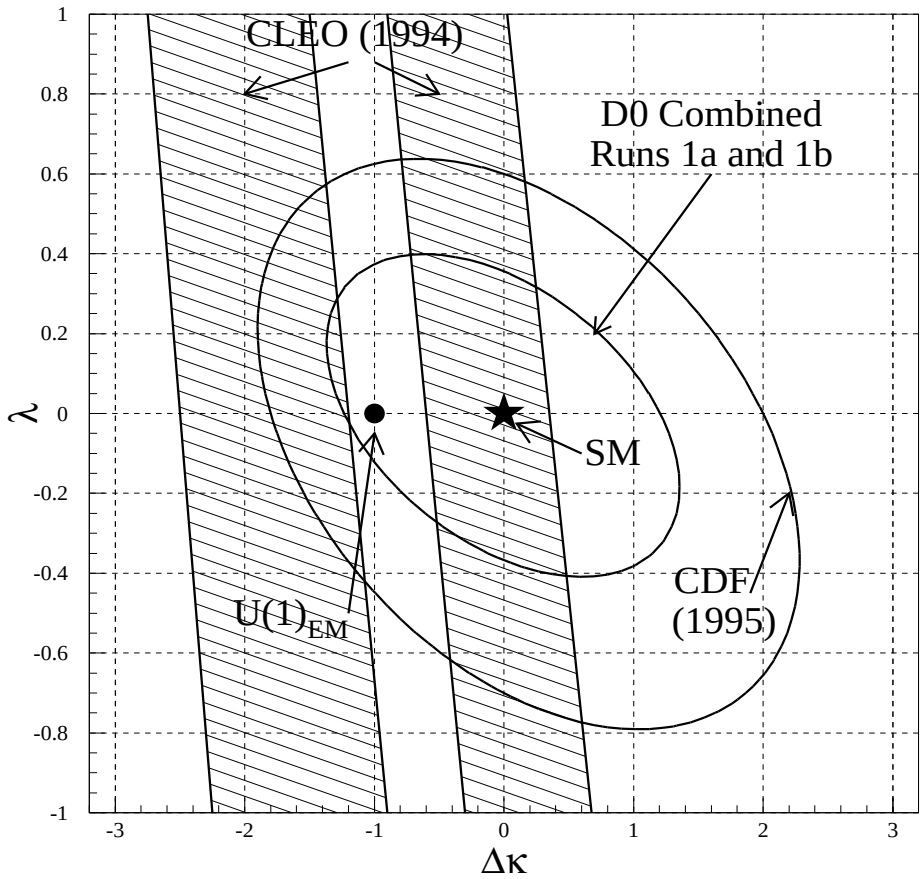

Figure 6.1. Comparison of the 95% CL limits on $\Delta\kappa$ and λ from this experiment with the published CLEO and preliminary CDF results. The CDF results use $e\nu\gamma$ and $\mu\nu\gamma$ events found in 67 pb^{-1} of data from a combined Run 1a and Run 1b analysis. The Run 1a DØ result was similar to the CDF (1995) ellipse. The direct experiments assume a dipole form factor scale of $\Lambda = 1.5$ TeV.

much larger amounts of integrated luminosity are the only ways in which the limits from the current Tevatron run will be surpassed. Beyond improving limits, there remains the task of observing the radiation zero (RAZ) in $W\gamma$ production. CDF may yet observe the RAZ from the data collected during Run 1. An upgraded DØ detector with a central magnetic field will almost certainly be able to observed a clear RAZ when the inverse femtobarn set of data from Tevatron Run 2 becomes available.

APPENDIX A

RUN 1A $W\gamma$ RESULTS

The Run 1a $W\gamma$ analysis [33] combined results from the electron and muon decay channels of the W boson. Each channel used 13.8 ± 0.7 pb^{-1} of data. The Run 1a $W(e\nu)\gamma$ analysis was extremely similar to the analysis described in this thesis. The kinematic and fiducial requirements on the electron and photon were identical for Runs 1a and 1b. The quality cuts on the electron were not changed between the two runs. The photon ID for Run 1b was improved by imposing the clean photon cuts (q.v. Section 4.2.2 and Appendix B); this cut was not used in Run 1a.

The $W(\mu\nu)\gamma$ analysis necessarily has some differences from the $W(e\nu)\gamma$ work, but each channel had a common photon requirement. The primary difference bewteen the two channels is that the p_T^μ was required to be above 15 GeV/c and the $\not\!\!E_T$ was only required to be above 15 GeV. The fiducial volume of the detector used for muon studies was divided into two pseudorapidity regions: $|\eta| < 1.0$ and $1.0 < |\eta| < 1.7$. Muon–specific quality cuts were imposed on the $W(\mu\nu)\gamma$ candidates, they are described in detail elsewhere [33]. The final number of events and the expected background for each channel is shown in Table A.1.

The measured cross section times branching ratio for $p\overline{p} \to W(\ell\nu)\gamma$ (with

Table A.1. Summary of Run 1a $W(e\nu)\gamma$ and $W(\mu\nu)\gamma$ data and backgrounds

Channel	$W(e\nu)\gamma$	$W(\mu\nu)\gamma$
Number Observed	11	12
Backgrounds:		
W + jets	1.7 ± 0.9	1.3 ± 0.7
$Z\gamma$	0.11 ± 0.02	2.7 ± 0.8
$W(\tau\nu)\gamma$	0.17 ± 0.02	0.4 ± 0.1
Total Background	2.0 ± 0.9	4.4 ± 1.1
Total Signal	$9.0^{+4.2}_{-3.1}$	$7.6^{+4.4}_{-3.2}$

$p_T^\gamma > 10$ GeV/c and $\Delta R_{\ell\gamma} > 0.7$) was measured to be:

$$\sigma(p\overline{p} \rightarrow W\gamma + X) \times \mathrm{BR}(W \rightarrow \ell\nu) = 11.26^{+4.00}_{-3.26} \pm 0.62\ (syst)\ \pm 0.61\ (lum)\ \mathrm{pb}$$

A binned likelihood fit to the combined p_T^γ spectra from the two channels (see Figure A.1) was used to set limits on the anomalous couplings, as described in Section 5.2. A dipole form factor with scale $\Lambda = 1.5$ TeV was assumed. 95% confidence level (CL) limits on the CP–conserving anomalous coupling parameters were found to be

$$-1.6 < \Delta\kappa < 1.8\ (\lambda = 0)\ \text{ and }\ -0.6 < \lambda < 0.6\ (\Delta\kappa = 0)$$

for the CP–conserving parameters, while the limits on the CP–violating parameters were quoted as

$$-1.7 < \tilde{\kappa} < 1.7\ (\tilde{\lambda} = 0)\ \text{ and }\ -0.6 < \tilde{\lambda} < 0.6\ (\tilde{\kappa} = 0)\ .$$

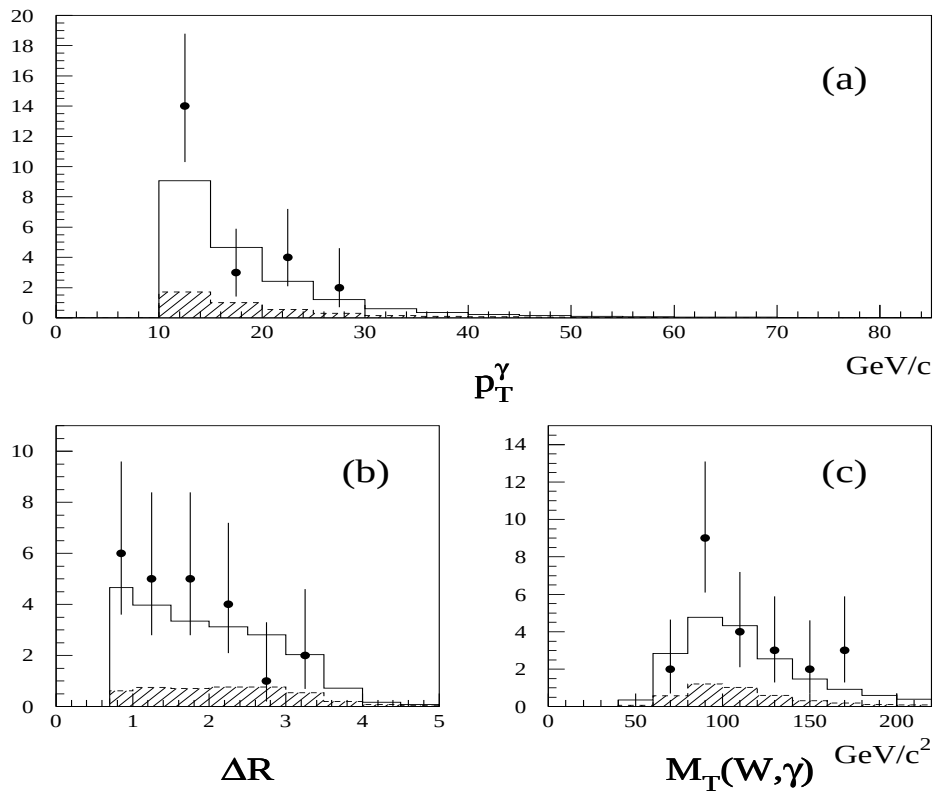

Figure A.1. (a) The p_T^γ spectrum for the 23 Run 1a $W\gamma$ candidates. The $\Delta R_{\ell\gamma}$ (b) and $M_T(\gamma\ell;\nu)$ (c) distributions are also shown. The points are the data with 1σ error bars. The solid histograms are the Monte Carlo predictions plus the background estimates (shown in the shaded histograms).

APPENDIX B

RUN 1B $W\gamma$ ANALYSIS USING BOTH "DIRTY" AND "CLEAN" PHOTONS

In a low statistics analysis such as this one it is important to not artificially deflate the amount of expected events by adding extremely tight quality cuts. To do so runs the risk of biasing an experiment away from what it is trying to measure. In the case of the Run 1b $W(e\nu)\gamma$ analysis shown in this work, a cut on the number of hits found in roads between event vertices and photon calorimeter clusters is used to reject a significant amount of background. This hits–in–road cut is described in Section 4.2.2 and has an overall efficiency of approximately 79%. Events which pass this cut are said to have *clean* photons while the events which fail are labeled *dirty*.

The p_T^γ spectrum for the $W\gamma$ candidates before this cut is applied is shown in Figure B.1. Sixty-four events pass the event selection criteria. The background estimates are summarized in Table B.1.

The QCD background is larger because the fake rates are somewhat higher when the hits–in–road cuts are not applied. The new E_T-independent values of Prob(jet $\rightarrow \gamma$) are $(10.9 \pm 0.3) \times 10^{-4}$ for photons in the CC, and $(12.9 \pm 0.3) \times 10^{-4}$ for photons in the EC. If these numbers are compared with the values in Table 4.4 and the efficiencies of the hits–in–road cuts it is obvious that in the central region the hits–in–road cuts do not improve the rejection

Table B.1. Summary of backgrounds for the $W\gamma$ analysis both with and without the hits–in–road cuts

Background	Clean Photons Only	Total Sample
W + jets	11.5 ± 2.3	15.6 ± 2.6
eeX	0.7 ± 0.1	6.1 ± 0.4
$Z\gamma$	0.4 ± 0.1	0.5 ± 0.1
$W(\tau\nu)$	0.6 ± 0.1	0.8 ± 0.1
Total	13.2 ± 2.3	23.0 ± 3.0

of QCD events; the change in Prob(jet $\rightarrow \gamma$) is entirely due to the inefficiency of the extra cut. The hits–in–road cuts do assist in the extra rejection of QCD background in the forward region.

The total number of signal events in the more primitive analysis is then $41.0^{+9.0}_{-8.0}$ and the cross section for $p_T^\gamma > 10$ GeV/c and $\Delta R_{e\gamma} > 0.7$ is measured to be

$$\sigma(p\overline{p} \rightarrow W\gamma + X) \times \mathrm{BR}(W \rightarrow e\nu) = 11.10^{+2.44}_{-2.17} \pm 0.61\ (syst)\ \pm 0.55\ (lum)\ \mathrm{pb},$$

which is completely consistent with results shown in Section 4.6. The loss of 8.2 signal events from the sample because of the hits–in–road cut is also completely consistent with the measured efficiency of the cut.

The signal–to–background ratio is improved from 1.8 to 2.5 because of the large amount of eeX background rejected by this cut. Diboson analyses are dominated by the small amount of available statistics, so in general it is not a good idea to reject 20% of the signal. The statistical uncertainty of the cross section measurement is 7% smaller when all of the $W\gamma$ candidates are used. Similarly, the extra statistics improve the limits on the anomalous couplings from the cross section measurement by about 5%. See Figure B.2.

The primary reason for rejecting these dirty photons is that, unlike the

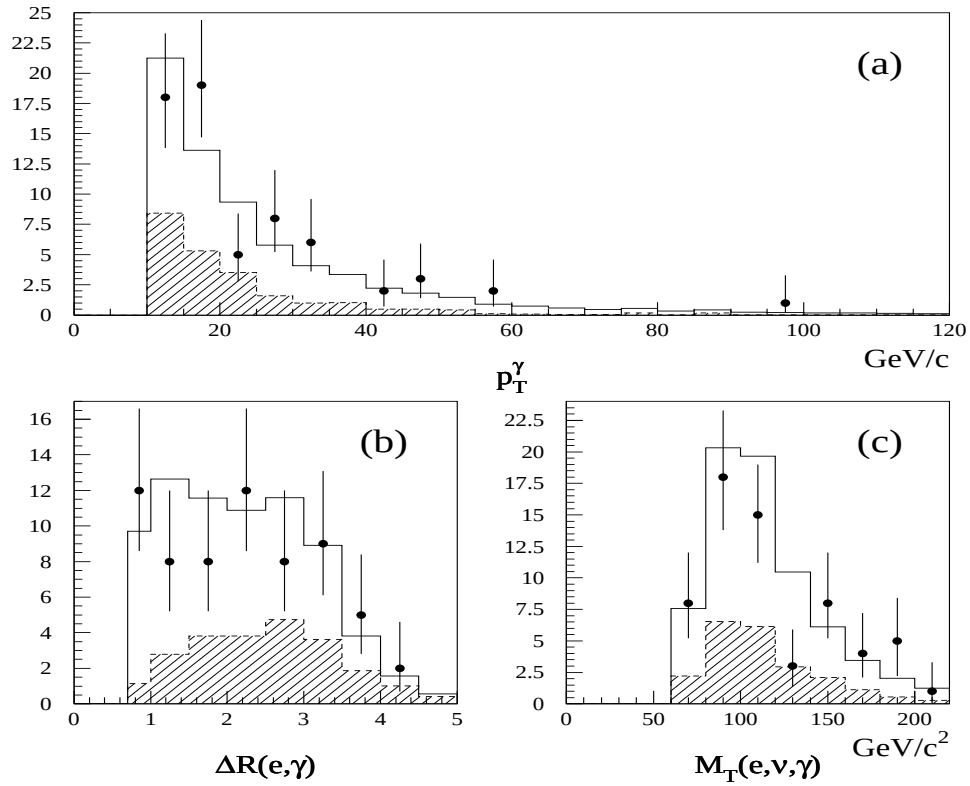

Figure B.1. (a) The p_T^γ spectrum for the Run 1b $W(e\nu)\gamma$ candidates before the hits–in–road cut is applied. The $\Delta R_{e\gamma}$ and $M_T(\gamma e;\nu)$ distributions (b,c) are also shown. There are two events with $M_T(\gamma e;\nu) > 220$ GeV/c^2. The points are the data with 1σ error bars. The solid histograms are the Monte Carlo predictions plus the background estimates (shown as shaded histograms).

large QCD background, the eeX background does not have a particularly nice shape. Electrons with unreconstructed tracks can populate all areas of the p_T^γ spectrum since the physics origin of these electrons can be one of many different processes. It is not practical to perform a binned–likelihood fit to a p_T^γ spectrum that is dominated by a large eeX background, especially when the background drives the lower edge of the empty bin to outrageous portions of the phase space. In other words, the total cross section for $p\overline{p} \rightarrow e\nu\gamma$ may completely consistent with the standard model prediction, but the differential

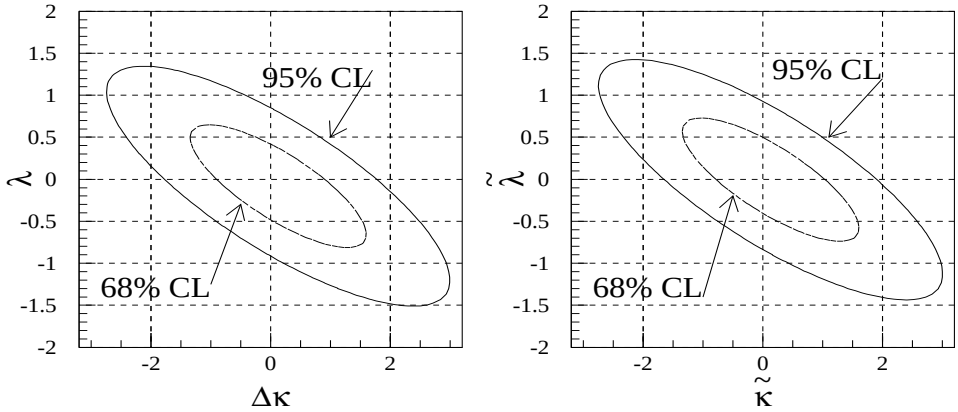

Run 1b W(eν)γ Cross Section Results (All Photons)	
68% axis limits	
$-0.9 < \Delta\kappa < 1.0$	$-0.8 < \tilde{\kappa} < 1.0$
$-0.5 < \lambda < 0.4$	$-0.4 < \tilde{\lambda} < 0.5$
95% axis limits	
$-1.8 < \Delta\kappa < 1.8$	$-1.7 < \tilde{\kappa} < 1.9$
$-0.9 < \lambda < 0.9$	$-0.8 < \tilde{\lambda} < 0.9$
Unitarity limits	
$\lvert\Delta\kappa\rvert < 3.3$	$\lvert\tilde{\kappa}\rvert < 23.3$
$\lvert\lambda\rvert < 1.8$	$\lvert\tilde{\lambda}\rvert < 1.8$

Figure B.2. Run 1b limits on the anomalous couplings from the fit to the total cross section, using both "dirty" and "clean" events, q.v. Figure 5.2. A dipole form factor scale of $\Lambda = 1.5$ TeV was assumed.

cross section $d\sigma/dp_T^\gamma$ is less consistent because of the bad description of the eeX background as a function of p_T.

BIBLIOGRAPHY

[1] S. Abachi *et al.* (DØ Collaboration), Phys. Rev. Lett. **72**, 2332 (1994).

[2] S. Abachi *et al.* (DØ Collaboration), Fermilab preprint FERMILAB-PUB-95-085-E, submitted to Phys. Rev. Lett.

[3] C. Quigg, *"Gauge Theories of the Strong, Weak, and Electromagnetic Forces,"* Addison-Wesley, 1983.

[4] M. Guidry, *"Gauge Field Theories: An Introduction with Applications,"* John Wiley & Sons, Inc., 1991.

[5] Review of Particle Properties, PDG, Phys. Rev. **D50** (1994) 1233, 1191, 1276, 1279.

[6] W.J. Marciano, Z. Parsa, Annu. Rev. Nucl. Part. Sci. **36**, 171 (1986).

[7] S. Willenbrock, *"Gauge Symmetries and Vector-Boson Self Interactions,"* in International Symposium on Vector Boson Interactions, edited by U. Baur, S. Errede, T. Müller, AIP Press (1996) p. 12.

[8] S. Abachi *et al.* (DØ Collaboration), Phys. Rev. Lett. **75**, 1023 (1995).

[9] F. Abe *et al.* (CDF Collaboration), Phys. Rev. Lett. **75**, 1017 (1995).

[10] S. Abachi *et al.* (DØ Collaboration), Phys. Rev. Lett. **75**, 1028 (1995).

[11] F. Abe *et al.* (CDF Collaboration), Phys. Rev. Lett. **74**, 1941 (1994).

[12] S. Godfrey, *"Quartic Gauge Boson Couplings,"* in International Symposium on Vector Boson Interactions, edited by U. Baur, S. Errede, T. Müller, AIP Press (1996) p. 209.

[13] R.W. Brown, D.Sahdev, K.O. Mikaelian, Phys. Rev. **D20**, 1164 (1979).

[14] H. Georgi, Ann. Rev. Nucl. and Part. Sci. **43**, 209 (1993).

[15] U. Baur, E.L. Berger, Phys. Rev. **D41**, 1476 (1990).

[16] U. Baur, D. Zeppenfeld, Nucl. Phys. **B308**, 127 (1988).

[17] J.M. Cornwall, D.N. Levin, G. Tiktopolous, Phys. Rev. Lett. **30**, 1268 (1973); Phys. Rev. **D10**, (1974) 1145; C.H. Llewellyn Smith, Phys. Lett. **46B**, (1973) 233; S.D. Joglekar, Ann. of Phys. **83**, (1974) 427.

[18] J. Alitti *et al.* (UA2 Collaboration), *"A Measurement of Two Jet Decays of the W and Z Bosons At the CERN $\overline{p}p$ Collider, "* Z. Phys. **C49** (1991) 17.

[19] A. Astbury *et al.*, Phys. Bull. **34**, (1983) 434-436.

[20] F. Abe *et al.* (CDF Collaboration), Phys. Rev. Lett. **66**, 2951 (1991).

[21] S. Abachi *et al.* (DØ Collaboration), Phys. Rev. Lett. **75**, 1456 (1995).

[22] R. Walczak, *"W and Z Boson Production at HERA,"* in International Symposium on Vector Boson Interactions, edited by U. Baur, S. Errede, T. Müller, AIP Press (1996) p. 198.

[23] F. Abe *et al.* (CDF Collaboration), submitted to Phys. Rev. **D**, (1995); preprint FERMILAB-PUB-95-301-E.

[24] R.W. Brown, *"Understanding Something About Nothing: Radiation Zeros,"* in International Symposium on Vector Boson Interactions, edited by U. Baur, S. Errede, T. Müller, AIP Press (1996) p. 261.

[25] T. Hahn, *"Exact and Approximate Radiation Amplitude Zeros - Phenomenologica Aspects,"* in International Symposium on Vector Boson Interactions, edited by U. Baur, S. Errede, T. Müller, AIP Press (1996) p. 224.

[26] J. Ohnemus, *"QCD Corrections to Diboson Production,"* in International Symposium on Vector Boson Interactions, edited by U. Baur, S. Errede, T. Müller, AIP Press (1996) p. 60.

[27] U. Baur, S. Errede, G. Landsberg, Phys. Rev **D50**, (1994) 1917.

[28] S.M. Playfer, *"Rare b Decays and Anomalous Couplings,"* in International Symposium on Vector Boson Interactions, edited by U. Baur, S. Errede, T. Müller, AIP Press (1996) p. 124.

[29] T. Kinoshita, W.J. Marciano, *"Quantum Electrodynamics",* in Vol. 7 of *"Advanced Series on Directions in High Energy Physics",* edited by T. Kinoshita. World Scientific (1990).

[30] K.F. Smith *et al.*, Phys. Lett. **B234** 191 (1990).

[31] J. Alitti *et al.* (UA2 Collaboration), Phys. Lett. **B 277**, 194 (1992).

[32] D. Benjamin, *"$W\gamma$ and $Z\gamma$ Production at the Tevatron,"* in 10th Topical Workshop on Proton-Antiproton Collider Physics, edited by R. Raja and J. Yoh, AIP Press (1996) p. 370.

[33] S. Abachi *et al.* (DØ Collaboration), Phys. Rev. Lett. **75**, 1034 (1995).

[34] J. Busenitz, *"Measuring the WWZ and $WW\gamma$ Couplings at LEP II, "* in International Symposium on Vector Boson Interactions, edited by U. Baur, S. Errede, T. Müller, AIP Press (1996) p. 12.

[35] D.A. Edwards, M.J. Syphers, *"An Introduction to the Physics of High Energy Accelerators,"* John Wiley & Sons, Inc., 1993.

[36] J. Thompson, *"Introduction to Colliding Beams at Fermilab,"* preprint FERMILAB-TM-1909 (1994) unpublished.

[37] S. Abachi *et al.* (DØ Collaboration), Nucl. Instr. and Methods **A338** (1994) 185.

[38] V. Hungerbühler, *"UA2: a Detector to Study $p\overline{p}$ Interactions at the SPS-collider,"* 1st Moriond workshop, in Lepton pair production: Proceedings, edited by J Tran Thanh Van. (1981) p. 223-229.

[39] R. Gilmore, *"Single Particle Detection and Measurement,"* Taylor & Francis, 1992.

[40] R. Fernow, *"Introduction to Experimental Particle Physics,"* Cambridge Universtity Press, 1986.

[41] R. Wigmans, Nucl. Instr. and Methods **141** (1987) 389.

[42] J. Bantly *et al.,* IEEE Trans on Nucl. Sci. **41** (1994) 1274.

[43] F. Abe *et al.* (CDF Collaboration), Phys. Rev. **D50**:5518-5561, 1994.

[44] N. Amos it et al. (E710 Collaboration), Phys. Lett. **B243** (1990) 158.

[45] J. Bantly *et al.,* DØ Internal Notes # 2318 (1994), # 2401 (1994), unpublished.

[46] M. Abolins *et al.,* IEEE Trans on Nucl. Sci. **36** (1989) 384; Nucl. Instr. and Methods **A289** (1990) 543.

[47] R. Genik II, *"A DSP Based Electromagnetic Trigger for the DØ Detector,"* in Proceedings of the IEEE Conference on Real-Time Computer Applications in Nuclear Particle and Plasma Physics 1995, 31.

[48] C. Gerber *et al.*, DØ Internal Note # 2140, unpublished, (1994).

[49] M. Paterno *et al.*, DØ Internal Note # 1782, unpublished (1993).

[50] R. Brun, F. Carminati, *GEANT v3.14*, CERN Program Library Long Writeup W5013, CERN (1993); J. Womersley, DØ Internal Note # 1520 (1992), unpublished.

[51] F. Paige, S. Protopopsecu, BNL Report no. BNL-38034 (1986), unpublished.

[52] A.D. Martin, R.G.Roberts, W.J. Stirling, Phys. Lett. **306B** (1993) 145.

[53] F. Abe *et al.* (CDF Collaboration), to be published in Phys. Lett. **B** (1994).

[54] H. Plothow-Besch, *PDFLIB v6.06,* CERN Program Library Long Writeup W5051, CERN (1995).

[55] R. Kehoe, M. Narain, DØ Internal Note # 2480 (1995) unpublished.

[56] R. Englemann *et al.,* Nucl. Inst. and Methods **A216** (1983) 45; M. Narain, DØ Internal Note # 1548A (1992), unpublished.

[57] S. Abachi *et al.,* Nucl. Instr. and Methods **A324** (1993) 53.

[58] P. Grudberg, DØ Internal Note # 2316 (1994), unpublished; S. Chopra *et al.,* DØ Internal Note # 2351 (1994), unpublished.

[59] S. Glenn, *private communication.*

[60] O. Dahl, *private communication.*

[61] S. Fahey *et al.,* DØ Internal Note # 2277 (1994), unpublished. J. Womersley, *private communication.*

[62] U. Baur, E.L. Berger, Phys. Rev. **D47**, 4889 (1993).

[63] G. Landsberg, *Ph.D. Dissertation*, SUNY @ Stony Brook (1994), unpublished.

[64] L. Chen DØ Internal Note # 2844 (1996), unpublished.